THE TANGENTIAL VELOCITY PROFILE AND MOMENTUM TRANSFER

WITHIN A MICROGRAVITY VORTEX SEPARATOR

A Thesis

by

MICHAEL CLAY ELLIS

Submitted to the Office of Graduate Studies of
Texas A&M University
in partial fulfillment of the requirements for the degree of

MASTER OF SCIENCE

December 2006

Major Subject: Nuclear Engineering

THE TANGENTIAL VELOCITY PROFILE AND MOMENTUM TRANSFER

WITHIN A MICROGRAVITY VORTEX SEPARATOR

A Thesis

by

MICHAEL CLAY ELLIS

Submitted to the Office of Graduate Studies of
Texas A&M University
in partial fulfillment of the requirements for the degree of

MASTER OF SCIENCE

Approved by:

Chair of Committee,	Frederick Best
Committee Members,	Yassin Hassan
	N. K. Anand
Head of Department,	William Burchill

December 2006

Major Subject: Nuclear Engineering

ABSTRACT

The Tangential Velocity Profile and Momentum Transfer within a Microgravity Vortex

Separator. (December 2006)

Michael Clay Ellis, B.S., Texas A&M University

Chair of Advisory Committee: Dr. Frederick Best

Liquid and gas do not separate naturally in microgravity, presenting a problem for two-phase space systems. Increased integration of multiphase systems requires a separation method adaptable to a variety of systems. Researchers at Texas A&M University (TAMU) have developed a microgravity vortex separator (MVS) capable of handling both a wide range of inlet conditions and changes in these conditions. To optimize the MVS design, the effects of nozzle area, separator geometry, and inlet flow rate must be understood. Computational fluid dynamics (CFD), in the form of Adapco's Star-CD, is used, along with laboratory testing, to accomplish this goal. Furthermore, as analysis aids for the laboratory data and CFD results, relationships for radial pressure, bubble transit time, and momentum transfer were developed.

Ground testing data showed a linear relationship between rotational speed and inlet flow rate. The CFD results compared well with the ground data and indicated that the majority of the rotational flow travels at nearly the same rotational speed. Examination of the tangential velocity profile also showed that a reduction of nozzle outlet area resulted in increased tangential velocities. Using dimensional analysis, a relationship

between separator radius, inlet momentum rate, fluid properties, and rotational speed was found. Applying this relationship to the ground data and CFD results showed a strong correlation between the two dimensionless groups. Linear regression provided an equation linking rotational speed to the separator parameters. This equation was tested against the ground data and shown to predict average rotational speed well for all separator models. These results were used to calculate the radial and axial transit times of gas bubbles within the separation volume. Radial transit time was found to decrease more rapidly than axial transit time as gas volume increased, indicating axial and radial transit times are closest in value for the all liquid case and increasing gas core diameter improves the operational characteristics of the separator. From a design standpoint, the all liquid case provides a minimum flow rate for successful phase separation. Maximum flow rate depends on the pressure resources of the system.

DEDICATION

For my mother, Deborah.

ACKNOWLEDGEMENTS

NOMENCLATURE

$\bar{F}_B$ = Bouyancy Force Vector

F_B = Bouyancy Force Magnitude

F_D = Drag Force Magnitude

F_R = Resultant Force on a Bubble

F_w = Magnitude of the Force due to Bubble Mass

$\bar{F}_r$ = Force Vector in the Radial Direction

$\bar{F}_\theta$ = Force Vector in the Tangential Direction

$\bar{F}_z$ = Force Vector in the Axial Direction

$\bar{a}$ = Acceleration Vector

a_b = Acceleration of a Bubble

a_c = Centripetal Acceleration

C_D = Drag Coefficient

ρ = Density

ρ_l = Density of the Liquid Phase

ρ_g = Density of the Gas Phase

μ_l = Dynamic Viscosity of the Liquid

σ_l = Surface Tension of the Liquid

V	= Fluid Volume
ω	= Rotational Speed
v_t	= Tangential Velocity of the Fluid
v_r	= Radial Velocity of a Bubble
v_{zr}	= Resultant Axial Velocity between a Bubble and the Liquid
v_z	= Axial Velocity of a Bubble
v_{term}	= Terminal Velocity of a Bubble
r	= Radial Position
$\hat{r}$	= Radial Unit Vector
θ	= Tangential Position
$\hat{\theta}$	= Tangential Unit Vector
z	= Axial Position
$\hat{z}$	= Axial Unit Vector
P_1	= Pressure at Inner Radial Face of a Fluid Element
P_2	= Pressure at Outer Radial Face of a Fluid Element
p	= Pressure at the Center of a Fluid Element
p_0	= Reference Pressure
X	= Integration Constant
C_1	= Integration Constant
R_α	= Length Associated with Angle α

D = Radial Distance from the Inlet Nozzle to Gas Core

D_z = Axial Distance from the Inlet Nozzle to the Baffle Plate

R = Separator Radius

α, β = Angles Between a Bubble Centerline and a Point Along the Bubble

Surface

L = Distance from the Separator Axis to a Bubble Center Point

L_1 = Radial Position of the Inlet Nozzle

L_2 = Radial Position of the Gas-Liquid Interface

Mo = Morton Number

Re = Reynolds Number

t_r = Radial Transit Time

t_z = Axial Transit Time

t_a = Time for a Bubble's Axial Velocity to Reach the Liquid Axial Velocity

$\dot{p}$ = Inlet Momentum Rate

A = Nozzle Outlet Area

v_N = Liquid Velocity at the Nozzle Outlet

L_N = Characteristic Length of the Nozzle Outlet

Re_N = Reynolds Number at the Nozzle Outlet

Π_1, Π_2 = Dimensionless Pi Groups

$\bar{g}$ = Gravitational Acceleration Vector

$\bar{v}$ = Fluid Velocity Vector

t = Time

μ = Fluid Dynamic Viscosity

v = Fluid Kinematic Viscosity

s_ϕ = Source Effects

Γ_ϕ = Diffusion Coefficient

$\vec{v}_{rel}$ = Flow Velocity Relative to the Coordinate Frame Velocity

ϕ = Dependent Flow Variable

$\sqrt{g}$ = Determinant of the Metric Tensor

V_{cell} = CFD Cell Volume

$\vec{S}_j$ = Surface Vector

$\vec{d}_{AB}$ = Distance between CFD Nodes A and B

f_j = CFD Geometry Factor

μ_t = Turbulent Viscosity

k = Turbulent Kinetic Energy

ε = Turbulent Dissipation Rate

g_i External Acceleration Component Magnitude

σ_m Schmidt Number

τ_{total} Total Shear Loss along the Separator Wall

l Viscous Layer Thickness

TABLE OF CONTENTS

LIST OF TABLES

LIST OF FIGURES

1. INTRODUCTION AND LITERATURE REVIEW

Development of the Texas A&M University (TAMU) microgravity vortex separator (MVS) began in 1988 to address problems associated with two-phase systems operating in low gravity environments. This device has undergone extensive analysis and testing aboard NASA's microgravity research aircraft, providing TAMU with over thirty hours of microgravity data from several thousand parabolas covering a wide variety of system applications. Analysis of this data has resulted in an optimized MVS design capable of meeting a wide range of system requirements.

Conceptually, the MVS consists of an injection nozzle attached to a right circular cylinder such that two-phase flow enters tangentially along the wall. During operation, a volume of liquid and gas exists within the cylinder. The momentum of the injected two-phase flow couples with the liquid present in the cylinder, producing, in microgravity, an axial gas column surrounded by a liquid vortex. This fluid orientation is driven by buoyancy resulting from the centripetal acceleration field present in the liquid vortex. Gas present in the injected two-phase flow travels to the gas column, while liquid remains in the vortex, effectively separating the two phases.

This thesis follows the style of *Nuclear Science and Technology*.

To increase performance and application potential of the MVS, a study of the fluid mechanics involved in the operation of this device has been conducted. Specifically, interest lies in the nature of the momentum coupling between the tangentially injected inlet flow and the rotating liquid film, as well as the tangential velocity profile produced by this momentum transfer. As the analytic solution to the Navier-Stokes equations is complicated for the MVS geometry and flow conditions, computational fluid dynamics (CFD), in the form of Adapco's STAR-CD software suite, is used to provide a numerical approximation. The results of this CFD analysis are then compared to microgravity test data for validation.

This document is divided into discussions of the history and current state of phase separator design, the theory involved in the operation and analysis of the TAMU MVS, ground testing and CFD procedure, the results of this analysis, and concluding remarks. Each of these discussions is separated into separate sections as indicated in the table of contents.

Background

In the microgravity environment experienced by space vehicles, liquid and gas do not naturally separate. This change in behavior is attributed to the lack of a buoyancy force, which depends on the acceleration field present within a fluid. On Earth, this acceleration field is provided by gravity, the magnitude of which allows the buoyancy

force to dominate other forces present in a fluid. And so, bubbles rise to the surface of liquids and two-phase mixtures will, in general, naturally separate through time. However, in the absence of a strong gravitational field, other forces, such as surface tension and the capillary effect, overcome buoyancy. As a result, natural buoyancy driven phase separation no longer occurs.

The lack of natural microgravity phase separation impacts a variety of space systems. Moisture exhaled from space vehicle crew members must be removed from the cabin air by humidity control systems. Waste water processing and hygiene systems need to separate unwanted solids and gases from the waste stream[1]. For reliable power production, proton exchange membrane (PEM) fuel cells require water management systems involving removal of water from the oxygen stream[2]. Lastly, with recent renewed interest in space nuclear power systems[3], a microgravity Rankine cycle is attractive for thermal to electric energy conversion and requires a phase separation device. These applications are just a few examples. The need for phase separation can be found in almost any system that encounters two-phase flow at some stage.

To answer this demand, researchers have conceived various methods of producing phase separation in low gravity environments, beginning in the 1950's. These separator types have included wicking, elbow, hydrophobic/hydrophilic, vortex, rotary fan separators, and combinations thereof. Each class of separator achieved acceptable performance for

particular applications and most performed in some capacity for the space program[1]. A summary concerning each of these types is found in the following paragraphs.

Microgravity Separator Types

An integral wick separator (IWS) is a heat exchanger which uses porous hydrophilic plates to allow energy transfer between a coolant line and humid air. As the air temperature decreases, condensate forms on the plates. This separator relies on capillary action to move the condensate from the plates to a region filled with wicking material. The liquid outlet line is connected to and maintained at a lower pressure than this region to allow water removal. A hydrophilic membrane is required on the liquid outlet line to prevent gas from entering. This separator was used for the Manned Orbiting Laboratory, regenerative life support equipment, and the Sabatier reactor[1].

A face wick separator (FWS) operates similarly to the IWS. However, instead of attempting to remove condensate from the cooling plates using capillary action, the FWS relies on the air flow to shear condensate from the plates. To collect the entrained condensate, a wicking material is placed in the air outlet. Similar to the IWS, the water is removed from this material by maintaining the liquid outlet line at a lower pressure. This separator was chosen for the Lunar Module[1].

A slurper separator (SS) is not a stand-alone separator, but a variant of the FWS intended to be used in conjunction with a rotary fan separator. This separator replaces the wicking material of the FWS with groups of chambers containing perforated hydrophilic plates. The purpose of the SS is to remove a portion of the air flow returning from the heat exchanger and use this portion to shear condensate collected on the perforated plates. The resulting two-phase flow is then passed to the rotary separator to complete phase separation. These separators are found on the International Space Station (ISS), space shuttle, extra-vehicular mobility unit (EMU), and Spacelab[1].

An elbow wick separator (EWS) is an elbow duct junction lined with wicking material on the outer radius. As high quality two-phase flow passes through this junction, centrifugal acceleration moves the liquid phase to the outer radius for collection by the wicking material. Similar to the other wicking separators, the outlet line is maintained at a lower pressure to remove liquid from the wicking material. The EWS was used for the Apollo and Biosatellite missions[1].

A hydrophobic/hydrophilic separator consists of a conical hydrophobic or hydrophilic screen, depending on whether the two-phase flow is high or low quality, placed in a duct with the apex pointing upstream. The phase to be separated collects on the screen and is sheared to either, if liquid is to be removed, a wicking material or, if gas is to be removed, a gas collection volume located at the outer radius of the screen. Liquid is removed from the wicking material similar to previous wicking separators and gas is

vented from the collection volume. This device found application with the Apollo, Biosatellite, and Gemini missions, as well as the EMU[1].

The TAMU separator falls into the class of vortex separators. This type uses the momentum of the two-phase flow to produce a centripetal acceleration field within the flow, allowing buoyancy forces to dominate and separation to occur. To achieve this result, the inlet flow is directed tangentially along the wall of a cylindrical chamber. As a result, a vortex is formed within the chamber. In the past, these separators were gas driven and used to separate liquid droplets from very high quality flow. In this case, the liquid droplets are driven to the wall and directed by a series of baffles to the liquid outlet. The gas is then removed from a central gas outlet port. This concept found application in microgravity waste collection systems[1].

The TAMU vortex separator operates successfully for any inlet quality of two-phase flow. Departing from previous vortex separation concepts, this design maintains a relatively thick liquid film at the wall of the cylindrical separation chamber. Due to the unique design of this chamber, the liquid film is able to change thickness, allowing adjustment to varying inlet flow conditions and providing the ability to accumulate fluids. Moreover, while previous vortex separators formed gas vortices, this design forms a liquid vortex surrounding a central gas column. Similar to other vortex separators, gas is withdrawn from the central column. A single baffle plate restricts the column from extending to the liquid outlet, from which the denser fluid exits.

At Keio University in Yokohama, Japan, several vortex separator designs are also currently under study. Much like the TAMU MVS, these separators rely on producing an acceleration field within the liquid portion of a two-phase flow to drive the buoyancy process[4].

Like vortex separators, rotary separators induce buoyancy by producing a centripetal acceleration field in the fluid. However, this concept uses a rotating drum rather than the momentum of the fluid to impart tangential velocity to the two-phase flow. This drum is usually motor-driven, although some designs have incorporated a turbine, spun by the two-phase flow, to drive the drum. This class of separator is historically the most widely used, finding application with the Lunar Module, Skylab, space shuttle, and ISS missions[1].

While each of these separator types operates successfully for specific applications, the purpose of the work done at TAMU is to provide microgravity phase separation for a variety of space systems through a single separator design. Currently, rotary separators are accepted as the most versatile microgravity separation technology. The high rotational speed generated by the rotating drum of these separators provides resistance to acceleration transients and, in comparison with past separator designs, rotary separators operate over the widest range of inlet flow conditions. However, compared with passive separator types such as the vortex separator, rotary separators suffer from higher power

consumption, from 500 to 2000 W, more complicated mechanical design, and higher maintenance requirements as a result of the high speed, rotating drum[5]. Furthermore, research completed over the past decade has shown the TAMU vortex separator more resistant to inlet flow variations and applicable to a variety of microgravity systems.

Texas A&M University Microgravity Vortex Separator History

For several years, various TAMU separator designs were subjected to concept validation tests aboard the KC-135. One such design, a magnetically-stirred separator, is shown in Fig. 1.1. These tests demonstrated the viability of employing the intrinsic momentum of a two-phase flow to induce phase separation in a fixed chamber. Testing then transitioned to understanding the operational characteristics of the MVS. By this time, the separator had evolved into a right circular cylinder with two-phase flow entering through a tangential nozzle. Within the cylinder, a baffle plate was introduced above the liquid outlet and a gas outlet tube extended axially into the separation region. This arrangement allows gas extraction from the gas column generated during operation while preventing this column from extending to the liquid outlet. Operational stability tests were conducted on this geometry to further understand the nature of the MVS.

During operation, the MVS may fail as a result of instability of the generated vortex. In general, these instabilities can be classified into two failure types, referred to as carry-over or carry-under. Carry-over occurs when liquid enters the gas outlet while carry-

under is an event in which gas enters the liquid outlet. In both cases, phase separation fails. To avoid this event, extensive testing of the hydrodynamic conditions resulting in carry-over or carry-under was conducted.
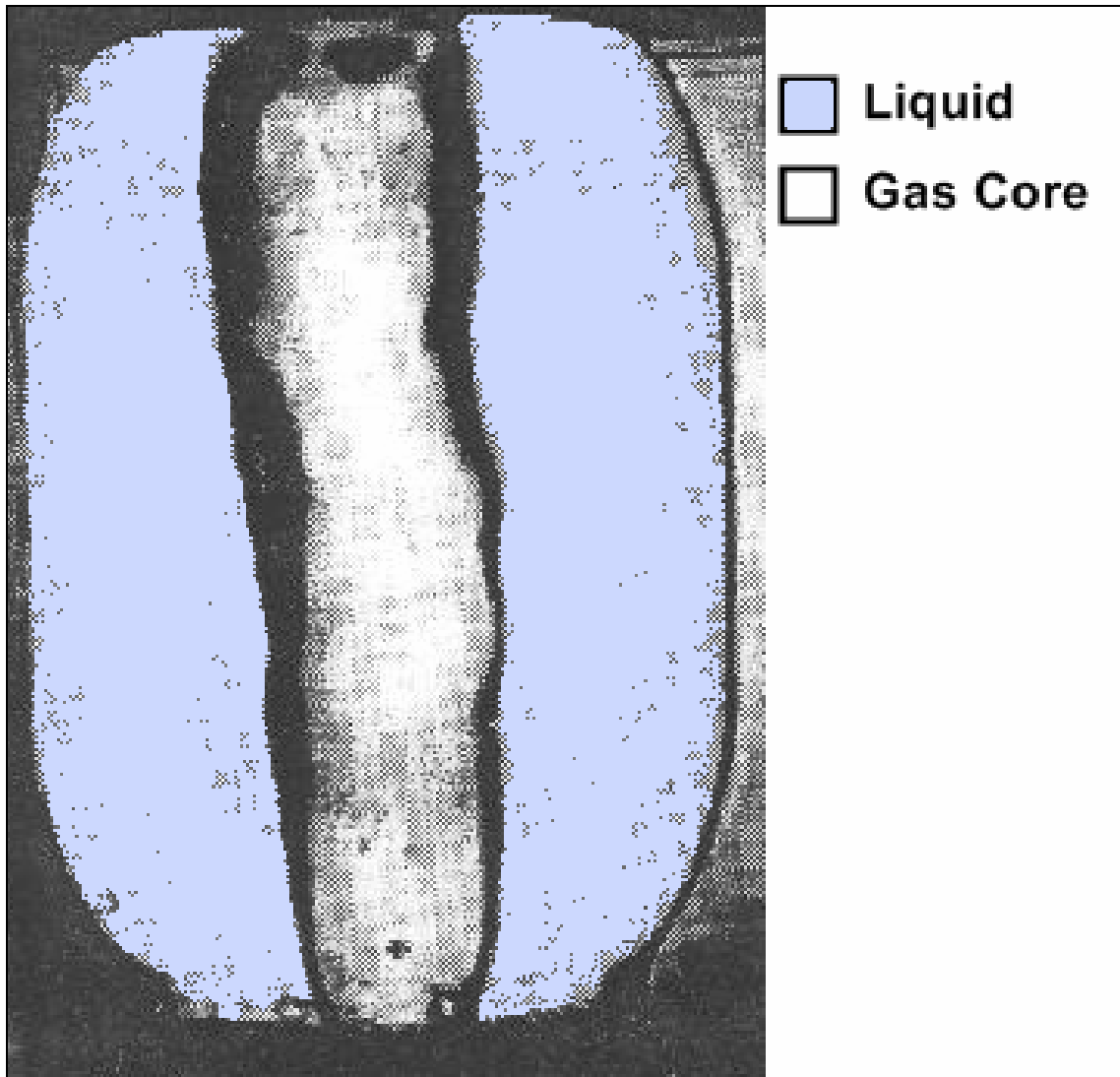
Fig. 1.1 Microgravity Testing of a Magnetically-Stirred Separator

Carry-under is related to the bubble transit time, radial and axial, within the separation volume. The radial bubble transit time is defined as the time required for the bubble to travel from a position at the wall of the separator, the location at which two-phase flow is injected, to the interface between the gas column and liquid film. The axial bubble transit time is defined as the time required for the bubble to travel from the axial position of the two-phase injection point to the top of the baffle plate. If the radial bubble transit time is greater than the axial bubble transit time, the bubble will move below the baffle plate and into the liquid outlet, resulting in carry-under. Both the radial and axial bubble transit times are related to the liquid flow rate of the injected two-phase flow. In fact, both transit times decrease with increasing flow rate, although the radial transit time decreases more rapidly than the axial transit time. Experiments have shown that, for an 11.4 cm diameter, 1.17 liter MVS operating with air and water, liquid flow rates below 2 Lpm result in carry-under. In other words, for this separator volume, radial transit time becomes greater than axial transit time at flow rates less than 2 Lpm.

Another contributing factor to carry-under is the liquid volume of the separator. In fact, this volume is also related to carry-over and management of this parameter is essential to successful microgravity phase separation. For lower liquid levels, the diameter of the gas column can become larger than the diameter of the baffle plate, allowing gas to travel to the liquid outlet. Conversely, for higher liquid levels, the gas column will collapse and allow liquid to travel to the gas outlet, resulting in carry-over. These two hydrodynamic limits establish the minimum and maximum allowable liquid, or gas,

volume allowable during separator operation. For the 1.17 L MVS, the minimum and maximum liquid volume was found to be 0.54 L and 1.04 L respectively, indicating 0.5 L of liquid or gas can be accumulated during operation.

Following the completion of the vortex stability tests, the separation ability of the TAMU MVS was tested alongside other separator models as part of the Separator Fly Off project in 1997. During this project, the separator operated successfully for all test points, out performing the other separator models. The two-phase flow rates included 1.6 to 8.3 Lpm of water and 0.2 to 1.2 SLpm of air.

After demonstrating the potential of the TAMU separator, testing of this device as part of a variety of systems soon followed. In 1998, the MVS was chosen to provide a closed two-phase test loop for a multi-chamber bioreactor and a packed bed device. The separator performed successfully for both systems, maintaining phase separation for two-phase flow rates of 2 to 9.8 Lpm of water and 0.5 to 3.1 SLpm of air. In 1999, the separator was chosen for the Immobilized Microbe Microgravity Waste-water Processing System (IMMWPS). A top down view of this separator during microgravity operation is shown in Fig. 1.2.
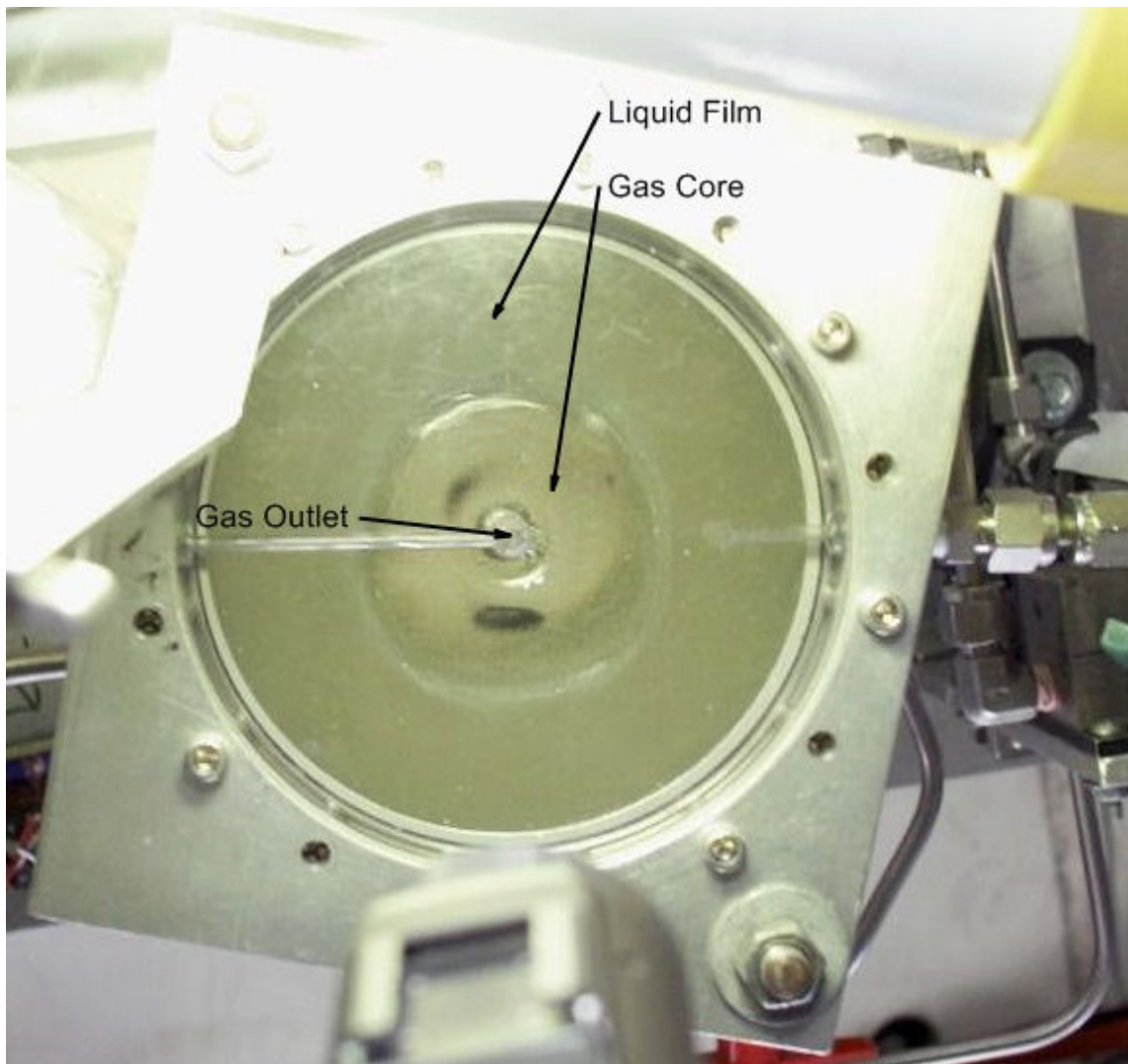
Fig. 1.2 Top Down View of the IMMWPS Separator during Microgravity Testing

As part of this system, the MVS was required to accumulate fluids over time. In order to measure the liquid volume within the separator during operation, an acoustic sensor was added to the device. By completion of this project in 2003, the acoustic sensor proved capable of providing dynamic monitoring of the liquid volume within the separator and the TAMU MVS became an integral part of the IMMWPS project. In 2000, the

separator was selected by Boeing to provide phase separation for their microgravity propellant transfer system. During testing for this system, the MVS was subjected to a full range of two-phase flow quality. Throughout the tests, the separator performed well for all inlet flow conditions. The MVS became part of the Proton Exchange Membrane (PEM) fuel cell system in 2003. Testing for this system involved integrating a gas driven ejector with the injection nozzle of the separator. During testing for this system, the separator was operated with gaseous Nitrogen flow rates up to 180 SLpm and at pressures of 413 kPa. Furthermore, start up testing was conducted with the separator in various orientations relative to high initial acceleration. The separator showed no dependence on start up orientation. Throughout all of these tests, the MVS has demonstrated the ability to provide microgravity phase separation for systems with a wide range of operating conditions.

While the TAMU MVS has found a variety of applications in the past, the potential of this microgravity phase separation device is just being realized. Currently, work is underway to apply the TAMU separator as a microgravity dehumidification device. In this capacity, a 1.2 liter MVS provides direct contact cooling of cabin air, condensate removal, and water reclamation for gas flow rates up to 180 SLpm. Flight testing of this system has begun. Also under investigation is the application of this separator as part of a microgravity Rankine cycle in support of project Prometheus. As part of this project, the separator will allow use of two-phase power cycles in microgravity, increasing the power resources available to space systems. Lastly, the MVS will support microgravity

testing of the Packed Bed Reactor Experiment (PBRE) underway at the NASA Glenn Research Center. In this testing, a 2.1 L MVS will provide an accumulation volume of 1 L and phase separation for inlet flow rates of 0 to 80 SLpm of gas and 3 to 10 Lpm of liquid. Flight testing of this experiment is expected in 2006.

Computational Fluid Dynamics

In order to improve the ease of system integration and allow for further optimization of the MVS design, the effects of nozzle area ratio, separator geometry, and inlet flow rate on momentum transfer and the tangential velocity distribution within the denser fluid must be understood. The accepted method for fluid behavior analysis involves solving the Navier-Stokes equations for the particular domain. For a three dimensional system such as the MVS, an analytic solution is not possible. For this reason, numerical analysis is used to provide an approximation to the solution, often in the form of Computational Fluid Dyanmics (CFD).

The interest in using CFD to understand the momentum transfer and tangential velocity profile inside a vortex separator is not limited to Texas A&M University. Researchers at the University of Tulsa (TU) employ CFX, a commercial CFD code developed by Ansys, to study cyclone separators used in the oil and gas industry. TU has found CFD capable of accurately simulating the cylindrical vortex flow encountered in this type of separator for single phase cases. The tangential velocity dissipates rapidly from the

inlet, with the greatest rate of dissipation occurring in the radial direction. Furthermore, results indicate all three velocity components, radial, tangential, and axial, vary throughout the device. The k-ε turbulence model was found to provide more accurate results for this geometry than the Reynolds Stress Model (RMS). Work is currently underway at TU to improve two-phase model results[6].

A joint effort between the University of Nottingham and the University of Hertfordshire used FIDAP, a commercial CFD code developed by Fluent, to study a vortex separator used in sewer water treatment plants, the Grit King[TM]. This separator geometry is considerably more complicated than either the TAMU or TU separator design. This complication arises most notably from a dip plate intruding from the top of the separator into the separator volume and a center cone that disrupts the vertical symmetry of the separator. As a result, a modified k-ε turbulence model, the advanced renormalization group (RNG) model, was necessary to provide an accurate flow solution. While the horizontal velocity results were well behaved, the vertical velocity components were chaotic and attributed to the complicated geometry of the separator. For model validation, results were evaluated alongside experimental data obtained using an Acoustic Doppler Velocimeter (ADV). Away from the center cone, the computed velocities compared well with experimental data. This was not always the case near the cone, however. The researchers believe including the effects of surface roughness in future calculations will provide a more accurate solution[7].

Peng et al. studied the reliability of CFD calculations with respect to reverse flow centrifugal separators. Laser Doppler Anemometry (LDA) was used to provide experimental data for evaluation of CFD performance. This data showed tangential velocity profiles decreasing linearly from the outer wall of the separator with all velocity components exhibiting negligible axial dependence. The CFD package was not specified by name but used a two-dimensional, axisymmetric Skew Upwind Differencing Scheme (SUDS) with a hybrid RMS, algebraic turbulence model. The researchers found the CFD results agreed with the LDA data concerning the location of the axial reverse flow boundary. However, this CFD package overestimated the axial velocity, with minimum and maximums nearly double the magnitude of the LDA data. With respect to radial velocity, the CFD package produced accurate results. Tangential velocity results were not compared with LDA data[8].

In the next section, theory relating to operation of the MVS and corresponding CFD analysis is discussed. Furthermore, several tools are developed to aid in comparing ground test data with CFD results.

2. THEORY

Much like conventional phase separation, the TAMU MVS relies on buoyancy effects to separate dissimilar density fluids. Buoyancy is defined as the net force acting on an object as a result of fluid pressure. In the case of phase separation, the object acted upon is the less dense fluid, usually taking the form of gas bubbles. The fluid pressure is developed in the denser fluid, usually a liquid, parallel to and as a result of the presence of an acceleration field. According to Newton's Second Law of Motion, the force developed by this acceleration, known as a body force, is shown for an infinitesimal fluid element as Eq. (2.1).

$$d\vec{F}_B = \vec{a}dm = \vec{a}\rho dV \qquad\qquad (2.1)$$

In terrestrial applications, this acceleration is gravity, the effects of which allow natural phase separation to occur as evidenced within our atmosphere by lakes and rainfall. However, since the MVS is intended to operate in the absence of gravity, another acceleration source must be provided. For this reason, the separator consists of a cylindrical separation chamber and liquid is injected tangentially along the curved wall of this chamber. This orientation provides the centripetal acceleration necessary to direct the flow in a circular path while producing minimal secondary flows. As the fluid rotates about the z-axis of the cylinder, centripetal force is continuously applied and transferred through the fluid. In accordance with Newton's Third Law of Motion, the

fluid reacts to this force internally and an equal and opposite force, referred to as centrifugal force, is generated. This force provides the acceleration field necessary for buoyancy to occur, driving liquid to the wall of the separation chamber and gas to the axis. The magnitudes of the centripetal and centrifugal acceleration, a_c, are equivalent and can be represented by Eq. (2.2) in cylindrical coordinates,

$$a_c(r,\theta,z) = \omega(r,\theta,z)^2 r = \frac{v_t(r,\theta,z)^2}{r} \qquad (2.2)$$

where ω is rotational speed and v_t denotes tangential velocity.

Aside from the internal body force, a fluid particle is also subject to external surface forces, typically shear stress and pressure. In a static environment, there is no deformation of the fluid particle and therefore no shear stress. The same can be said for a fluid undergoing rigid body rotation, in which the fluid is assumed to move with constant rotational speed. This approximation allows for an initial look at the behavior of the MVS.

Pressure Gradient

Consider a fluid element in cylindrical coordinates, shown in Fig. 2.1. In the radial direction, pressure is exerted inward on the front and rear radial faces. If the pressure at

the center of the element is $p = p(r,\ \theta,\ z)$, the pressure at the inner radial face, denoted as P_1, can be found using a Taylor series expansion about this point, shown as Eq. (2.3).

$$
\begin{aligned}
P_1 &= p + \frac{\partial p}{\partial r}(r_1 - r) + \frac{\partial^2 p}{\partial r^2}\frac{1}{2!}(r_1 - r)^2 + \frac{\partial^3 p}{\partial r^3}\frac{1}{3!}(r_1 - r)^3 + \ldots \\
&= p - \frac{\partial p}{\partial r}\frac{dr}{2} + \frac{\partial^2 p}{\partial r^2}\frac{dr^2}{8} - \frac{\partial^3 p}{\partial r^3}\frac{dr^3}{48} + \ldots
\end{aligned}
\tag{2.3}
$$

The differential length, dr, is assumed to be small enough that the square and higher powers of this length are negligible. With this being the case, a first order Taylor series expansion provides a sufficient description of the pressure equation within a differential fluid element. This truncated expansion is shown as Eq. (2.4).

$$
P_1 = p - \frac{\partial p}{\partial r}\frac{dr}{2}
\tag{2.4}
$$

The same can be done for the outer radial pressure, P_2, as shown in Eq. (2.5).

$$
P_2 = p + \frac{\partial p}{\partial r}\frac{dr}{2}
\tag{2.5}
$$

The radial component of the surface force, F_r, can then be found from the magnitude of these two pressures, the area on which they act, and the direction of their action, as shown in Eq. (2.6).

$$d\vec{F}_r = \left(p - \frac{\partial p}{\partial r} \frac{dr}{2} \right) r\, d\theta\, dz\, \hat{r} + \left(p + \frac{\partial p}{\partial r} \frac{dr}{2} \right) r\, d\theta\, dz\, (-\hat{r}) \qquad (2.6)$$
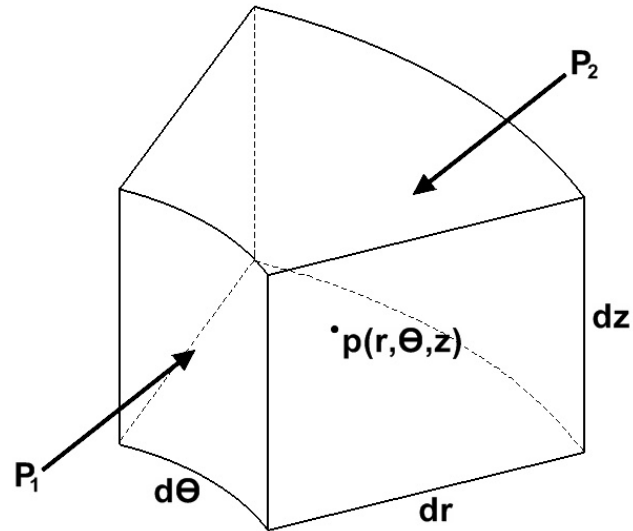
Fig. 2.1 Fluid Element and Radial Pressure Forces

Canceling terms produces Eq. (2.7), representing the surface force in the radial direction. Note that, had the Taylor expansion been carried out to a higher order, the even order terms would cancel out in this step. The result from using a single order or second order expansion would be the same.

$$d\vec{F}_r = -\frac{\partial p}{\partial r} r\, dr\, dz\, d\theta\, \hat{r} \qquad (2.7)$$

Following the same procedure, the axial and tangential surface force, respectively F_z and

F_θ, is determined, shown as Eqs. (2.8) and (2.9), respectively.

$$d\vec{F}_z = -\frac{\partial p}{\partial z} r\, dr\, dz\, d\theta\, \hat{z} \qquad (2.8)$$

$$d\vec{F}_\theta = -\frac{\partial p}{\partial \theta} dr\, dz\, d\theta\, \hat{\theta} \qquad (2.9)$$

Combining these equations produces the surface force vector for this fluid element, $\vec{F}_s$,

shown as Eq. (2.10).

$$\begin{aligned} d\vec{F}_s &= -\left(\frac{\partial p}{\partial r}\hat{r} + \frac{1}{r}\frac{\partial p}{\partial \theta}\hat{\theta} + \frac{\partial p}{\partial z}\hat{z} \right) r\, dr\, d\theta\, dz \\ &= -\nabla p\, r\, dr\, d\theta\, dz = -\nabla p\, dV \end{aligned} \qquad (2.10)$$

For the case of rigid body rotation, the only acceleration is a result of the rotation itself

and accounted for by the body force, $\vec{F}_b$. The resultant of the body force and surface

force must then be zero, as shown in Eq. (2.11),

$$d\vec{F}_s + d\vec{F}_b = -\nabla p\, dV + \vec{a}_c \rho_l\, dV = \vec{0} \qquad (2.11)$$

where ρ_l is the density of the denser fluid, typically liquid.

Dividing through by the differential volume and substituting Eq. (2.2) for centrifugal acceleration, noting that rotational speed is constant, gives Eq. (2.12).

$$-\nabla p + \rho_l \varpi^2 r \hat{r} = \vec{0} \tag{2.12}$$

Noting that the centrifugal acceleration acts only in the radial direction, the tangential and axial vector components are zero. Furthermore, the pressure equation must only be a function of radius and the partial derivative can be represented as a total derivative. Eq. (2.12) can then be reduced to the magnitude of the radial vector component, shown as Eq. (2.13).

$$-\frac{dp}{dr} + \rho_l \varpi^2 r = 0 \tag{2.13}$$

This function can be integrated to provide the pressure function for rigid body rotation, shown as Eq. (2.14),

$$p(r) = \frac{1}{2}\rho_l \varpi^2 r^2 + X \tag{2.14}$$

where X represents the resulting integration constant.

Evaluating this equation at a radius of zero, where some reference pressure exists, allows determination of the integration constant. This solution is shown as equation (2.15).

$$p(r) = \frac{1}{2}\rho_l \varpi^2 r^2 + p_0 \qquad (2.15)$$

This is the pressure field that provides the force necessary for buoyancy to occur. For comparison, the gravity driven pressure field is shown as Eq. (2.16),

$$p(z) = \rho_l g z + p_0 \qquad (2.16)$$

where g is the gravitational acceleration.

The pressure profile increase is quadratic for the centripetal system while linear for the gravitational system. This difference is due to the nature of the acceleration profile. Gravity can be assumed constant for most terrestrial purposes and is for the derivation resulting in Eq. (2.16). The centripetal acceleration of a fluid rotating with constant speed, however, increases linearly with radius. As a result, the pressure gradient developed by the rotating liquid flow within the cylindrical separation chamber increases from the central axis of the cylinder as the square of the radial position.

Bubble Movement

To understand the effect of this pressure gradient on the buoyancy force experienced by gas bubbles existing within the rotating liquid flow, consider the spherical bubble shown in Fig. 2.2.
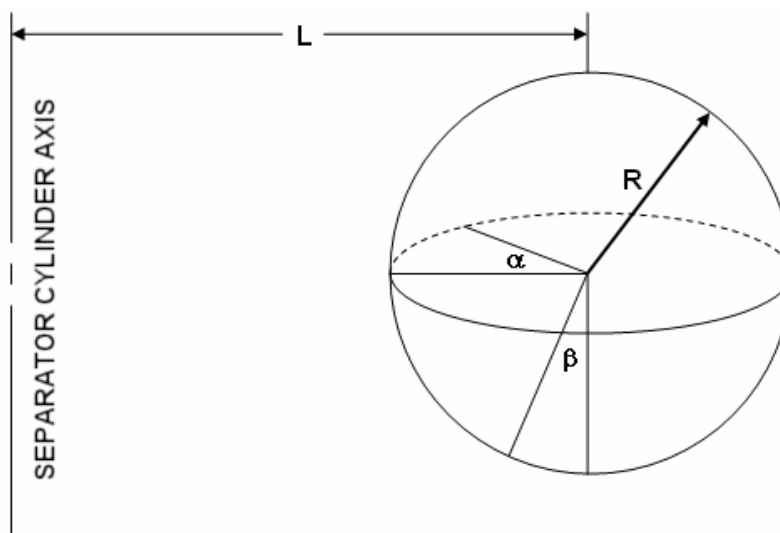
Fig. 2.2 Diagram of Spherical Gas Bubble

The surface of the bubble, on which the pressure acts, is most easily described by the angles denoted α and β. The pressure gradient, Eq. (2.15), has been derived in terms of the radial location within the separator cylinder. In order to perform the surface integration necessary to determine the buoyancy force exerted on the bubble, Eq. (2.15) will be translated to the coordinate system used to describe the bubble surface.

As shown in Fig. 2.2, let L be the distance from the separator axis to the center of the bubble while R denotes the radius of the bubble. Moving along the surface of the bubble, mathematically accomplished by changing the two angles which describe the surface, varies the radial distance from the separator axis and, therefore, the pressure exerted on the bubble surface. Fig. 2.3 demonstrates the manner in which the radius is affected by changing these two angles.
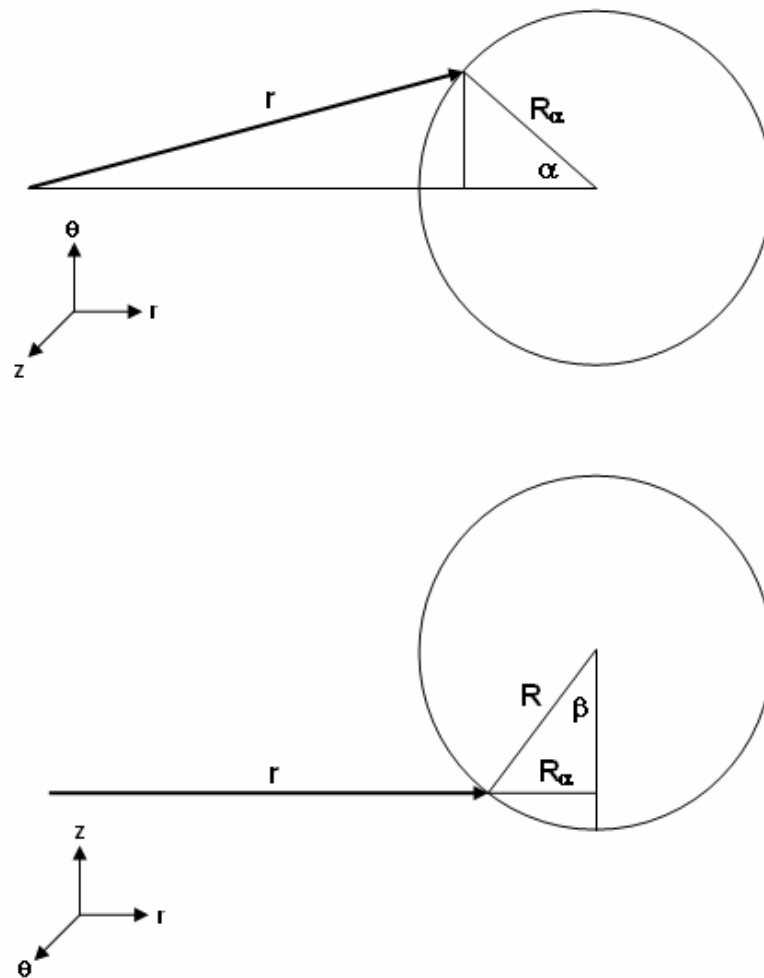
Fig. 2.3 Relationship between Radius and Spherical Angles

As angle α rotates from 0 to 2π, the radius behaves as shown in Eq. (2.17).

$$r = \left[R_\alpha{}^2 + L^2 - 2LR_\alpha \cos\alpha\right]^{1/2} \tag{2.17}$$

As shown in Eq. (2.18), angle β affects the magnitude of R_α.

$$R_\alpha = R\sin\beta \tag{2.18}$$

Using these two equations, Eq. (2.15) can be rewritten in terms of position on the bubble surface, referenced by the angles shown in Fig. 2.3. Pressure magnitude along the bubble surface is then expressed as Eq. (2.19).

$$p(\alpha,\beta) = \frac{1}{2}\rho_l\varpi^2\left(R^2\sin^2\beta + L^2 - 2LR\sin\beta\cos\alpha\right) + p_0 \tag{2.19}$$

This pressure acts normal to the bubble surface and inwards to the center. Because of spherical symmetry and the dependence of pressure on radial position only, the angular and axial components of the pressure vector balance each other over the entire surface of the sphere. For this calculation, the surface pressure can then be considered as Eq. (2.20).

$$p(\alpha,\beta) = \left[\frac{1}{2}\rho_l\varpi^2\left(R^2\sin^2\beta + L^2 - 2LR\sin\beta\cos\alpha\right) + p_0\right]\sin\beta\cos\alpha\,\hat{r} \tag{2.20}$$

This pressure acts only in the radial direction of the separator coordinate system. The buoyancy force can then be found by integrating this pressure over the surface of the bubble, shown as Eqs. (2.21).

$$F_B = \iint_A p(\alpha,\beta)d^2A$$
$$F_B = \int_0^\pi\int_0^{2\pi} p(\alpha,\beta)R^2\sin\beta\,d\alpha\,d\beta \tag{2.21}$$
$$F_B = -\rho_l\omega^2 L\frac{4}{3}\pi R^3\,\hat{r}$$

The negative sign indicates the buoyancy force acts towards the center of the separation chamber, along the radius. Noting that the volume of the bubble appears in the equation, the buoyancy force can be written as Eq. (2.22).

$$F_B = -\rho_l\omega^2 LV\,\hat{r} \tag{2.22}$$

Unlike gravity driven buoyancy, this force increases linearly with radial position. A bubble entering the separation chamber at the wall will experience the greatest buoyancy force.

For a bubble containing a fluid of significant density, the centrifugal force experienced by this fluid will act against the buoyancy force. This force is a result of the mass of the fluid and is commonly referred to as weight. Assuming the density within the bubble is constant, the weight of the bubble, F_w. can be represented by Eq. (2.23).

$$F_w = \rho_g \omega^2 LV \, \hat{r} \tag{2.23}$$

As this weight is always present when buoyancy is present, Eq. (2.22) is modified to account for this force and shown as Eq. (2.24).

$$F_B = \left(\rho_g - \rho_l \right) \omega^2 LV \, \hat{r} \tag{2.24}$$

While the liquid density is greater than that of the gas, the bubble will move inward towards the center of the separator. As the bubble gains radial velocity, v_r, drag force, F_D, will resist this movement and is represented by Eq. (2.25).

$$F_D = \frac{1}{2} C_D \rho_l v_r^2 \pi R^2 \, \hat{r} \tag{2.25}$$

For this case, fluid movement around the bubble is assumed to be similar to flow around a spherical body. This assumption of spherical bubble shape is acceptable for fluid flow

with a low Reynolds number, Re, and Morton number, Mo[9]. These non-dimensional

parameters are shown below as Eqs. (2.26) and (2.27),

$$Mo = \frac{a_b \mu_l^4}{\sigma_l^4 \rho_l} \tag{2.26}$$

$$Re = \frac{\rho_l v_r 2R}{\mu_l} \tag{2.27}$$

where a_b is the acceleration of the buble, μ_l denotes the viscosity of the denser fluid, and

σ_l is the surface tension of the denser fluid.

Experimental analysis conducted on this type of flow has provided a well accepted

empirical relationship between Reynolds number and the drag coefficient[10]. This

relationship is shown below in Fig. 2.4.
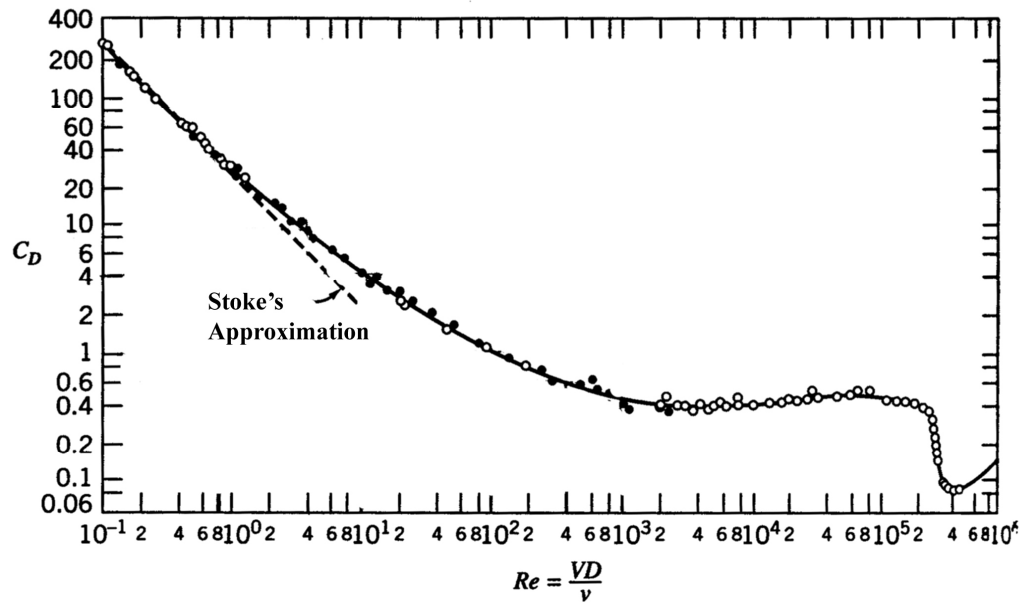
Fig. 2.4 Relationship between Drag Coefficient and Reynolds Number for a Smooth Sphere[10]

For very low Reynolds numbers (<0.8), Stokes found the drag coefficient, C_D, could be approximated by Eq. (2.28)[10].

$$C_D = \frac{24}{Re} \tag{2.28}$$

Substituting Eq. (2.27) for Re yields Eq. (2.29).

$$C_D = \frac{12\mu_l}{\rho_l v_r R} \tag{2.29}$$

Recalling Eqs. (2.24) and (2.25) and neglecting the effects of turbulence on the bubble velocity, a relationship for the acceleration of the bubble can be obtained from examining the balance between the buoyancy and drag forces, shown as Eq. (2.30).

$$F_R = \left[\left(\rho_g - \rho_l \right) \omega^2 L V + 6 \mu_l v_r \pi R \right] \hat{r}$$

$$a_b = \frac{F_R}{\rho_g V} = \left[\left(1 - \frac{\rho_l}{\rho_g} \right) \omega^2 L + \frac{9}{2} \frac{\mu_l v_r}{\rho_g R^2} \right] \hat{r} \qquad (2.30)$$

At the wall, the bubble is assumed to be traveling with negligible radial velocity. At this initial point, the potential acceleration of the bubble is at its maximum as the drag force is also negligible. As the bubble gains radial velocity and radial position, centrifugal acceleration decreases and the drag force increases. This effect leads to equilibrium between the two forces at a radial velocity known as the terminal velocity of the bubble, v_r. For flows in which Stoke's approximation is valid, this velocity can be determined from Eq. (2.30) and is shown as Eq. (2.31).

$$v_{term} = \frac{2}{9} \frac{R^2}{\mu_l} \left(\rho_l - \rho_g \right) \omega^2 L \qquad (2.31)$$

To simplify calculation of the bubble transit time, a desirable assumption is to neglect the period in which the bubble is accelerating to a terminal velocity. This period exists from the initial entry of the bubble into the rotational flow and for a short time thereafter.

In order to make this assumption, an approximation of this time period must be attempted. If the time period is negligible, the bubble velocity can be treated as though dependent on radial position alone.

Examining Eq. (2.30) further reveals dependence between bubble acceleration, radial velocity, radial position, and tangential velocity. As the bubble accelerates, radial velocity increases while radial position and tangential velocity decrease.

Introducing a time-step allows Eq. (2.30) to be approximated over the domain of interest which, in this case, is the period in which the bubble is accelerating to a terminal velocity. Initial values of negligible radial velocity and maximum radial position (at the wall) allow the initial acceleration to be calculated. This acceleration is assumed constant for time dt, after which the resulting radial velocity and position can be determined. At time dt, the acceleration is recalculated and this process continues until the terminal velocity is reached. The results for a dt of 1×10^{-9} seconds are shown in Fig. 2.5.
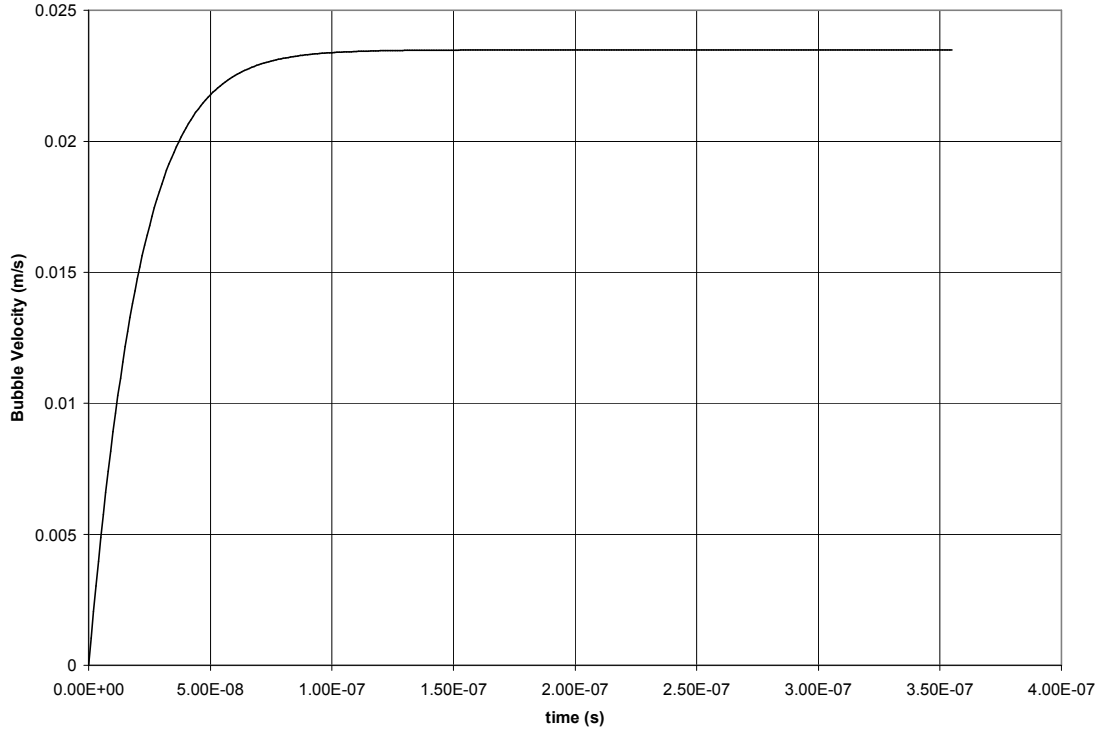
Fig. 2.5 Bubble Radial Velocity as Terminal Velocity Is Approached

It can be seen that the bubble takes approximately 1E-7 seconds to reach its terminal velocity. Since bubble transit times are usually on the order of several seconds, neglecting this period is an acceptable assumption and will greatly simplify the remaining calculations. Eq. (2.31) can now be integrated over the radial distance of interest to determine bubble transit times for flows in which the Reynolds number remains below ~1.0. This result is shown as Eq. (2.32),

$$t_r = \frac{D^2}{\displaystyle\int_D V_r} = \frac{9\mu_l}{R^2\omega^2(\rho_l - \rho_g)}\frac{(L_1 - L_2)^2}{(L_1^{\ 2} - L_2^{\ 2})} \tag{2.32}$$

Where D represents the distance traveled by the bubble, L_1 is the initial radial position of the bubble, and L_2 is the final position.

Others have determined empirical relationships for Reynolds numbers beyond the region for which Stoke's approximation is valid[11]. These functions allow the extension of this calculation to Reynolds numbers beyond 1.0 and are shown below as Eq. (2.33).

For Re < 0.1,

$$C_D = \frac{9}{2} + \frac{24}{Re}$$

For 0.1 < Re < 20,

$$C_D = \frac{24}{Re}[1 + 0.1315\,Re^{(0.82 - 0.05\log_{10} Re)}]$$

(2.33)

For 20 < Re < 1.5E3,

$$C_D = \frac{24}{Re}[1 + 0.1935\,Re^{0.6305}]$$

For the separator to function, the radial transit time must be less than the axial transit time. The axial transit time is defined as the time required for a bubble to travel from the inlet nozzle to the baffle plate. If this time is less than the radial transit time, gas bubbles have the opportunity to escape through the liquid outlet line rather than coalesce with the gas core. This event results in separation failure.

Bubbles attain an axial velocity as a result of drag imparted by the liquid. Recalling Eq. (2.25) and substituting the resultant axial velocity, v_{zr}, between the liquid and gas bubble for radial velocity provides Eq. (2.34).

$$F_D = \frac{1}{2} C_D \rho_l v_{zr}^2 \pi R^2 \, \hat{r} \qquad (2.34)$$

A relationship for the axial acceleration of the bubble, a_z, can be obtained by dividing by bubble mass, shown as Eq. (2.35).

$$a_z = \frac{3}{8} C_D \frac{\rho_l}{\rho_g} \frac{v_{zr}^2}{R} \qquad (2.35)$$

Substituting Stoke's approximation for the drag coefficient, Eq. (2.29), yields Eq. (2.36).

$$a_z = \frac{9}{2} \frac{\mu_l}{\rho_g R^2} v_{zr} \qquad (2.36)$$

The axial acceleration of the bubble can be viewed mathematically as the derivative of the axial velocity with respect to time. This relationship allows the equation to be solved for resultant axial velocity, or the velocity difference between the liquid and gas bubble, as a function of time, t, as shown in Eq. (2.37).

$$v_{zr} = C_1 e^{-\frac{9}{2}\frac{\mu_l}{\rho_g R^2}t}$$
(2.37)

At time $t=0$, the bubble axial velocity is zero and, therefore, the resultant axial velocity will be equal to the liquid velocity. This condition allows the integration constant, C_1, to be determined, giving the final equation for the bubble and liquid resultant axial velocity, v_{zr}, as a function of time and axial velocity of the bubble, v_z, shown as Eq. (2.38).

$$v_{zr} = v_z e^{-\frac{9}{2}\frac{\mu_l}{\rho_g R^2}t}$$
(2.38)

As the bubble approaches the liquid velocity, the resultant axial velocity approaches zero. The time required for this to occur, t_a, can be found by rearranging Eq. (2.38), yielding Eq. (2.39).

$$t_a = -\frac{2}{9}\frac{\rho_g R^2}{\mu_l}\ln\left(\frac{v_{zr}}{v_z}\right)$$
(2.39)

For air bubbles in liquid water, a bubble with a radius of 1 millimeter will achieve 99 percent of the liquid velocity in 1.5 milliseconds. A bubble with a 1 centimeter radius will achieve the same in a tenth of a second. As axial transit times are on the order of several seconds, the bubble axial velocity can be assumed to be that of the liquid. This is

a conservative assumption as the average axial liquid velocity will always be greater than that of the bubble. Assuming further that the liquid axial velocity is relatively constant within the separation volume, the axial transit time is then given by Eq. (2.40),

$$t_z = \frac{D_z}{v_z}$$

(2.40)

where D_z is the distance traveled by the bubble in time t_z.

Knowledge of the liquid velocity profile within the separation volume will then allow calculation of radial and axial transit times through Eqs. (2.32) and (2.40). These times are important indicators of separator performance. Furthermore, the velocity profile provides insight into the transfer of momentum between the inlet jet and liquid within the separation volume. Understanding this profile is key to modeling separator performance.

Dimensional Analysis

The tangential velocity profile of the liquid within the separation volume is a result of separator geometry, liquid velocity at the inlet, nozzle geometry, and fluid properties. Separator geometry defines both the fluid volume within the separation chamber as well as the surface area available for frictional losses. As maximum separation volume with

minimal frictional losses is desirable, the TAMU MVS is composed of a right circular cylinder. Rotating flow within this cylinder is driven by the momentum of the fluid injected tangentially by the inlet nozzle. This momentum rate, $\dot{p}$, results from the inlet velocity, v_N, area of the nozzle outlet, A, and density of the injected fluid, ρ, all of which define the inlet momentum rate, shown as Eq. (2.41).

$$\dot{p} = \rho A v_N^2 \tag{2.41}$$

The properties of the fluid, most notably density and dynamic viscosity, μ, will also affect the tangential velocity achievable within the separator. Density is not only related to the amount of momentum available at the injection point but also the fluid mass to be driven by this momentum. Viscosity describes both the frictional loss potential at the separator wall as well as the ability of momentum to transfer from the inlet to the fluid residing within the separation volume. Together these parameters determine the tangential velocity profile and, therefore, centripetal acceleration field of the rotating flow.

Dimensional analysis is useful as an initial look at the relationship between these parameters. The first step involves selecting variables to represent the parameters discussed above. For a right circular cylinder, separator geometry is identified by the cylindrical radius of the separation volume. Density and viscosity are selected to describe the fluid. The effects of nozzle geometry and inlet flow rate are distinguished

by the inlet momentum rate. However, as fluid density effects are already accounted for, this parameter will be modified to reflect inlet momentum rate per unit density. Assuming the average rotational speed of the fluid within the separation volume is approximated by a function of these variables, Eq. (2.42) describes this relationship.

$$\omega = f\left(R, \rho, \mu, \frac{\dot{p}}{\rho}\right) \tag{2.42}$$

According to the Buckingham Pi Theorem, reduction in the number of parameters used to describe this relationship is possible through combining the variables found in Eq. (2.42) to form dimensionless parameters, or Pi groups. While this approach will not allow calculation of the rotational speed or tangential velocity within the separator, the nature of the relationship between these variables may be uncovered.

Separator radius, density, and viscosity are selected as the repeating variables, indicating two dimensionless Pi groups exist for this relationship, shown as Eqs. (2.43).

$$\Pi_1 = R^a \rho^b \mu^c \frac{\dot{p}}{\rho}$$
$$\Pi_2 = R^d \rho^e \mu^f \omega \tag{2.43}$$

Solving for the appropriate powers to produce dimensionless numbers provides Eq. (2.44).

$$\Pi_1 = R^0 \rho^2 \mu^{-2} \frac{\dot{p}}{\rho} = \frac{\rho \dot{p}}{\mu^2} = \frac{\rho^2 A V^2}{\mu^2}$$

$$\Pi_2 = R^2 \rho^1 \mu^{-1} \omega = \frac{\rho R^2 \omega}{\mu}$$

(2.44)

Selecting the characteristic length of the nozzle, L_N, as the square root of the nozzle outlet area allows the first Pi group to be redefined as the Reynold's number, shown in Eq. (2.45).

$$\Pi_1 = \frac{\rho L_N V}{\mu} = \mathrm{Re}_N$$

(2.45)

The relationship between the selected separator parameters and average rotational speed is then given by Eq. (2.46).

$$\frac{\rho R^2 \omega}{\mu} = f\left(\mathrm{Re}_N\right)$$

(2.46)

The exact form of this relationship cannot be determined by this analysis. This result will be investigated further during discussion of the ground test data and CFD results. From a qualitative perspective, Eq. (2.46) relates the ratio of inertial to viscous forces at the injection nozzle to that within the separation volume. The ability of this balance to approximate separator performance is examined later.

Navier-Stokes Equations

Analysis of the continuity of mass and momentum within the separator is necessary to determine the velocity profile directly. This approach leads to the Navier-Stokes equations. Generally accepted as fundamental equations of fluid motion, solution of the Navier-Stokes equations allows for determination of velocity and pressure profiles within the domain of interest. However, complete analytic solutions are only possible for simple flow domains and, as a result, complicated flow geometries are approximated by simplification or use of numerical analysis. For the TAMU MVS, the latter is pursued, in the form of CFD, to provide an approximate solution to the flow domain.

The general, vector form of the Navier-Stokes continuity and momentum equations are shown as Eqs. (2.47) and (2.48), respectively,

$$\frac{\partial \rho}{\partial t} + \nabla \cdot (\rho \vec{v}) = 0 \tag{2.47}$$

$$\rho \frac{D\vec{v}}{Dt} = -\nabla p + \rho \vec{g} + \mu \nabla^2 \vec{v} \tag{2.48}$$

where ρ denotes the fluid density, t is time, $\vec{v}$ is the velocity vector, $\vec{g}$ represents the gravitational acceleration vector, and μ is the dynamic viscosity of the fluid.

For the MVS model, the fluid is assumed to behave as an incompressible continuum of constant density and viscosity, at thermodynamic equilibrium, and existing in an environment without external acceleration fields. The mass continuity equation, then, is expanded in cylindrical coordinates as Eq. (2.49)[10].

$$\frac{1}{r}\frac{\partial}{\partial r}(rv_r) + \frac{1}{r}\frac{\partial}{\partial \theta}(v_\theta) + \frac{\partial}{\partial z}(v_z) = 0 \tag{2.49}$$

The momentum equations for each spatial component, radial, r, tangential, θ, and axial, z, are shown respectively as Eqs. (2.50), (2.51), and (2.52)[10].

$$\rho\left(\frac{\partial v_r}{\partial t} + v_r\frac{\partial v_r}{\partial r} + \frac{v_\theta}{r}\frac{\partial v_r}{\partial \theta} - \frac{v_\theta^2}{r} + v_z\frac{dv_r}{dz}\right) =$$
$$-\frac{\partial p}{\partial r} + \mu\left\{\frac{\partial}{\partial r}\left[\frac{1}{r}\frac{\partial}{\partial r}(rv_r)\right] + \frac{1}{r^2}\frac{\partial^2 v_r}{\partial \theta^2} - \frac{2}{r^2}\frac{\partial v_\theta}{\partial \theta} + \frac{\partial^2 v_r}{\partial z^2}\right\} \tag{2.50}$$

$$\rho\left(\frac{\partial v_\theta}{\partial t} + v_r\frac{\partial v_\theta}{\partial r} + \frac{v_\theta}{r}\frac{\partial v_\theta}{\partial \theta} - \frac{v_r v_\theta}{r} + v_z\frac{dv_\theta}{dz}\right) =$$
$$-\frac{1}{r}\frac{\partial p}{\partial \theta} + \mu\left\{\frac{\partial}{\partial r}\left[\frac{1}{r}\frac{\partial}{\partial r}(rv_\theta)\right] + \frac{1}{r^2}\frac{\partial^2 v_\theta}{\partial \theta^2} - \frac{2}{r^2}\frac{\partial v_r}{\partial \theta} + \frac{\partial^2 v_\theta}{\partial z^2}\right\} \tag{2.51}$$

$$\rho\left(\frac{\partial v_z}{\partial t} + v_r\frac{\partial v_z}{\partial r} + \frac{v_\theta}{r}\frac{\partial v_z}{\partial \theta} + v_z\frac{dv_z}{dz}\right) = -\frac{\partial p}{\partial z} + \mu\left[\frac{1}{r}\frac{\partial}{\partial r}\left(r\frac{\partial v_z}{\partial r}\right) + \frac{1}{r^2}\frac{\partial^2 v_z}{\partial \theta^2} + \frac{\partial^2 v_z}{\partial z^2}\right] \tag{2.52}$$

The term on the left hand side of the momentum equations is referred to as the convection term, while the right hand side comprises the diffusion terms. Approximations to these terms are introduced by the CFD code and are necessary to reach a three-dimensional flow solution for the MVS geometry[12]. The CFD package used to provide a numerical solution to these equations is Star-CD version 3.15, produced by Adapco. The selection of Star-CD was based on this software's ability to include rotational momentum and buoyancy effects, years of success modeling fluid flows, and availability at TAMU.

Star-CD employs the Finite Volume (FV) method to discretize the Navier-Stokes equations. In this method, the fluid domain is broken down into cells, collectively referred to as a mesh or grid. This software supports a variety of polyhedral cells, as well as triangular prisms and pyramid cells, arranged in an unstructured fashion[12]. Structured meshes rely on mathematical equations to define the mesh shape. Unstructured meshes, on the other hand, consist of vertices which define the mesh shape, allowing more precise fits to complicated geometries. Furthermore, the variety of shape options allows the final mesh to conform to the original fluid domain. The downside to this approach is that each vertex must be recorded and maximum cell quantity is limited by available storage space and memory capacity. Recent advances achieved in computing technology, however, greatly offset this weakness[13].

For the TAMU MVS, the fluid domain is selected to include the separation volume, inlet

nozzle, and liquid outlet tube. This orientation is shown in Fig. 2.6.
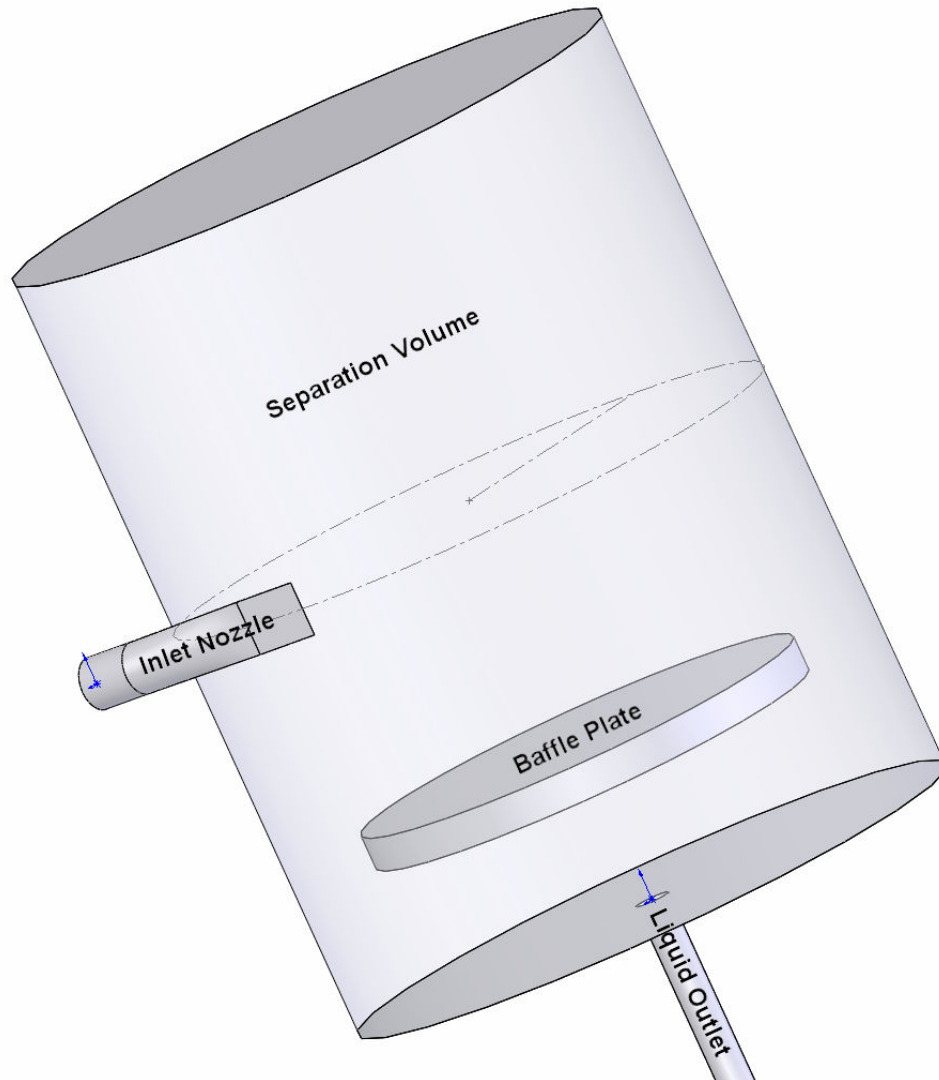
Fig. 2.6 MVS Simulation Geometry

The MVS mesh is constructed manually, using primarily hexahedral cells.   This

approach, while time consuming, is necessary due to the large length scale variations

within the separator. The nozzle entrance is typically hundredths of an inch wide, while the separation volume is several inches in diameter. Attempts to use Star-CD's automeshing feature resulted in overrefined meshes exceeding the available storage capacity and with estimated computational time far greater than desired. As a result, the primary meshing strategy involves easing the transition between the small nozzle cell volumes and relatively coarse interior mesh. Layering the separation volume mesh in such a way to allow small cell sizes near the wall, where the nozzle meets this volume, and gradually increasing cell size towards the inner radius of the separator meets this goal.

As the geometry of the mesh directly impacts computational time and accuracy, the rate of cell size increase towards the inner radius is restricted by numerical considerations. To avoid loss of detail in the velocity profile, adjacent cells are not allowed to exceed a volume ratio of four to one. Furthermore, each radial layer consists of several groups in which changes in volume occur only due to the change in radial position. Another factor to consider is mesh deformation, defined by cell aspect ratio, internal angle, and warp angle. Cell aspect ratio compares the longest side of a cell to the shortest, internal angle represents the nature in which cell faces are joined, and warp angle indicates the planar relationship between cell faces. As mesh deformation leads to erroneous coefficients within the discretized Navier-Stokes equations, these values are monitored so as not to exceed those recommended by Adapco[14]. Following this strategy, the MVS mesh is completed as shown in Fig. 2.7.
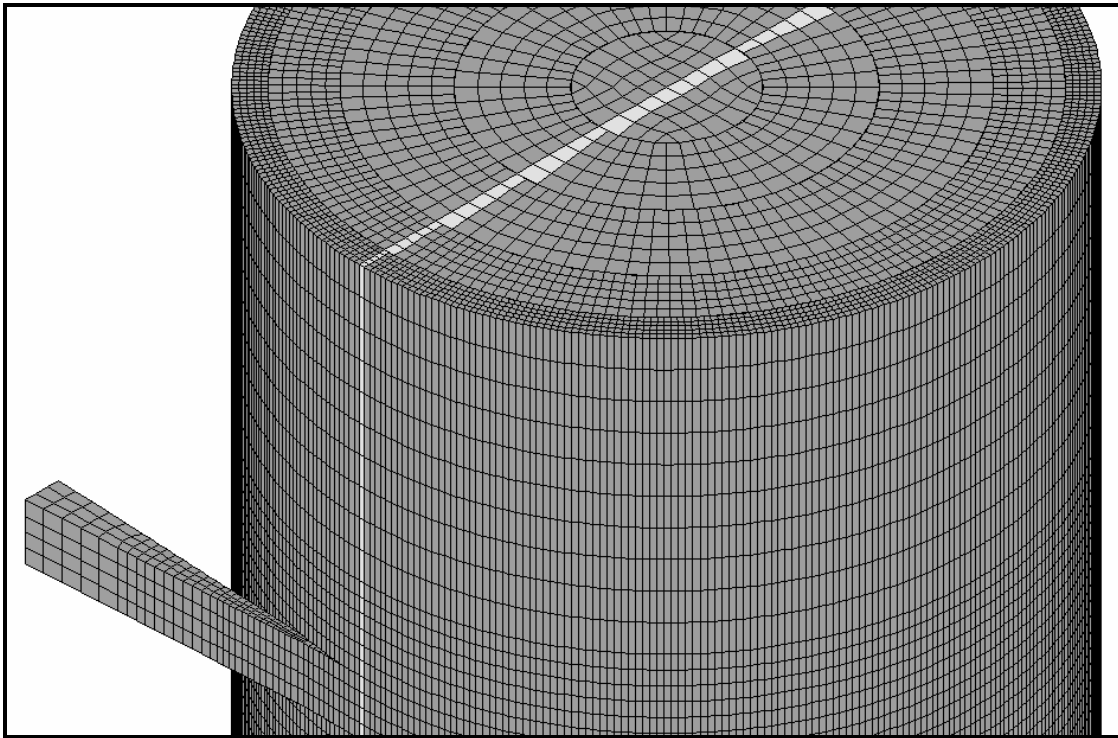
Fig. 2.7 MVS Mesh Section

The Navier-Stokes equations are integrated over each of these cells and time step for transient cases. Approximate solutions to the dependant variables are then determined at the center of each cell. With this approach, the conservation properties of the original Navier-Stokes equations are maintained within the discretized equations[12].

Star-CD employs the coordinate-free form of the conservation equations, referred to as the convection-diffusion equation, shown as Eq. (2.53),

$$\frac{1}{\sqrt{g}}\frac{\partial}{\partial t}\left(\sqrt{g}\rho\phi\right)+\nabla\left(\rho\bar{v}_{rel}\phi-\Gamma_{\phi}\nabla\phi\right)=s_{\phi} \tag{2.53}$$

where the source effects, s_{ϕ}, diffusion coefficient, Γ_{ϕ}, and flow velocity relative to the coordinate frame velocity, $\bar{v}_{rel}$, are ascertained from Eqs. (2.48) and (2.49)[12,15]. The dependent flow variable is represented by ϕ and $\sqrt{g}$ is the determinant of the metric tensor. This tensor varies for each coordinate system and is used to translate Eq. (2.54) from Cartesian space to the space described by the metric tensor.

Assuming a cell volume, V_{cell}, with cell faces described by the surface vector, $\bar{S}_{j}$, an exact solution to Eq. (2.54) is formulated as Eq. (2.54).

$$\frac{d}{dt}\int_{V_{cell}}\rho\phi dV+\sum_{j}\int_{S_{j}}\left(\rho\bar{v}_{rel}\phi-\Gamma_{\phi}\bar{\nabla}\phi\right)\cdot d\bar{S}=\int_{V_{cell}}s_{\phi}dV \tag{2.54}$$

The first term represents transient effects on the flow variable. In this work, steady state solutions are investigated and this term is not necessary but included for completeness. The summation following this term includes the positive convection term and negative diffusion term. Source and sink effects are represented by the final term. This equation is valid for a time dependent, arbitrary cell volume, shown in Fig. 2.8, bounded by moving surfaces, in this case the cell faces.
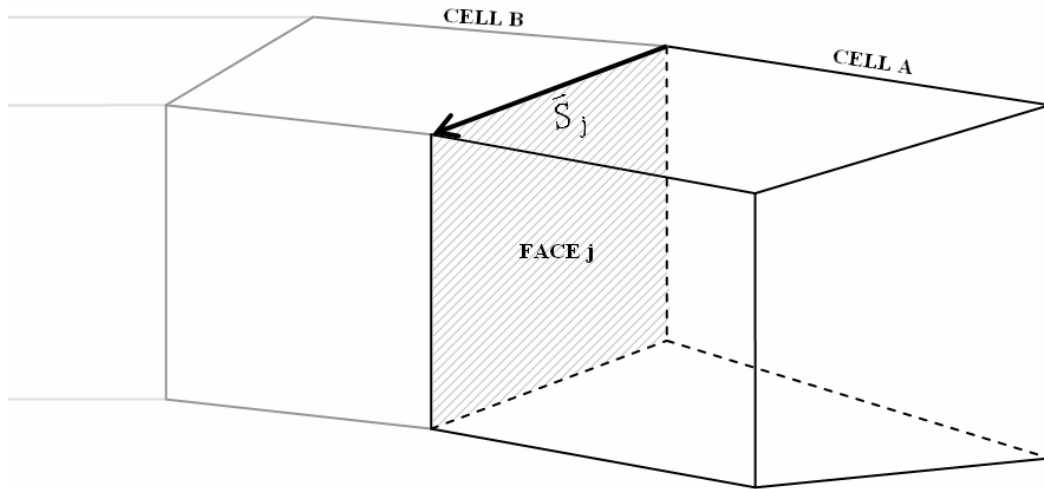
Fig. 2.8 Arbitrary Cell Volume and Surfaces

To reduce calculation time, Eq. (2.52) is simplified by approximating the integrals. The first term is estimated by introducing a time interval, δt, and comparing the instantaneous values separated by this interval, as shown in Eq. (2.55),

$$\frac{d}{dt} \int_{V_{cell}} \rho \phi dV \approx \frac{\left(\rho \phi V_A\right)_{new} - \left(\rho \phi V_A\right)_{pre}}{\delta t} \tag{2.55}$$

where *new* denotes the condition temporally succeeding the condition denoted by *pre*.

The second term is approximated by first splitting the convection and diffusion terms into separate summations, labeled C and D respectively in Eq. (2.56), and averaging them across each cell face.

$$\sum_j \int_{S_j} \left(\rho\vec{v}_{rel}\phi - \Gamma_\phi\bar{\nabla}\phi\right)\cdot d\vec{S} \approx \sum_j \left(\rho\vec{v}_{rel}\phi\cdot\vec{S}\right)_j - \sum_j \left(\Gamma_\phi\bar{\nabla}\phi\cdot\vec{S}\right)_j \equiv \sum_j C_j - \sum_j D_j \qquad (2.56)$$

The diffusion term is separated further into normal and cross-diffusion, shown as Eq. (2.57). Normal diffusion is represented by the first bracketed term and cross-face diffusion comprises the second. The subscripts denote scalar values at the center node of cells A and B, with $\vec{d}_{AB}$ being the distance vector between these nodes. The constant f_j is a geometry factor calculated by Star-CD and $\Gamma_{\phi j}$ is the interpolated diffusion coefficient for each cell face.

$$D_j \approx \Gamma_{\phi,j}\left[f_j\left(\phi_B - \phi_A\right) + \left\{\bar{\nabla}\phi\cdot\vec{S} - f_j\bar{\nabla}\phi\cdot\vec{d}_{AB}\right\}_j\right] \qquad (2.57)$$

The convection term is separated for calculation purposes as shown in Eq. (2.58).

$$\begin{aligned} C_j &\equiv F_j\phi_j \\ F_j &\equiv \left(\rho\vec{v}_{rel}\cdot\vec{S}\right)_j \end{aligned} \qquad (2.58)$$

This treatment is applied at each cell making up the flow domain, beginning, for each iteration, at cells with inlet boundary conditions and terminating at those with outlet boundaries[12]. Boundary conditions exist at the separator wall, inlet nozzle, and outlet tube. The separator wall is defined as a no slip boundary. This condition exists for all cell faces on the exterior of the model and all cell faces surrounding the baffle region. The inlet region is defined at the nozzle entrance and the outlet region at the liquid outlet exit, both shown in Fig. 2.9. The inlet region boundary conditions include average inlet velocity, calculated from inlet flow rate and nozzle inlet area, and fluid properties. The outlet region is defined by the flow split. For all cases, there is no flow splitting and this value is unity.
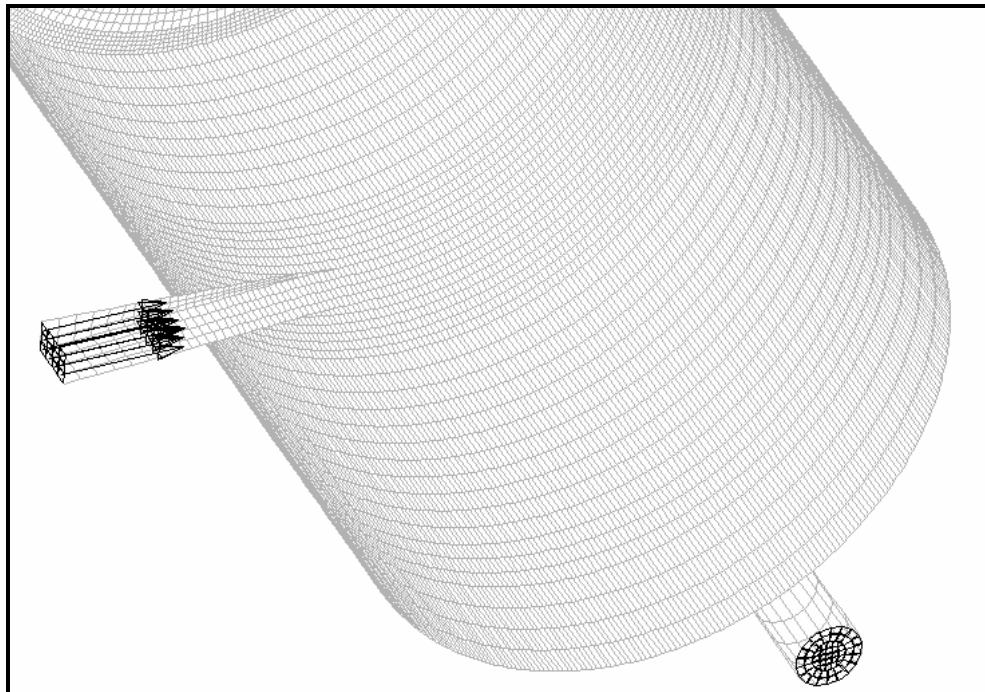
Fig. 2.9 Inlet and Outlet Boundaries

Once the fluid domain is defined, a solution algorithm is selected. Star-CD provides the Semi-Implicit Method for Pressure Linked Equations (SIMPLE), Pressure-Implicit Split-Operator (PISO), and SIMPISO, a combination of the preceding two. All methods temporarily decouple the flow equations using split operators, enforce continuity through a set of pressure equations formed by combining the mass and momentum conservation equations, and involve a predictor stage to produce preliminary velocity and pressure fields, which are corrected iteratively. Operator splitting allows approximation of the Navier-Stokes equations as a set of scalar equations, each with a single unknown[11].

PISO and SIMPISO differ from SIMPLE in that they consider numerical pressure gradient effects arising from non-orthogonal cell shapes. For the MVS mesh, the majority of the cells are orthogonal with respect to the global cylindrical coordinate system. However, the central region of the separation volume and the inlet nozzle are not. PISO also has the option of several corrector stages and is the only algorithm offered by Star-CD designed to perform transient analysis. With these differences in mind, a test case was analyzed using each method. While all three provided equivalent flow solutions, PISO completed in considerably less time. For this reason, the PISO algorithm was selected. Furthermore, the versatility of this algorithm will be advantageous for future transient analysis.

While PISO alone is sufficient for approximating a laminar flow field, an additional model is necessary to account for turbulence within the flow domain. Star-CD provides

several turbulence modeling options, including a variety of k-ε models, sub-grid scale models, and the Large Eddy Simulation model. As this is the first attempt to model the velocity profile of the MVS, the k-ε models are attractive as they maintain widespread use among the computational fluid dynamics community and have been shown to predict turbulent effects well for a variety of systems. Furthermore, for flow past a flat plate, the k-ε model compares closely to experimental data[16]. From a cylindrical point of view, much of the MVS flow path is similar to this type of flow. For these reasons, the standard, high Reynolds number k-ε model was chosen for this work. Noting, however, that the accuracy of these predictions is specific to the flow geometry of the system, as true for all turbulence models, and another approximation may be found more appropriate in future studies.

The high Reynolds number k-ε model consists of the turbulent kinetic energy, k, and dissipation rate, ε, equations. These equations are derived from the Navier-Stokes momentum equation using time averaged flow properties and shown below in coordinate free form as Eqs. (2.59) and (2.60), respectively,

$$
\frac{1}{\sqrt{g}}\frac{\partial}{\partial t}\left(\sqrt{g}\rho k\right)+\frac{\partial}{\partial x_j}\left[\rho\bar{v}_{rel,j}k-\left(\mu+\frac{\mu_t}{\sigma_k}\right)\frac{\partial k}{\partial x_j}\right]=
$$
$$
\mu_t\left(P+P_B\right)-\rho\varepsilon-\frac{2}{3}\left(\mu_t\frac{\partial v_i}{\partial x_i}+\rho k\right)\frac{\partial u_i}{\partial x_i}
$$

(2.59)

$$\frac{1}{\sqrt{g}}\frac{\partial}{\partial t}\left(\sqrt{g}\rho\varepsilon\right)+\frac{\partial}{\partial x_j}\left[\rho\bar{v}_{rel,j}\varepsilon-\left(\mu+\frac{\mu_t}{\sigma_\varepsilon}\right)\frac{\partial\varepsilon}{\partial x_j}\right]=$$

$$C_{\varepsilon 1}\frac{\varepsilon}{k}\left[\mu_t P-\frac{2}{3}\left(\mu_t\frac{\partial u_i}{\partial x_i}+\rho k\right)\frac{\partial u_i}{\partial x_i}\right]+C_{\varepsilon 3}\frac{\varepsilon}{k}\mu_t P_B \qquad (2.60)$$

$$-C_{\varepsilon 2}\rho\frac{\varepsilon^2}{k}+C_{\varepsilon 4}\rho\varepsilon\frac{\partial u_i}{\partial x_i}$$

where the turbulent viscosity, μ_t, is defined by Eq. (2.61),

$$\mu_t = \rho C_\mu \frac{k^2}{\varepsilon} \qquad (2.61)$$

the substituted equations, P and P_B, are given by Eqs. (2.62) and (2.63), respectively,

$$P = \left(\frac{\partial v_i}{\partial x_j}+\frac{\partial v_j}{\partial x_i}\right)\frac{\partial v_i}{\partial x_j} \qquad (2.62)$$

$$P_B = -\frac{g_i}{\sigma_h}\frac{1}{\rho}\frac{\partial\rho}{\partial x_i} \qquad (2.63)$$

g_i represents external acceleration components, typically gravity, σ_h is the Prandtl number, σ_m is the Schmidt number, and σ_k, σ_ε, C_{e1}, C_{e2}, C_{e3}, and C_{e4} are empirical coefficients[11]. The values used during computation are listed in the following section.

3. PROCEDURE

Several models of the MVS were ground tested to determine the average rotational speed for varying inlet flow rate. All tests were single phase liquid to avoid flow distortion caused by gravity driven buoyancy. The CFD mesh for each case was modeled after these separators as closely as possible, although slight variations between the computational and physical models did exist. In the following sections, the ground testing procedure and CFD case inputs are discussed.

Ground Testing

Each separator model was constructed primarily of acrylic, the exception being the aluminum nozzle interiors. The flow loop consisted of a centrifugal pump, laminar flow element flow meters, and vinyl tubing. This simple system is shown below in Fig. 3.1.
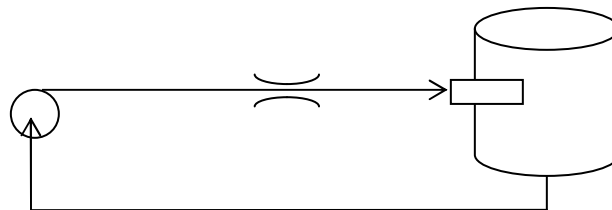
Fig. 3.1 Ground Testing System

Rotational speed was measured using a paddle wheel device, shown in Fig. 3.2. This device consisted of a paddle connected by a thin arm to an axle that extended along the

z-axis into the separation volume. The arm extended the paddle, oriented to face the tangential flow, from the axle along the radial axis. A bearing allowed the assembly to move freely with the tangential flow component. Three separator sizes were tested, listed in Table 3.1 by diameter, maximum liquid volume, and tested flow range.

Table 3.1 Ground Testing Information.

Separator Diameter	Maximum Liquid Volume	Tested Flow Rate Range
5.1 cm	0.10 L	0.5-1 Lpm
11.4 cm	1.2 L	1-6 Lpm
14 cm	2.1 L	1-11 Lpm

For each test, inlet flow rate was increased stepwise from the minimum to maximum value, back to the lower end of the range, and again to the maximum flow rate while recording rotational speed using an optical tachometer. At each step, the flow rate and rotational speed were allowed to stabilize before recording data. This produced three sets of data across the tested flow range, examined in the next section.
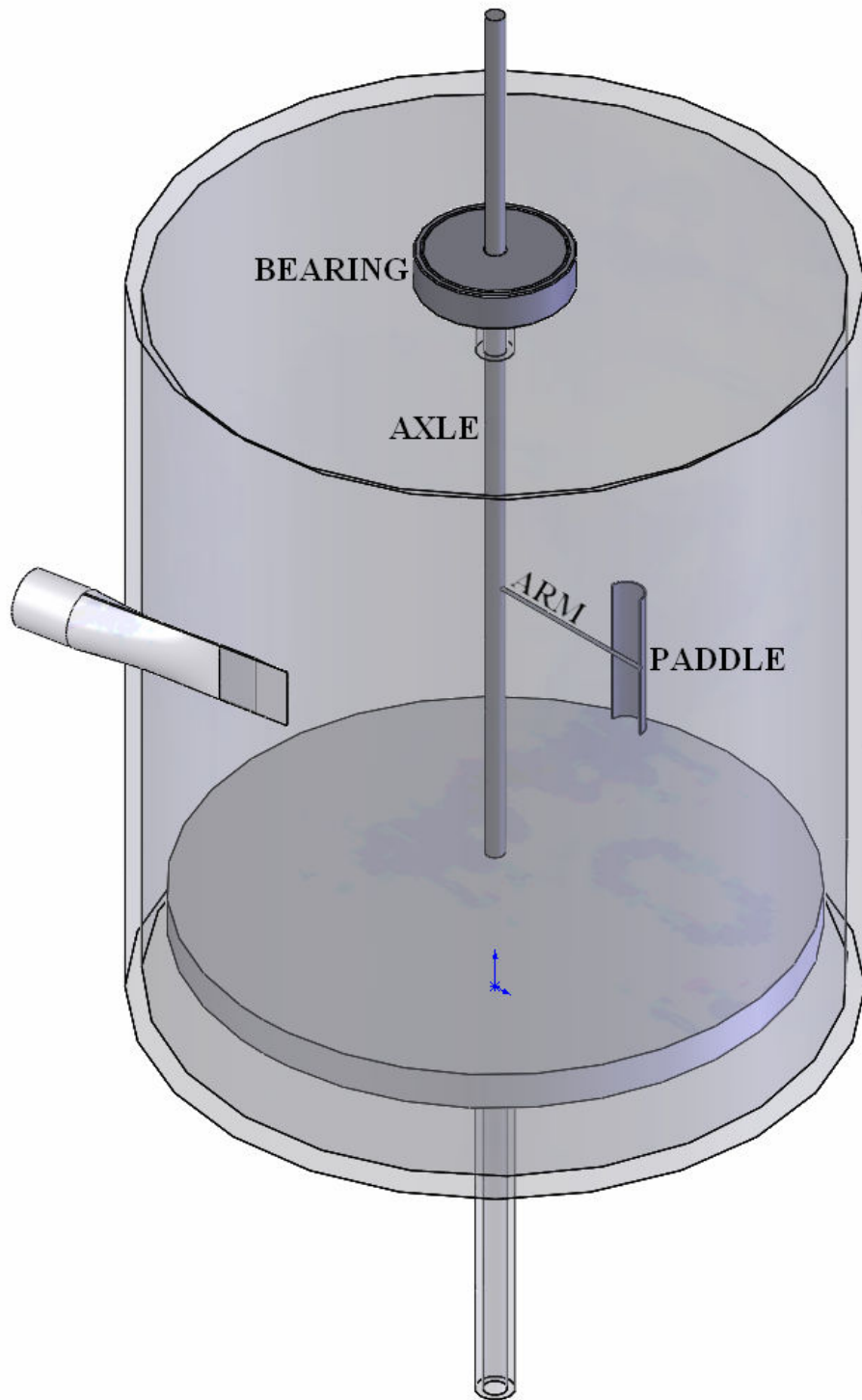
Fig. 3.2 Paddle Wheel Assembly.

Computational Fluid Dynamics

In this section, the procedure followed for mesh creation and case execution is summarized. The bulk of the work completed by the user involves Star-CD's preprocessor, Prostar. Using this tool, the computational mesh is created with the aid of simple cell generators, automatic cell coupling functions, boundary identifiers, and mesh checking routines that examine the final grid for connectivity and potential numerical stability problems.

The approach for the MVS mesh involved first creating two-dimensional shells for extrusion along the z-axis into three-dimensional space. Starting in two dimensions allowed for detailed user examination of the cell spacing and connectivity that would have been considerably more difficult in three-dimensional space. Furthermore, when mistakes were found, correction was simple and easy to visualize.

Three shells were created for extrusion into the final mesh. The first shell was created for the separation volume and represented the base shell structure for the remaining cells. As mentioned in the theory section, the strategy for all shells is listed below:

1. Minimize obtuse and acute angles between cell faces.
2. Capture detail near the separator wall, specifically in the area of nozzle influence.

3. Maintain aspect ratios of adjacent cell volumes within the limit prescribed by Star-CD.

4. Allow for several rows of cells with volume changes occurring due to radial position only before increasing or decreasing cell volume.

5. Minimize overall cell count without losing desired solution detail.

The first four objectives are necessary for numerical accuracy, as discussed in the previous section, while the last is concerned with reducing final computational time. Keeping these considerations in mind, the final shell was created as shown in Fig. 3.3.
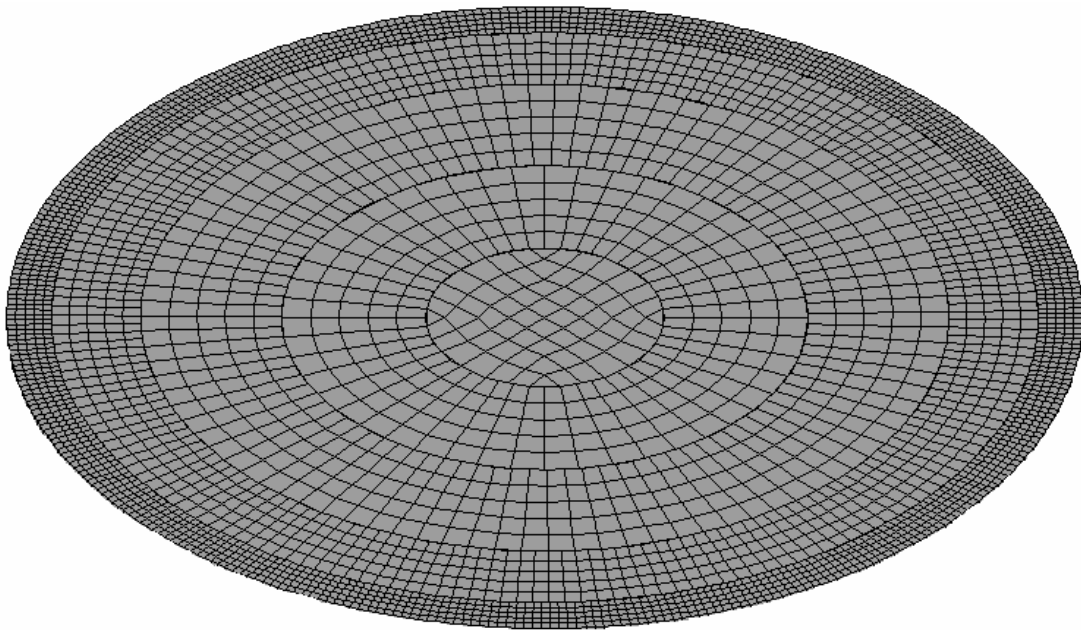
Fig. 3.3 Base Shell Configuration

This orientation comprises much of the MVS mesh, except for the baffle and nozzle regions. For the baffle region, the shell was modified by removing the interior portion where the baffle plate exists. The nozzle modification involved addition of the triangular shaped nozzle to the base shell and merging the nozzle cells with the base cells. These three shell types were then positioned to match the MVS geometry and extruded into the final mesh, shown in Fig. 3.4.

An effort was made to ensure matching faces of adjacent cells shared vertices. However, this was not always possible and the definition of cell couples was necessary. Couples inform the flow solver that adjacent cells are connected despite having different face vertices and of the face area shared between these two cells. Star-CD provides an automatic coupling tool which checks for discontinuities in the flow domain, referred to as cracks, and defines couples as necessary. After using this tool to connect the remainder of the flow domain, all couples were checked to confirm proper connectivity. Misarranged couples were deleted and created by hand. As a final check, the connectivity of the entire mesh was tested before proceeding.

Once all model cracks had been removed, the mesh boundaries were defined. Wall boundary regions included the exterior faces of the model and interior faces surrounding the baffle plate region, at which a no slip condition was set. The inlet and outlet regions included the nozzle inlet and liquid outlet, respectively. The inlet region was defined by average inlet velocity, temperature, and pressure. Throughout all cases, only inlet

velocity and separator geometry were changed while fluid properties, shown in Table 3.2, were held constant.
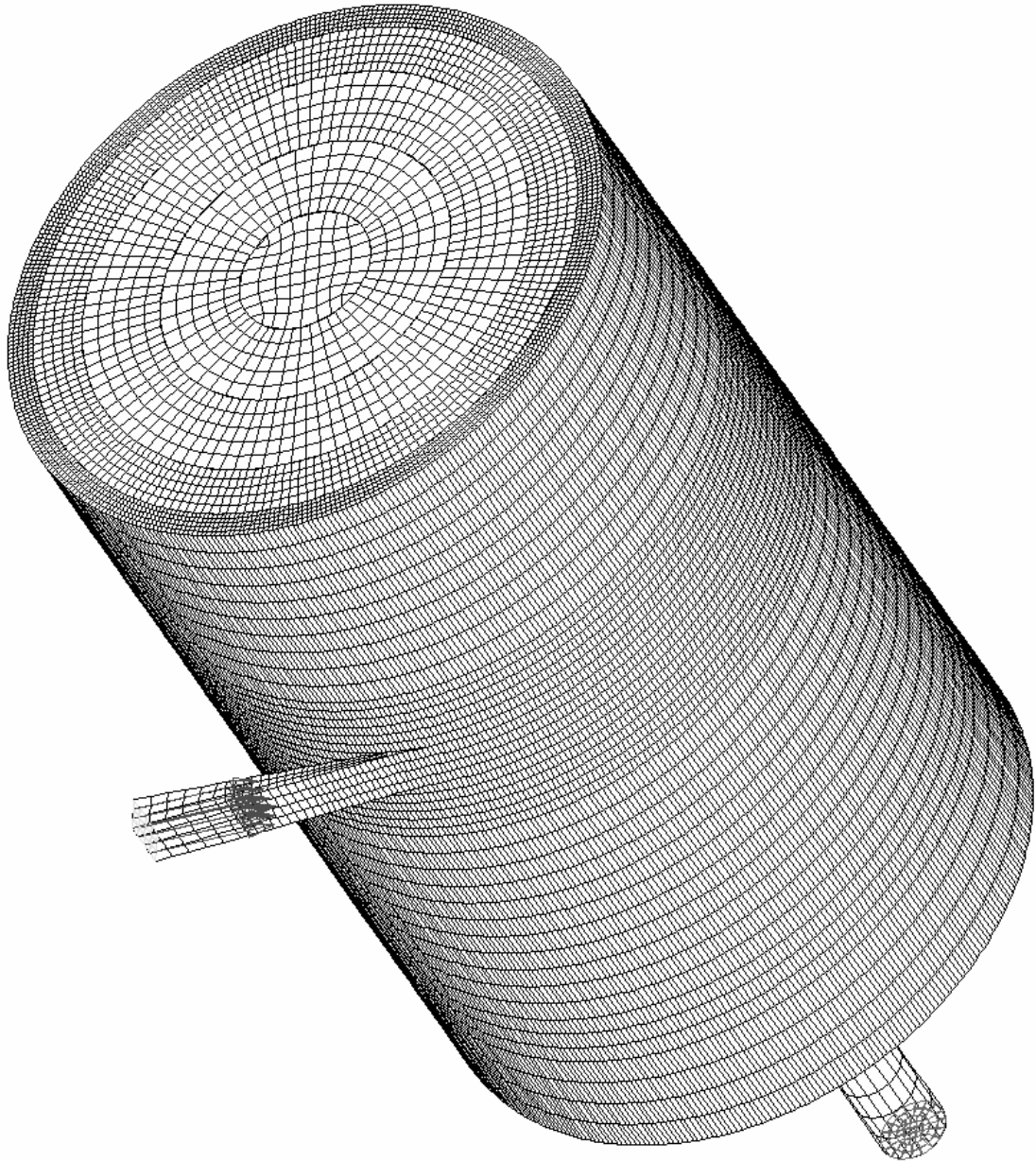
Fig. 3.4 Extruded MVS Mesh

Table 3.2 Properties of Water Used in CFD Model

Density	$997.3 \ \dfrac{kg}{m^3}$
Molecular Viscosity	$9.313 \times 10^{-4} \ \dfrac{kg}{ms}$
Specific Heat	$4.075 \times 10^{3} \ \dfrac{J}{kg\,K}$
Conductivity	$0.6078 \ \dfrac{W}{m\,K}$
Inlet Temperature	$22\,°C$
Inlet Pressure	$101\,kPa$

Of major interest in this study were the effects of varying inlet flow rate and separator geometry on the tangential velocity profile. As such, the inlet flow rate, nozzle outlet area, and separator diameter were adjusted to produce the CFD cases listed in Table 3.3

Table 3.3 CFD Case Parameters

Case	Separator Diameter	Nozzle Dimensions (Width x Height)	Inlet Flow Rate
20W058	5.1 cm	0.452 mm x 4.52 mm	0.58 Lpm
20W080	5.1 cm	0.452 mm x 4.52 mm	0.8 Lpm
45R200	11.4 cm	0.330 mm x 10.2 mm	2 Lpm
45R300	11.4 cm	0.330 mm x 10.2 mm	3 Lpm
45R400	11.4 cm	0.330 mm x 10.2 mm	4 Lpm
45W200	11.4 cm	1.02 mm x 10.2 mm	2 Lpm
45W300	11.4 cm	1.02 mm x 10.2 mm	3 Lpm
45W400	11.4 cm	1.02 mm x 10.2 mm	4 Lpm
45W500	11.4 cm	1.02 mm x 10.2 mm	5 Lpm
45W1000	11.4 cm	1.02 mm x 10.2 mm	10 Lpm
55R450	14 cm	0.404 mm x 12.4 mm	4.5 Lpm
55W200	14 cm	1.24 mm x 12.4 mm	2 Lpm
55W600	14 cm	1.24 mm x 12.4 mm	6 Lpm
55W630	14 cm	1.24 mm x 12.4 mm	6.3 Lpm
55W1000	14 cm	1.24 mm x 12.4 mm	10 Lpm

The final stage of preprocessing involves setting the computational parameters. The PISO algorithm was selected for steady state evaluation of the flow domain. This algorithm begins with a predictor stage which makes an initial attempt at producing a

velocity and pressure field from either the boundary conditions, in the case of the first iteration, or from the values determined from preceding iterations. At this stage, the momentum and continuity equations are decoupled and not required to agree with each other.

Next, momentum and continuity balance is attempted to a specified tolerance during corrector stages. If numerical stability problems arise, relaxation of the pressure variable may be used. The relaxation factor has a value greater than zero, representing maximum relaxation, or equal to one, representing no relaxation, and weights the pressure solution for a more gradual approach to convergence. For this work, a maximum of twenty corrector stages, a corrector tolerance of 0.25, and no pressure relaxation were selected. The actual number of corrector stages employed depends on whether the percent error of the dependent variables calculated by the decoupled flow equations is less than the specified corrector step tolerance. If the stage limit is reached without achieving the specified tolerance, a warning is issued by Star-CD and the algorithm moves on to the next iteration.

To further refine the velocity and pressure field, each corrector stage performs a number of inner iterations, or sweeps, monitored by more strict tolerance parameters, in this case specific to each variable, as well as a maximum sweep limit. For steady state calculations, relaxation factors are also implemented during these sweeps. The default tolerance parameters, sweep limits, and relaxation factors for each variable are shown in

Table 3.4. Adjustment of these parameters is only required in special cases as indicated by persistent warning messages issued by Star-CD[14]. For this work, adjustment was not necessary.

Table 3.4 Sweep Parameters for the PISO Algorithm.

	Velocity	Pressure	Turbulence	Enthalpy	Mass Fraction
Tolerance	0.1	0.05	0.1	0.1	0.1
Sweep limit	100	1000	100	100	100
Relaxation factor	0.7	1.0	0.7	0.95	1.0

To avoid endless iteration, the maximum number of outer iterations per run was set to 2000. Solution convergence was considered to occur when the residual error of the flow variables was less than 1×10^{-4}.

The turbulence model was chosen to be the high Re, k-ε model with constant turbulent viscosity. The empirical constants resulting from the time averaged derivation of this model from the momentum equations are selected for this model as recommended by Star-CD and shown below in Table 3.5. Again, adjustment is only recommended for special cases[14]. Since this work is the first detailed analysis of the phase separator flow domain and previous experimentation has yielded little information on turbulent behavior, the default values are used.

Table 3.5 Turbulence Model Coefficients

C_μ	σ_κ	σ_ε	σ_h	σ_m	C_{e1}	C_{e2}	C_{e3}	C_{e4}
0.09	1.0	1.22	0.9	0.9	1.44	1.92	0.0	-0.33

Finally, Prostar was used to compile the problem executable. Each case was run on an IBM Regatta p690. The results of each case are discussed in the next section.

4. RESULTS

The ideas developed in the theory section are tested and developed further through analysis and comparison of the ground testing data with CFD results. The ground testing data were produced using the single phase paddle wheel experiments as described in the procedure section. To allow for comparison of this data with the numerical analysis discussed in the theory section, the CFD cases were modeled to match, as closely as possible, the separators and operating conditions used in the ground tests. In the remainder of this section, the data and results will be discussed separately and then compared.

Rotational Speed Ground Test

Three separator sizes were tested, referred to by their diameter. Most of the microgravity testing conducted by TAMU has involved a 11.4 cm separator and this size is considered the base model for this study. The remaining two separator models were selected to be larger, 14 cm in diameter, and smaller, 5.1 cm diameter. The ground testing data are shown below, in Figs. 4.1 through 4.3, in order of decreasing size. These data are displayed with the inlet flow rate along the abscissa and rotational speed data along the ordinate. Finally, all three data sets are shown together in Fig. 4.4.
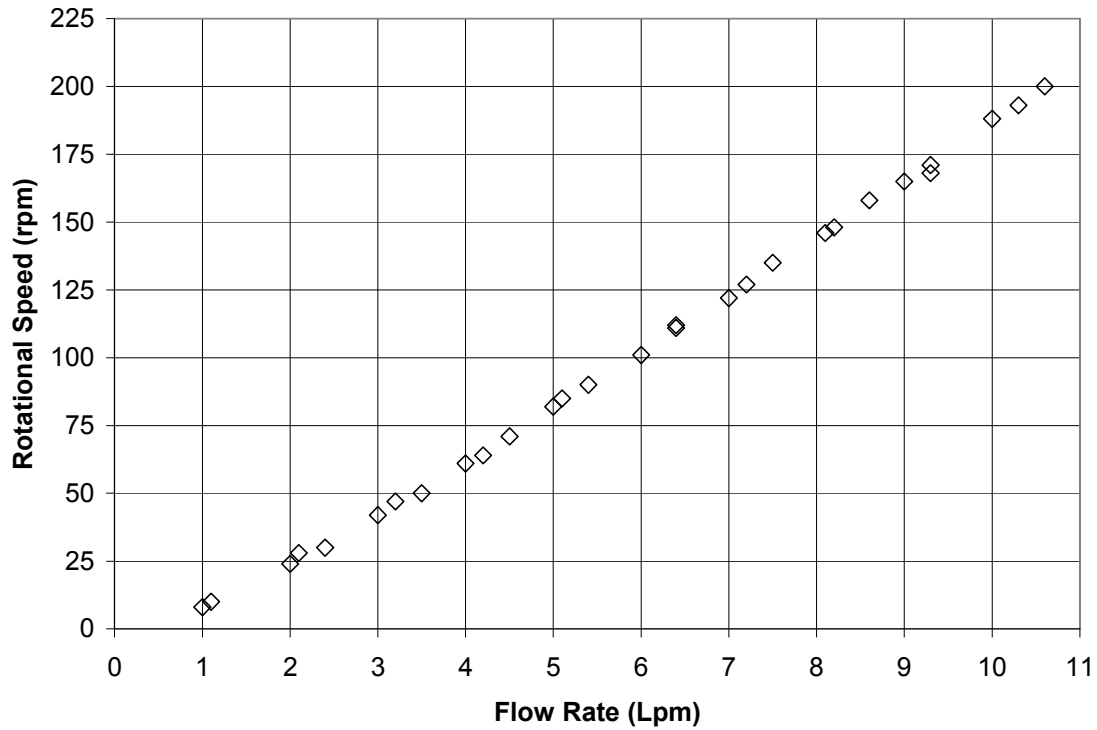
Fig. 4.1 14 cm Rotational Speed Data from Ground Testing

The data from the 14 cm separator ground tests show a linear relationship between flow rate and rotational speed with very little variance between test points at similar flow rates. The maximum tested flow rate, 6 Lpm, generated a 120 rpm vortex within the 14 cm separator while the minimum flow rate, 1.7 Lpm, generated a 28 rpm vortex.
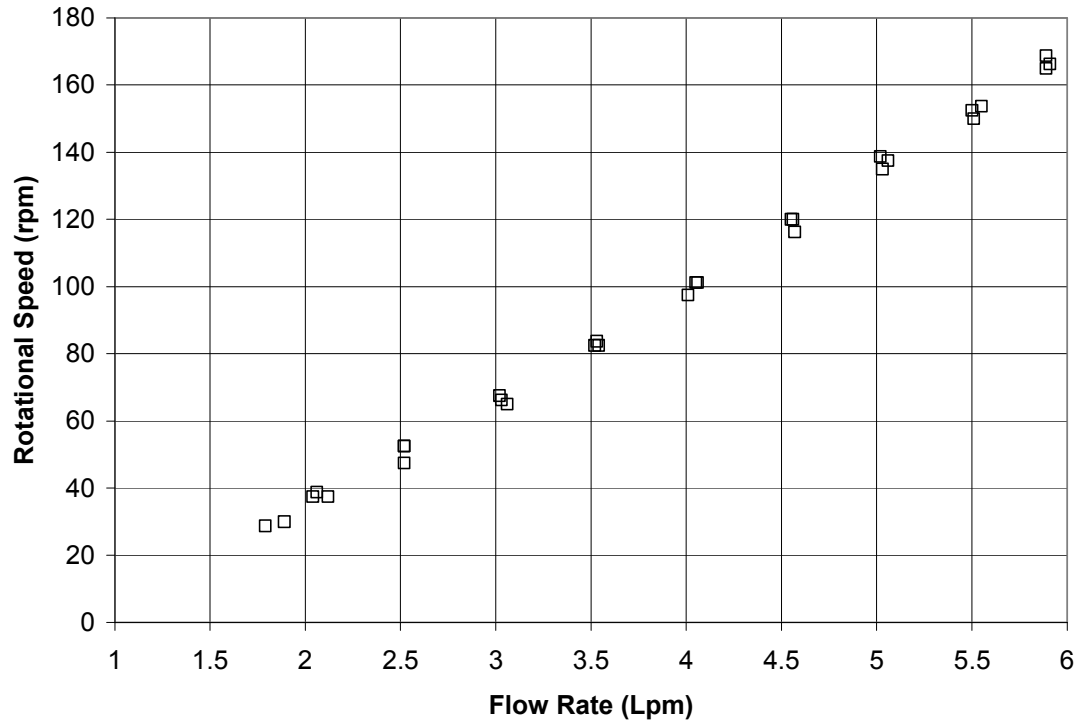
Fig. 4.2 11.4 cm Rotational Speed Data from Ground Testing

The data from the 11.4 cm separator ground tests also show a linear relationship with minimum variance. The maximum tested flow rate, 5.8 Lpm, generated a 163 rpm vortex within the 11.4 cm separator while the minimum flow rate, 1.6 Lpm, generated a 25 rpm vortex.
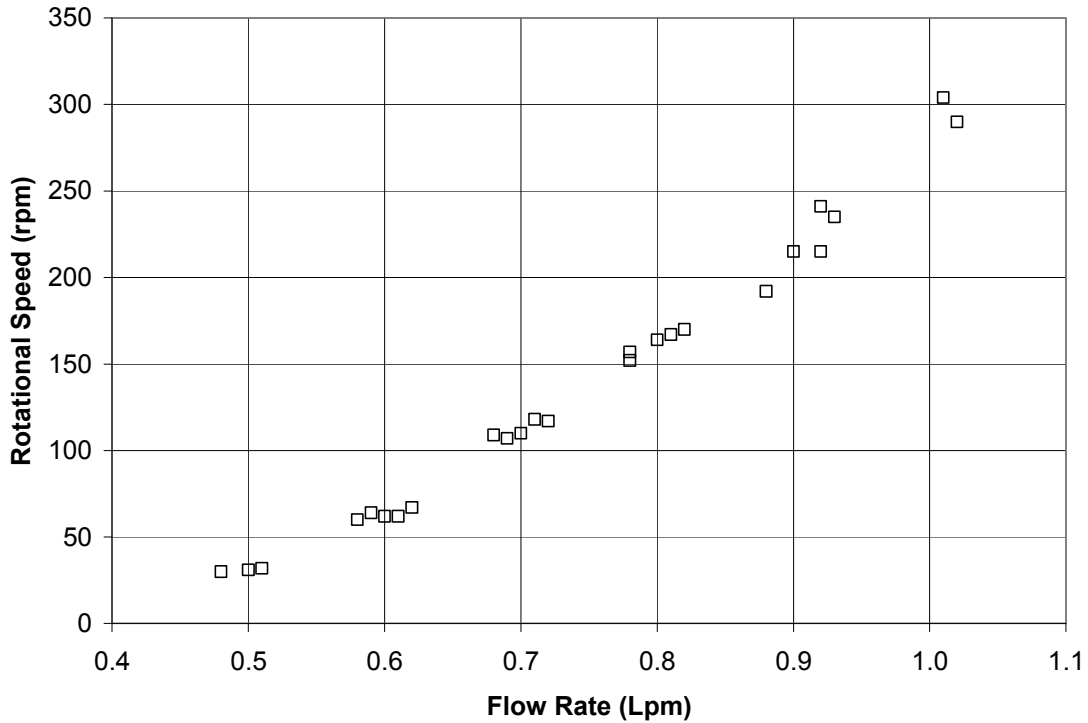
Fig. 4.3 5.1 cm Rotational Speed Data from Ground Testing

The data from the 5.1 cm separator ground tests show a linear relationship similar to the preceding separator data but with more variance. This variance is due to a combination of the sensitivity of the 5.1 cm separator to inlet flow rate and the flow rate measurement error. For instance, a change of 0.1 Lpm results in an approximate rotational speed increase of 50 rpm. For the larger separators, a flow rate change of 2 Lpm or more is necessary to produce a similar rotational speed change. As a result, the smaller a separator becomes the more important flow meter precision becomes. The flow meter selected for these tests operated with a standard error of ±0.05 Lpm, lacking the precision necessary for the 5.1 cm separator and resulting in a more scattered data set.

However, insight into the operation of the smaller separator is still provided. In future tests, the flow rate sensitivity of this separator must be considered. For the test associated with Fig. 4.3, the maximum tested flow rate, 1 Lpm, generated a 300 rpm vortex within the 5.1 cm separator while the minimum flow rate, 0.5 Lpm, generated a 30 rpm vortex.
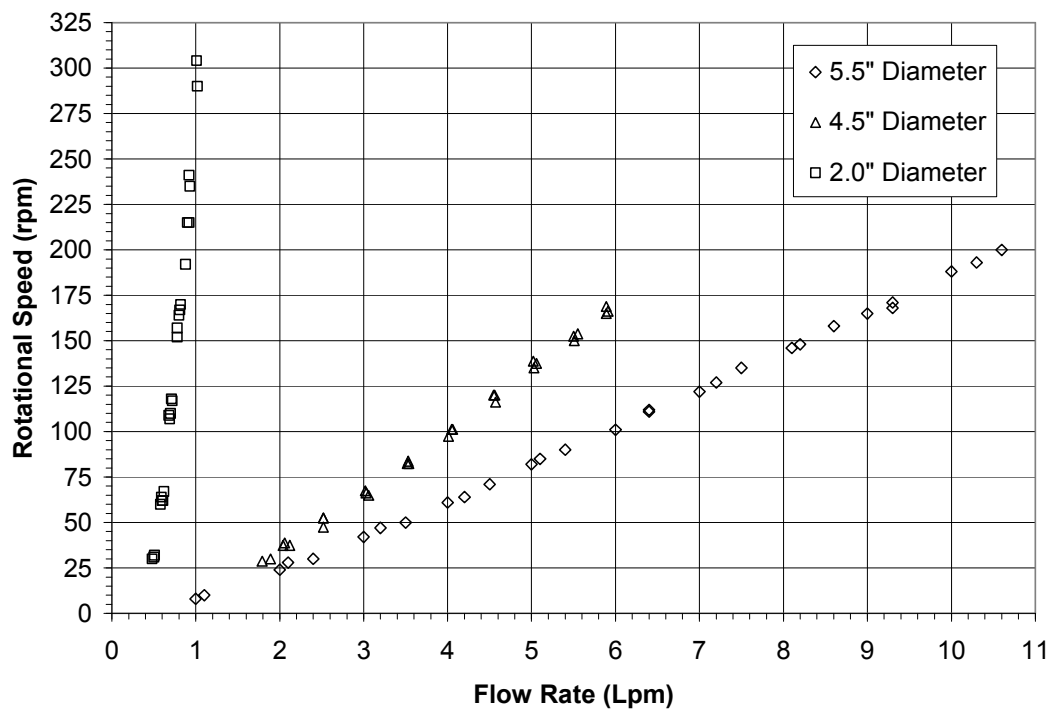
Fig. 4.4 All Rotational Speed Data from Ground Testing

In Fig. 4.4, the rotational speed data from all separators are shown. Of interest is the manner in which separator size influences the effect of flow rate on rotational speed. As mentioned previously, the smallest separator is very sensitive to inlet flow rate,

increasing from approximately 30 rpm to 300 rpm from a flow rate increase of about 0.5 Lpm, or an average rate of increase of 550 rpm/Lpm. The larger separators increase at a slower rate, with the 11.4 cm separator increasing at an average rate of 35 rpm/Lpm and the 14 cm separator increasing at 21 rpm/Lpm.

The dependence of this rate on separator size is related to shear losses at the separator wall. During separator operation, rotational speed results from the balance between the momentum lost to shear at the wall and the momentum provided by the inlet flow. The total shear loss along the separator wall, τ_{total}, depends on the dynamic viscosity of the liquid, the tangential velocity gradient with respect to radial position within the viscous layer, and the separator wall surface area[10], shown as Eq. (4.1).

$$\tau_{total} = \mu \iint_{A_s} \frac{dv_\theta}{dr} dA_s \qquad (4.1)$$

For these tests, the liquid viscosity does not change. However, separator radius affects both the tangential velocity magnitude near the separator wall and the surface area available for shear losses. Assuming the rotational flow outside of the viscous layer behaves as a rigid body, the tangential velocity near the wall behaves as Eq. (4.2).

$$v_\theta(R) = 2\pi R \omega \qquad (4.2)$$

The constant, 2π, results from the rotational speed, ω, units of rotations per second. The tangential velocity gradient within the viscous layer is approximated linearly, as shown in Eq. (4.3), by defining a viscous layer thickness, l.

$$\frac{dv_\theta}{dr} \cong \frac{v_\theta}{l} = \frac{2\pi R\omega}{l} \tag{4.3}$$

Eq. 4.1 is then approximated by Eq. (4.4).

$$\tau_{total} \cong \mu\left(\frac{2\pi R\omega}{l}\right)A_s = \mu\left(\frac{2\pi R\omega}{l}\right)\left(4\pi R^2\right) = \frac{\mu}{l}8\pi^2 R^3\omega \tag{4.4}$$

Recalling the assumption that, for steady state operation, the total shear loss along the wall is equivalent to the inlet momentum rate, Eq. (4.4) can be rewritten as Eq. (4.5).

$$\omega = \frac{l}{\mu}\frac{\dot{p}}{8\pi^2 R^3} \tag{4.5}$$

Assuming the viscous layer thickness changes are negligible relative to the separator radius for varying inlet momentum rate, this equation indicates that the effects of inlet momentum rate on rotational speed are proportional to the cube of the separator radius. Table 4.1 investigates this relationship.

Table 4.1 Comparison of R^3 Ratio and Flow Rate to Rotational Speed Ratio

Separator Diameter (cm)	R^3 Ratio Compared to			Flow Rate to Rotational Speed Ratio Compared to		
	5.1 cm Separator	11.4 cm Separator	14.0 cm Separator	5.1 cm Separator	11.4 cm Separator	14.0 cm Separator
5.1	-	0.088	0.048	-	0.064	0.038
11.4	11.4	-	0.55	15.7	-	0.6
14.0	20.8	1.83	-	26.2	1.67	-

The relationship between the two ratios suggests separator radius contributes considerably to the effect of flow rate on rotational speed. This supports the relationship between inlet flow rate, rotational speed, and separator size depicted by Table 4.1 and Fig. 4.4. The inlet momentum rate is determined by the inlet flow rate and nozzle characteristics, as discussed in the theory section and described by Eq. 2.41. Understanding the manner in which this rate relates to the angular momentum of the rotating flow is the key to predicting separator performance. While Eq. 4.5 is a useful approximation for explaining the effect of separator size on rotational speed, a more detailed investigation is necessary to resolve how momentum is transferred from the inlet flow to the rotating fluid body. The CFD method described in the previous sections is used to provide this detail.

Tangential Velocity Profiles of CFD Models

The main goal of the CFD analysis was to determine the tangential velocity profile of the rotating flow during steady state operation. Six different separator designs were

modeled and the resulting tangential velocity profiles are displayed in the order listed in

Table 4.2.

Table 4.2 CFD Case Parameters and Associated Tangential Velocity Profiles

Case	Separator Diameter	Nozzle Outlet Dimensions (Width x Height)	Inlet Flow Rate	Results Figure
20W058	5.1 cm	0.457 mm x 4.57 mm	0.58 Lpm	4.6
20W080	5.1 cm	0.457 mm x 4.57 mm	0.8 Lpm	4.7
45W200	11.4 cm	1.02 mm x 10.2 mm	2 Lpm	4.8
45W300	11.4 cm	1.02 mm x 10.2 mm	3 Lpm	4.9
45W400	11.4 cm	1.02 mm x 10.2 mm	4 Lpm	4.10
45W500	11.4 cm	1.02 mm x 10.2 mm	5 Lpm	4.11
45W1000	11.4 cm	1.02 mm x 10.2 mm	10 Lpm	4.12
45R200	11.4 cm	0.330 mm x 10.2 mm	2 Lpm	4.13
45R300	11.4 cm	0.330 mm x 10.2 mm	3 Lpm	4.14
45R400	11.4 cm	0.330 mm x 10.2 mm	4 Lpm	4.15
55W200	14.0 cm	1.24 mm x 12.4 mm	2 Lpm	4.16
55W600	14.0 cm	1.24 mm x 12.4 mm	6 Lpm	4.17
55W630	14.0 cm	1.24 mm x 12.4 mm	6.3 Lpm	4.18
55W1000	14.0 cm	1.24 mm x 12.4 mm	10 Lpm	4.19
55R600	14.0 cm	0.404 mm x 12.4 mm	6 Lpm	4.20

The results shown in the following figures were averaged azimuthally by the program

found in Appendix A.1 and plotted for varying axial distances from the liquid outlet side

of the separator with the radial position, measured from the axis of the separator cylinder

to separator wall, along the abscissa and tangential velocity along the ordinate. Each

figure is labeled according to separator diameter, nozzle outlet dimensions, and inlet flow rate.

Each line in these figures represents the azimuthal average of the tangential velocity as a function of radial distance for specific axial positions. These positions are measured from the baffle plate to the gas outlet side of the separator. Three colors denote positions within axial regions of the separator: blue marks the region from the baffle plate to the axial location where nozzle effects occur, green is the axial region which experiences the most noticeable nozzle flow effects, and red indicates the region beginning at the axial position where nozzle effects become minimal and extending to the gas outlet side of the separator. These regions and their corresponding color are shown below in Fig. 4.5.
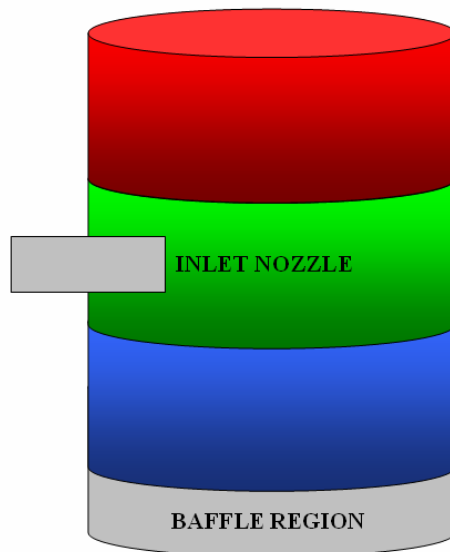
Fig. 4.5 Axial Regions and Corresponding Color Used in Results Figures
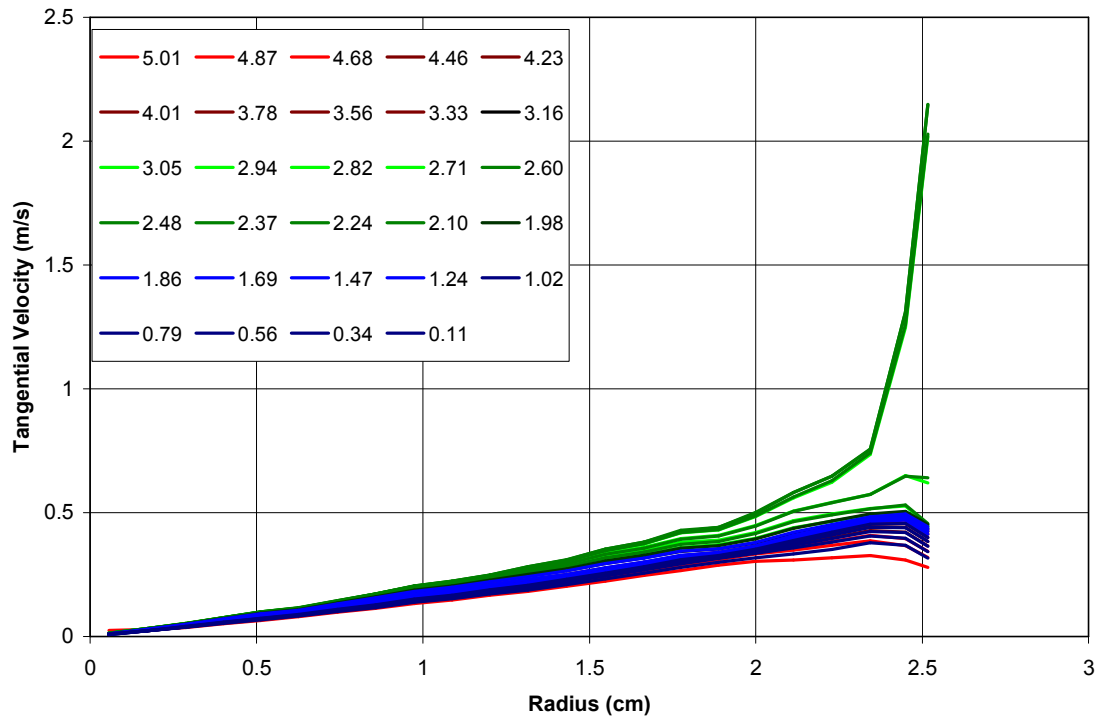
Fig. 4.6 Tangential Velocity for Varying Axial Position, 5.1 cm Diameter Separator,

0.58 LPM, Nozzle 0.452 mm x 4.52 mm

The results for CFD case 20W058 are shown in the Fig. 4.6. A maximum tangential

velocity of 2.2 meters per second was achieved at the axial position of 2.5 cm and radial

position of 2.5 cm. This location is at the wall of the separator and midline of the nozzle

outlet. At this same axial location but at a radius of 2.3 cm, the tangential velocity has

reduced to 0.74 meters per second. Overall, the average for tangential velocity over the

entire separation volume is 0.23 meters per second, indicating this region contains

considerably higher velocities than found in the remainder of the separation volume.

This region of high velocity is a direct result of the inlet nozzle. As the radial position

moves towards the central axis of the separator and away from the outlet of the nozzle, the tangential velocities at each axial position converge. Furthermore, these velocities become linear away from the inlet effects, although they assume slightly different slopes. This behavior indicates that most of the flow within the separation volume is traveling with approximately the same rotational speed, with the exception of the higher velocity band resulting from the inlet flow. For this case, the inlet flow band exists from a radial position of 2 cm to the wall, 20% of the separator radius, and between the axial locations of 2 and 3 cm, 20% of the separator height.

Fig. 4.7 Tangential Velocity for Varying Axial Position, 11.4 cm Diameter Separator, 3 LPM, Nozzle 1.02 mm x 10.2 mm

Case 45W300, profile shown in Fig. 4.7, is a larger model than the previous case, 11.4 cm in diameter, with an inlet flow rate of 3 liters per minute. This flow rate resulted in a maximum velocity of 2.3 meters per second with an average of 0.28 meters per second. Despite the increase in separator size, the shape of the tangential velocity profile remains similar to the previous case.

Fig. 4.8 Tangential Velocity for Varying Axial Position, 11.4 cm Diameter Separator, 3 LPM, Nozzle 0.330 mm x 10.2 mm

Case 45R300, shown in Fig. 4.8, is the same separation volume size and inlet flow rate as the previous model but with a smaller nozzle aspect ratio, a result of thinning the nozzle outlet width from 1.02 mm to 0.33 mm. This flow rate resulted in a maximum

velocity of 4.4 meters per second with an average of 0.55 meters per second. For comparison, the wider nozzle from case 45W300 produced a maximum velocity of 2.3 meters per second and an average of 0.28 meters per second.

The increase of maximum tangential velocity as nozzle outlet area decreases is expected as, although these two models have the same inlet flow, the smaller area results in an inlet flow with higher velocity. However, this increase in tangential velocity does not restrict itself to the high velocity band resulting from inlet flow effects but increases velocity throughout the separator, nearly doubling the average tangential velocity. This relationship indicates that nozzles with smaller areas provide higher rotational speeds within the separator, resulting in higher centripetal acceleration and improved separator performance. Counteracting this benefit, however, is the pressure drop through the nozzle. As nozzle outlet area decreases, pressure drop rises. The optimum design point, then, should be found in the balance of nozzle pressure drop, inlet flow rate, and nozzle outlet area.

Furthermore, in order to minimize the effects of the high velocity band resulting from the inlet nozzle effects, nozzle area reduction should be achieved by reducing the nozzle outlet thickness rather than nozzle outlet height. This consideration stems from the fact that a wider nozzle would extend the high velocity band closer to the gas core region of the separator and further disrupt the flow symmetry of the MVS. This concept will be discussed further in the Tangential Velocity Results Comparison section.
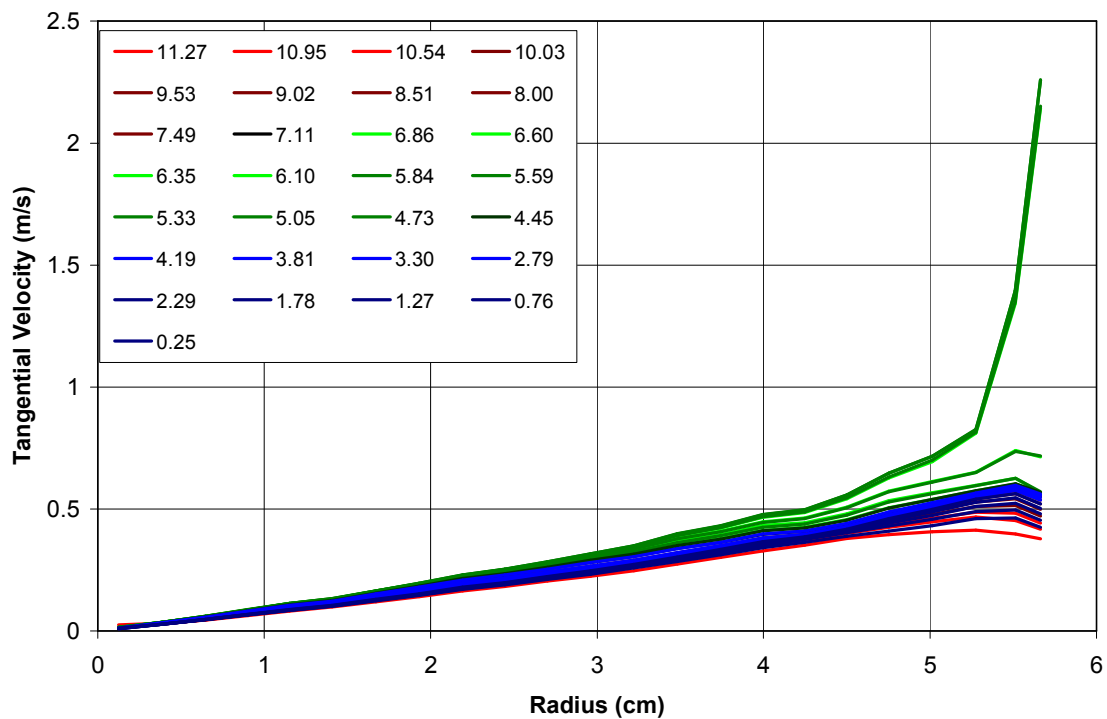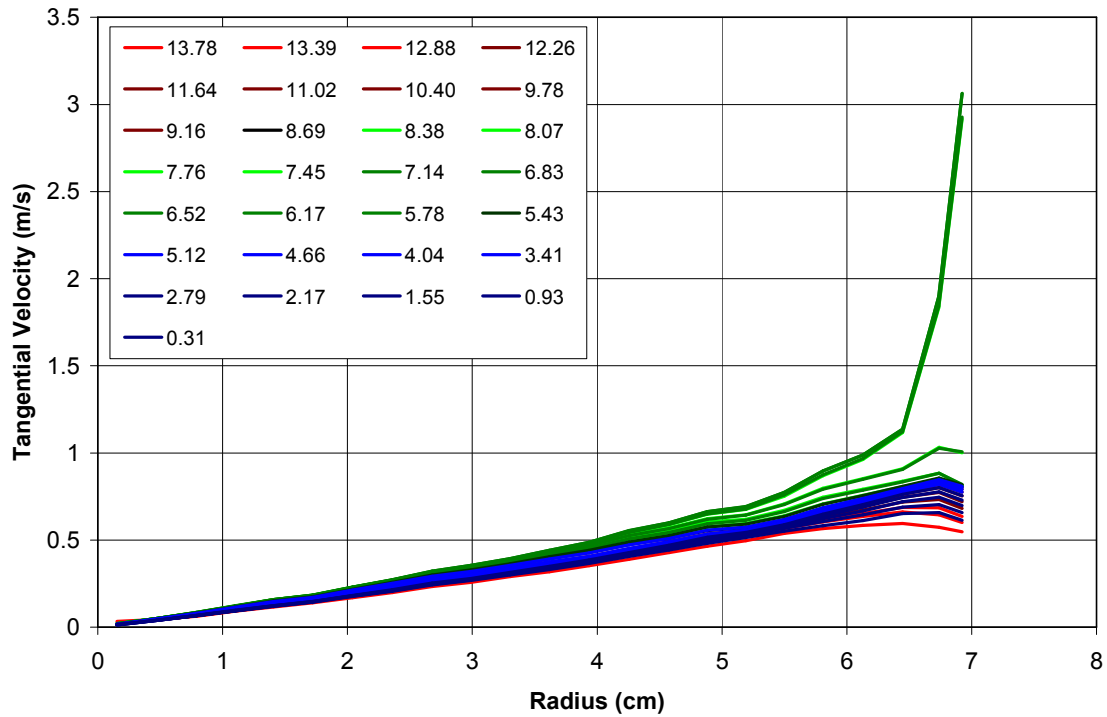
Fig. 4.9 Tangential Velocity for Varying Axial Position, 14.0 cm Diameter Separator, 6

LPM, Nozzle 1.24 mm x 12.4 mm

Case 55W600, shown in Fig. 4.9, is a larger model than the previous cases, 14.0 cm in diameter, with an inlet flow rate of 6 liters per minute. This flow rate resulted in a maximum velocity of 3.1 meters per second with an average of 0.39 meters per second. Again, the velocity profile remains similar to the preceding cases.
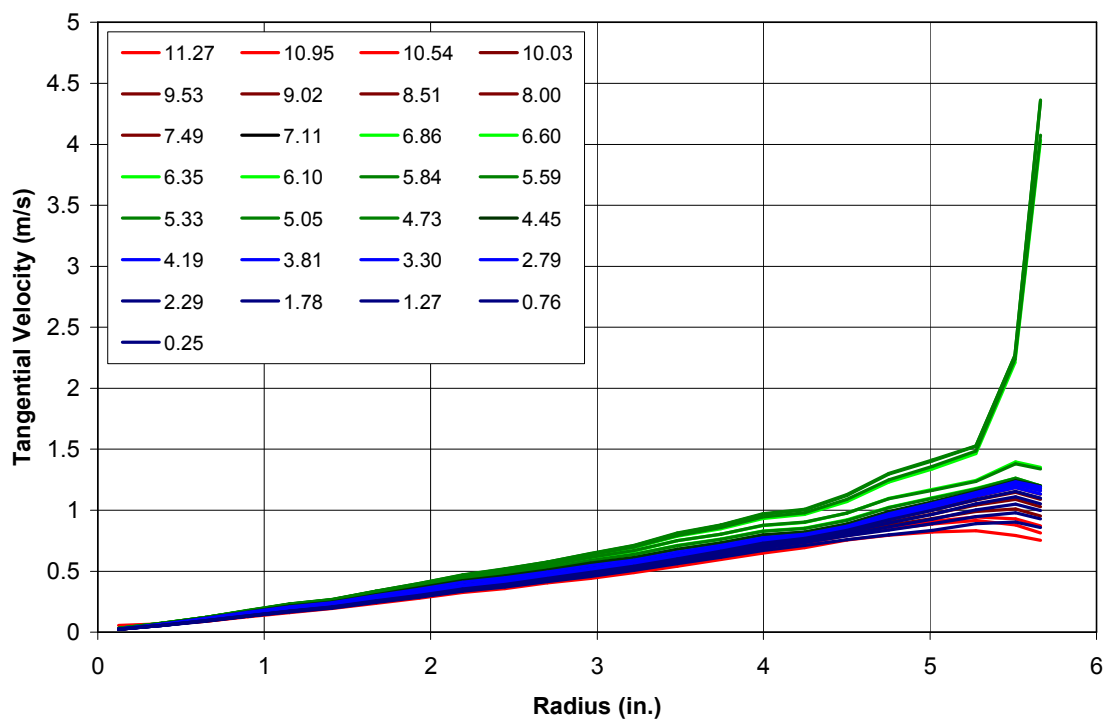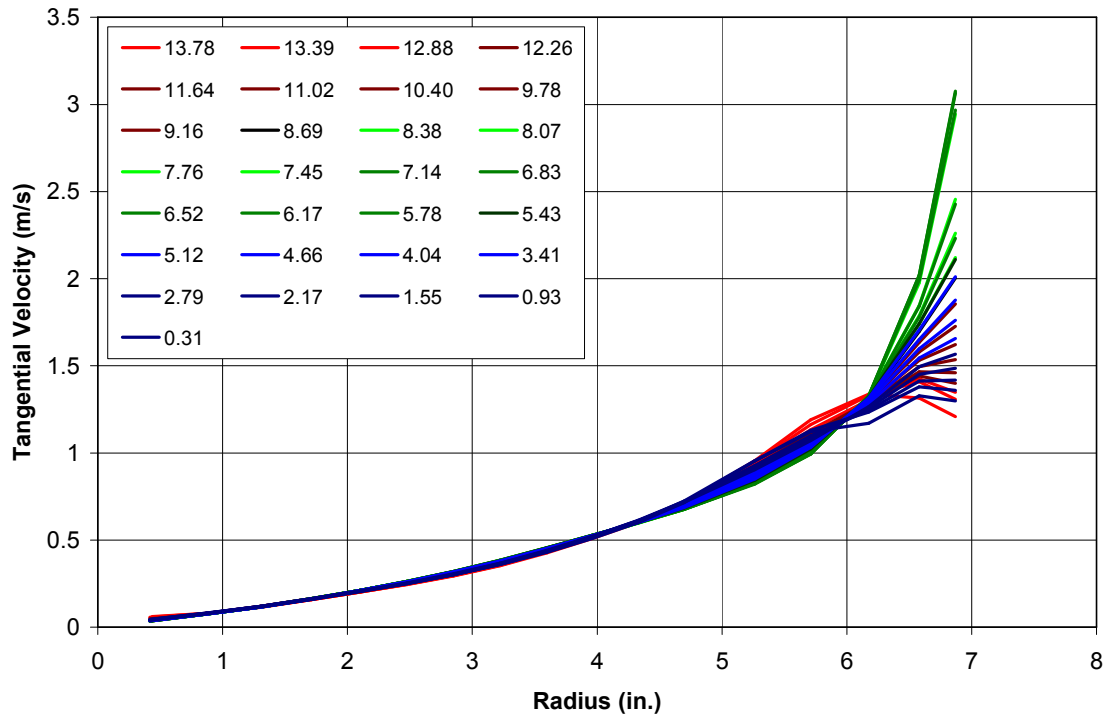
Fig. 4.10 Tangential Velocity for Varying Axial Position, 14.0 cm Diameter Separator,

6 LPM, Nozzle 0.404 mm x 12.4 mm

Case 55R600, shown in Fig. 4.10, is the same in separation volume size as the previous model but with a smaller nozzle aspect ratio, a result of thinning the nozzle outlet width from 1.24 mm to 0.404 mm. This case achieved a maximum velocity of 3.1 meters per second with an average of 0.62 meters per second. For comparison, the wider nozzle from case 55W600 produced a maximum velocity of 3.1 meters per second and an average of 0.39 meters per second. Unlike the 11.4 cm diameter separator, the narrow nozzle case produced a maximum velocity equivalent to the wider nozzle. The overall average velocity, however, did increase as seen in the smaller model.

The tangential velocity profile determined for this case is unlike any of the previous results. The inlet nozzle effects spread nearly along the entire axial region at the wall of the separator. Furthermore, outside of this region, the tangential velocity profiles approach each other more rapidly than previous cases and do not behave in a linear fashion as radial position approaches the central axis of the separation chamber. For a rotating flow, a non-linear velocity profile indicates a departure from rigid body rotation. This change in behavior is not fully understood.

The major difference between case 45R400 and 55R600 is the rotational flow volume compared with the nozzle outlet area. As the radius of a separator design increases, the flow volume within the separation volume increases as the cube of the radius. The nozzle dimensions for these cases were scaled as a percentage of separator radii, using the 11.4 cm diameter separator as the base for the scale. As a result, the inlet area increases as the square of the separator radius. The difference in the tangential velocity profile for this case may be a result of the separation volume increasing more rapidly than the nozzle outlet area. With this in mind, achieving similar performance between separators may require the nozzle to be scaled to this volume.

Tangential Velocity Results Comparison

To further examine the effects of flow rate, separator size, and nozzle outlet area on tangential velocity, the results from each model are compared below. Tangential results from each separator, at axial planes 24% above the separation volume midplane, are displayed in the following figures. Separator models of similar radius are investigated together in Figs. 4.11 to 4.13, with radial position along the abscissa and tangential velocity, averaged azimuthally, along the ordinate.
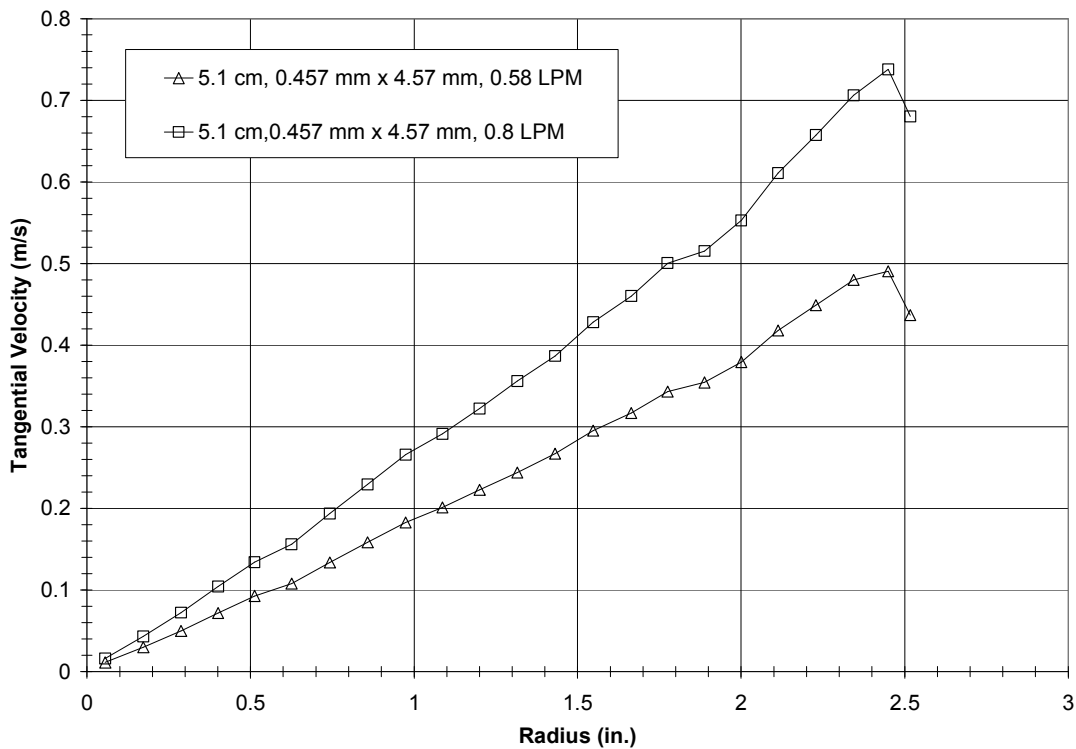
Fig. 4.11 Comparison of Tangential Velocity Results for the 5.1 cm Diameter Model

Fig. 4.11 demonstrates the increase in overall velocity resulting from increased flow rate. Each line represents a different CFD case for the 5.1 cm diameter separator as shown in the legend. In this case, a maximum velocity gain of 0.24 meters per second is achieved from a flow rate increase of 0.22 liters per minute. This gain decreases as radial position approaches the central axis of the separation volume.
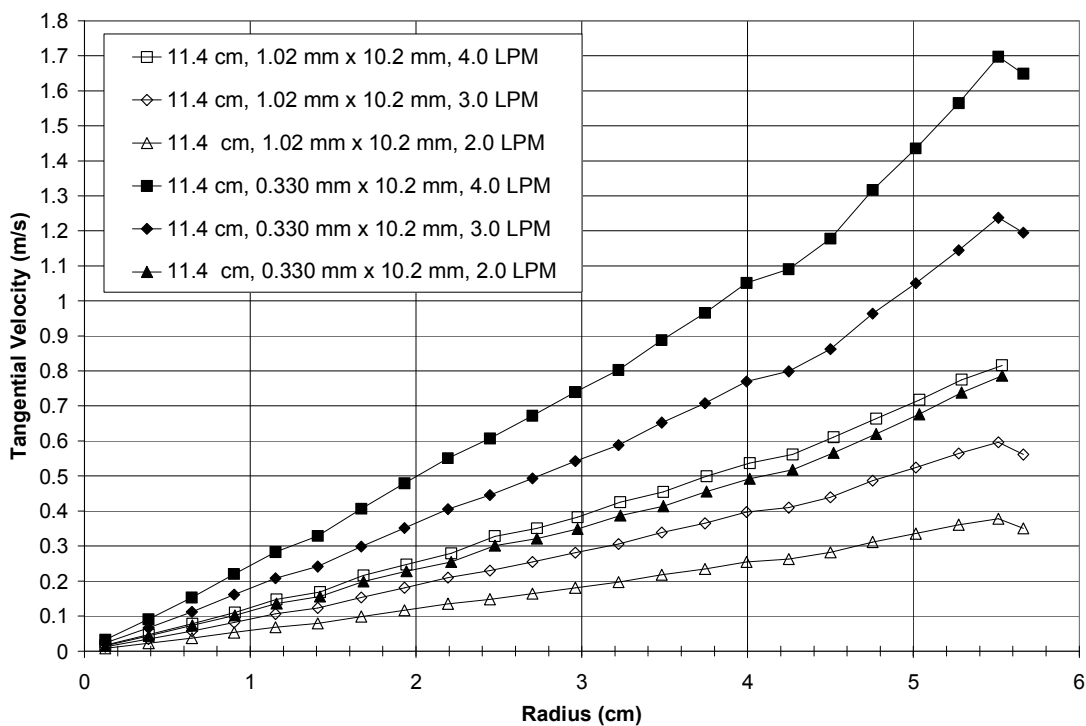
Fig. 4.12 Comparison of Tangential Velocity Results for the 11.4 cm Diameter Model

Fig. 4.12 demonstrates both the effect of increasing inlet flow rate as well as adjusting nozzle outlet area. The lines marked with filled shapes indicate tangential velocity results for the narrow nozzles, 0.330 mm in width, while those not filled denote results for the wider nozzles, 1.02 mm. Each line represents a different CFD case for the 11.4

cm diameter separator as denoted by the legend. Case 45W400, a wide nozzle with 4 liters per minute of inlet flow, and case 45R200, a narrow nozzle with 2 liters per minute of inlet flow, are good examples of the effect of nozzle width on tangential velocity. 45W400 produces slightly more tangential velocity, with a maximum of 0.8 meters per second, than 45R200 but at twice the flow rate. Case 45R400, a narrow nozzle with 4 liters per minute of inlet flow, achieves a maximum velocity of 1.7 meters per second, twice that of the wider nozzle. For the same flow rate, a decrease in nozzle width of 67.5% resulted in doubling the maximum tangential velocity within the separation volume.
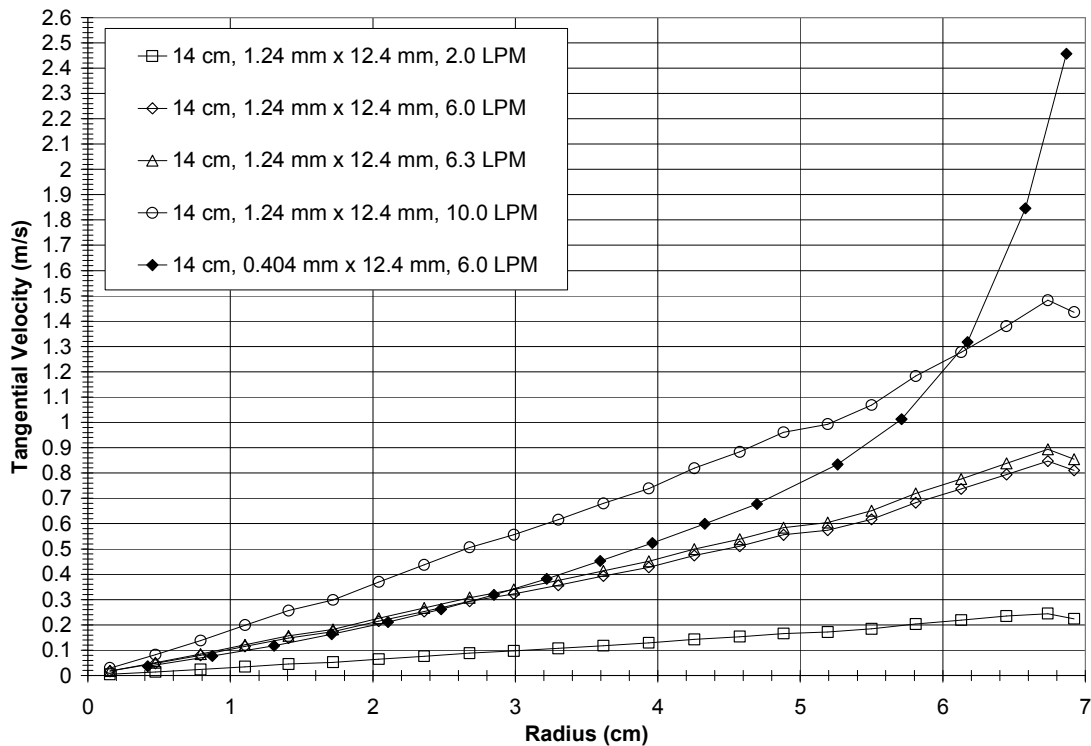
Fig. 4.13 Comparison of Tangential Velocity Results for the 14 cm Diameter Model

Fig. 4.13 provides a closer look at the velocity profile of the narrow nozzle, 14 cm diameter separator design, case 55R600, compared with the wide nozzle cases of the same diameter, cases 55W200 through 55W1000. The line marked with filled shapes indicates tangential velocity results for the narrow nozzle, 0.404 mm in width, while those not filled denote results for the wider nozzles, 1.24 mm. Each line represents a different CFD case for the 14 cm diameter separator as denoted by the legend. The narrow nozzle case for this diameter shows inlet nozzle effects persisting at this axial location, while the wider nozzles show little effect. As the narrow nozzle case approaches the central axis of the separation volume, the tangential velocities approach those of the wider nozzle cases of the same inlet flow rate. However, the approach to this axis is not a linear velocity profile as seen in all other cases. Furthermore, unlike the 11.4 cm diameter cases, the narrow nozzle, 14 cm diameter case does not result in higher tangential velocities at the inner radial positions. These higher velocities are found, instead, at the outer radial positions, a result of the inlet nozzle effects spreading axially rather than radially. Comparing cases 55R600 and 55W600, the maximum velocity achieved by the narrow nozzle case is 2.5 meters per second with the wide nozzle case reaching 0.8 meters per second. This is an increase of 212.5%, considerably higher than the 100% increase achieved by the narrow nozzle, 11.4 cm diameter cases. Despite the altered tangential velocity profile, the average tangential velocity increased with the narrow nozzle, 14 cm diameter case in a manner consistent with the narrow nozzle, 11.4 cm diameter cases. This result indicates that although the momentum transfers through the rotational flow in a different manner, the overall momentum transfer remains similar.

In the following section, the region affected by the inlet nozzle will be explored more closely using case 45R400. This case is a 11.4 cm diameter separator with a nozzle of width 0.33 mm and height 10.2 mm operating with an inlet flow rate of 4 liters per minute. The cell centered tangential velocity results are examined along the plane shown in Fig. 4.14.
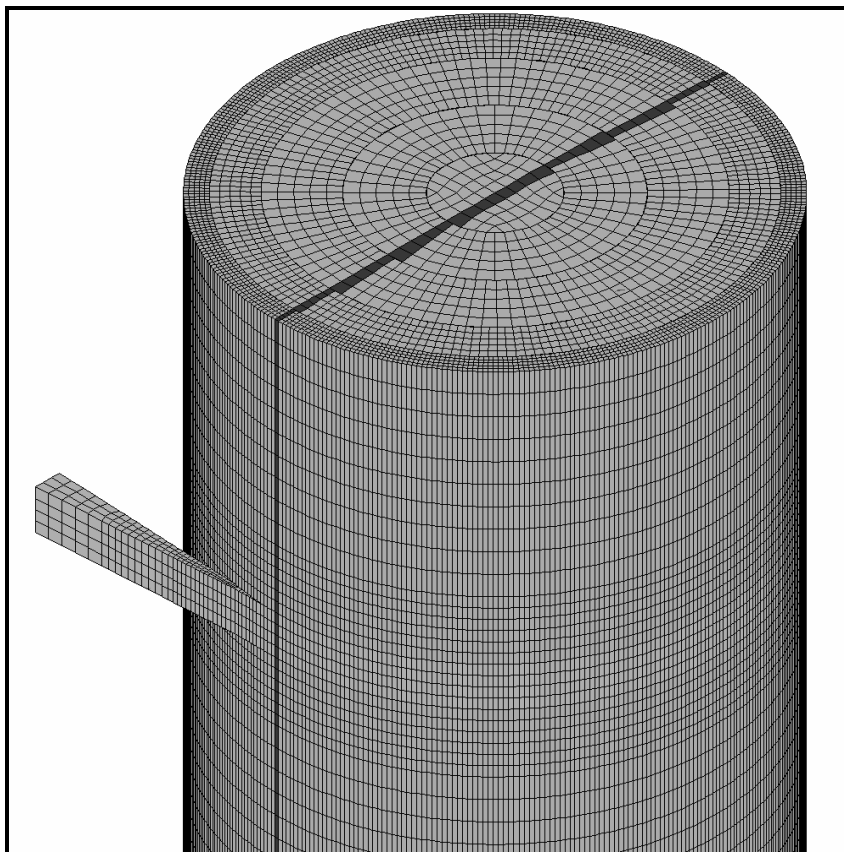
Fig. 4.14 Selected Cell Plane Orientation

Radial position is measured from the central axis, with positive position directed towards the nozzle and negative towards the separator wall opposite the nozzle. Axial plane location is measured from the separator mid-plane, shown in Fig. 4.15.
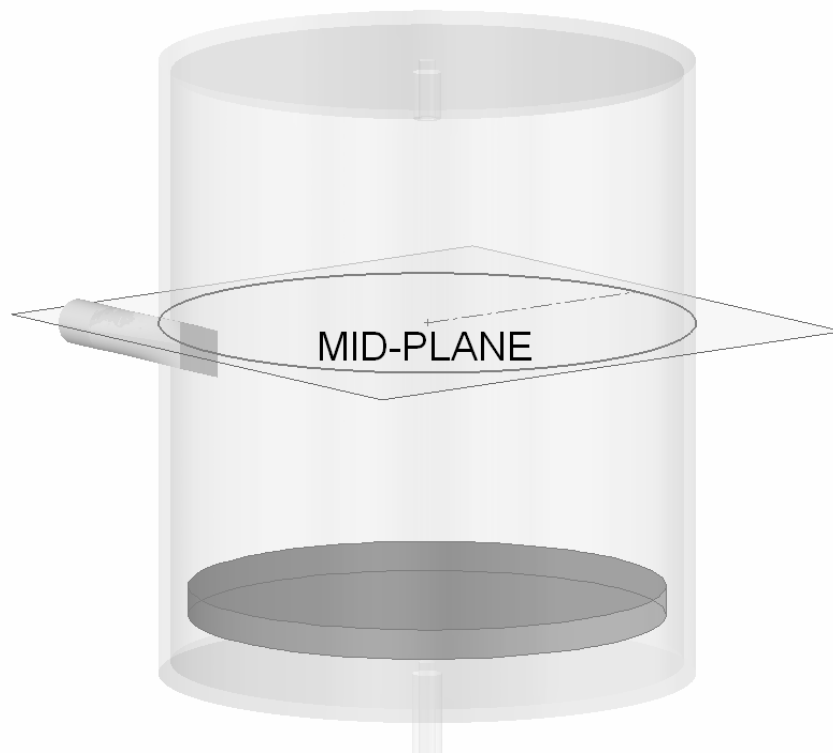
Fig. 4.15 Location of Separator Mid-plane

The tangential velocity values about the mid-plane are examined for case 45R400, shown in Fig. 4.16. As the region affected by inlet effects is symmetric about this plane, the following figures show the tangential velocity profiles at 0.2, 0.4, 0.6, 1.2, and 1.8 inches below the mid-plane.
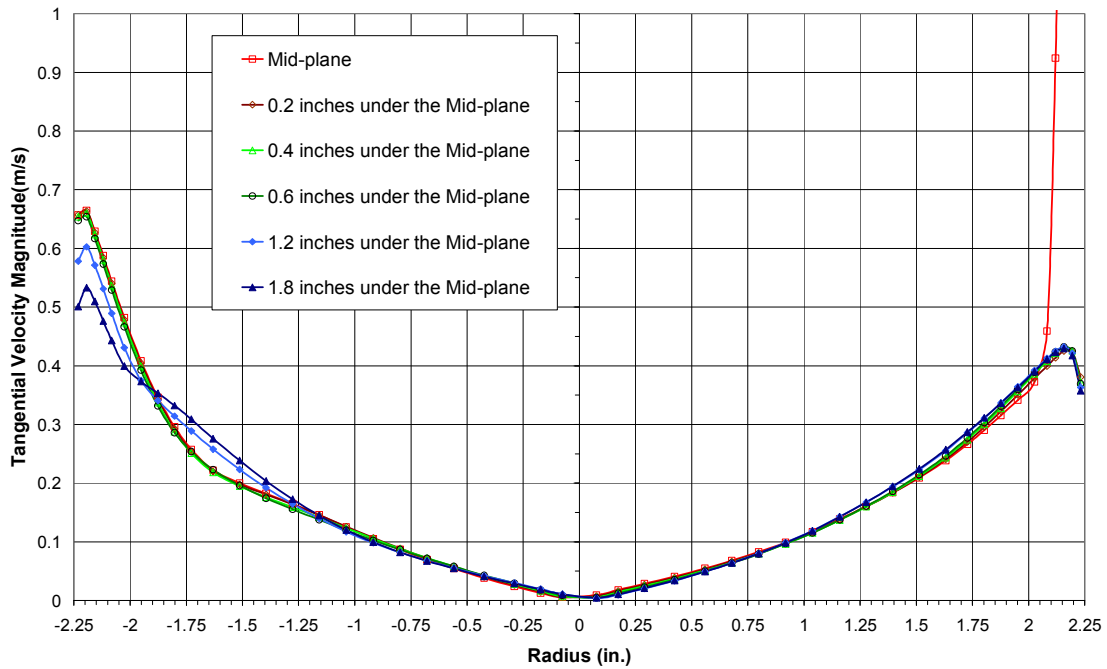
Fig. 4.16 Cell-centered Tangential Velocity at the Separator Mid-plane

The highest velocity occurs at the mid-plane and is a result of the inlet effects. At 0.2 inches below the mid-plane, the inlet effects are no longer evident on the nozzle outlet side, or right hand side of the figure. However, opposite the nozzle outlet, the tangential velocity achieves the highest value in this region. As axial position moves away from the mid-plane, this tangential velocity decreases. On the right hand side, all axial planes aside from the mid-plane produce nearly identical velocity profiles. Overall, this behavior indicates the high velocity region associated with the inlet spreads axially as the flow moves radially about the separator axis, producing a velocity profile that becomes more symmetric as the central separator axis is approached. Symmetry is important in this region as the gas core resides in the inner radial positions of the

separator and asymmetric flow patterns would result in undesirable instabilities. To further illustrate this occurrence, a contour map of the tangential velocity values near the separator wall is shown in Fig. 4.17.
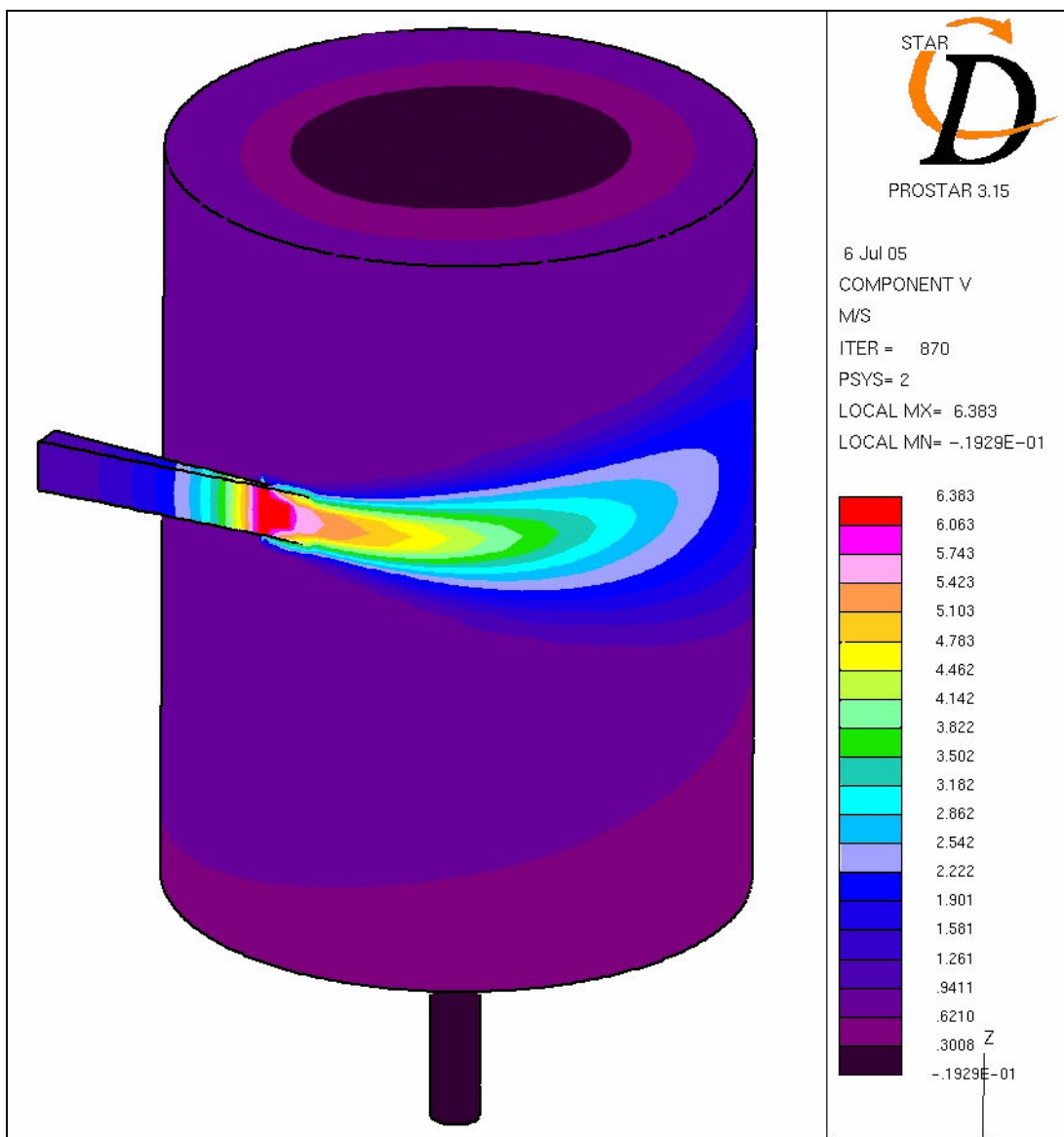
Fig. 4.17 Tangential Velocity Contour Plot for Case 45W400

At 90 degrees counter-clockwise from the nozzle entrance, the tangential velocity has decreased from 6.4 meters per second to approximately 1.5 meters per second, a value below the azimuthal average of 2 meters per second. Again, the high velocity nozzle effects are shown to diminish rapidly as position moves away from the nozzle outlet.

In the following section, the CFD results are validated against the ground testing data. As much of the tangential velocity analysis is based on these results, the correlation between the computational and real world values determines the strength of the arguments presented here.

Data and Results Comparison

The cell-centered tangential velocity results were averaged over the separation volume to produce an average rotational speed for each case. These averages are compared with the ground data in Fig. 4.18.
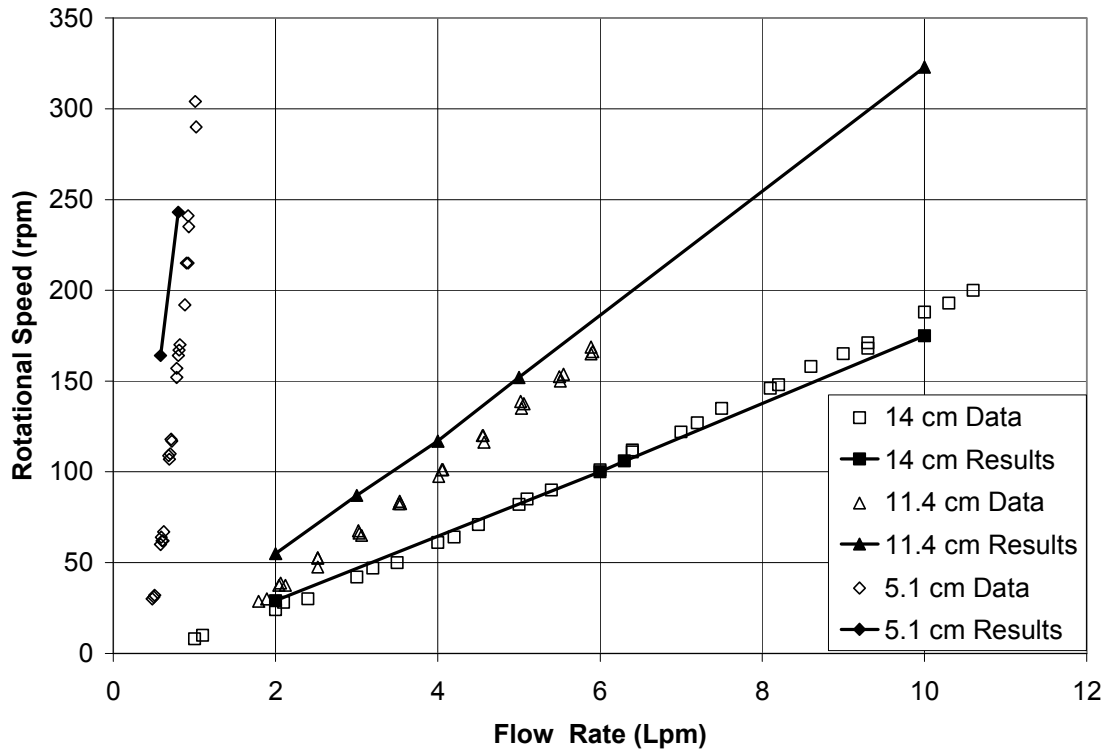
Fig. 4.18 Comparison of Rotational Speed Results and Data

The solid markers and lines denote the CFD results while the hollow markers reference the ground data. Each separator size uses equivalent shapes as markers. The figure shows that the CFD results from the 14 cm diameter separator compare well with the ground test data, reaching a maximum error of about 10 rpm at the higher flow rates. Both the 5.1 cm and 11.4 cm diameter CFD results are less favorable and over predict the ground test data. For the 11.4 cm diameter cases, the maximum error occurs at the lower flow rates and is on the order of 20 rpm. The 5.1 cm diameter cases, however, have a maximum error of 100 rpm. This error is likely a result of the instrumentation used to monitor rotational speed and flow rate during the ground testing. The precision

of the flow meter, discussed previously, could lead to errors of up to 25 rpm for the 5.1 cm diameter separator. Furthermore, since the paddle wheel assembly adds another momentum loss mechanism to the system due to friction within the bearing, this method may have been too intrusive for use with this separator. Fig. 4.19 shows the effects on rotational speed resulting from changing inlet momentum rate for all three separator sizes.
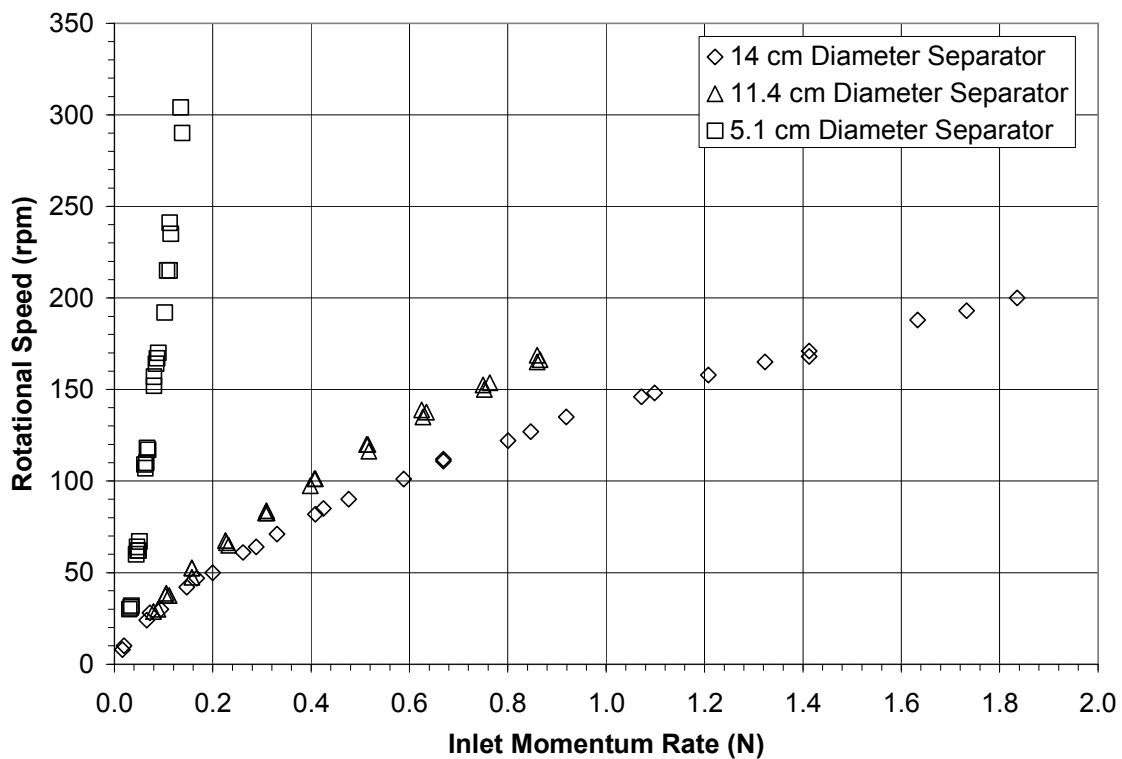
Fig. 4.19 Effects of Changing Inlet Momentum Rate for Varying Separator Size

The additional loss mechanism produced by the paddle wheel assembly would, in effect, be similar to reducing the inlet momentum rate of a separator operating without the

assembly. For the larger separators, a small reduction in inlet momentum rate has little effect.

For the larger separators, this additional loss mechanism is not as significant as the total momentum loss due to shear along the separator wall. However, recalling that during steady state operation the inlet momentum rate balances with the separator loss mechanisms, Fig. 4.19 shows that a small change in inlet momentum rate results in a considerable change in rotational speed. For example, a 0.01 N change results in a rotational speed change of approximately 25 rpm. The 11.4 cm diameter separator, on the other hand, shows a change of about 2 rpm and the 14 cm diameter separator shows even less change. As a result, the larger separators are less sensitive to the additional loss mechanism introduced by the paddle wheel assembly than the 51 cm diameter separator. In future tests, rotational speed and flow rate monitoring devices must take this sensitivity into account.

Aside from potential instrumentation errors, the sensitivity of the smaller separators to momentum balance could affect the CFD calculations as well. Errors intrinsic in the finite volume approximation could be significant enough to produce erroneous results. In the same manner described in the preceding paragraph, larger separators would be affected less by momentum balance errors than smaller separators. The discrepancy between the 5.1 cm diameter results and data will be examined further in the next section.

Buckingham Pi Theorem Relationship

The Buckingham Pi relationship developed in the theory section was tested using both the ground data and CFD results, including appropriate model parameters for each, shown in Fig. 4.20.
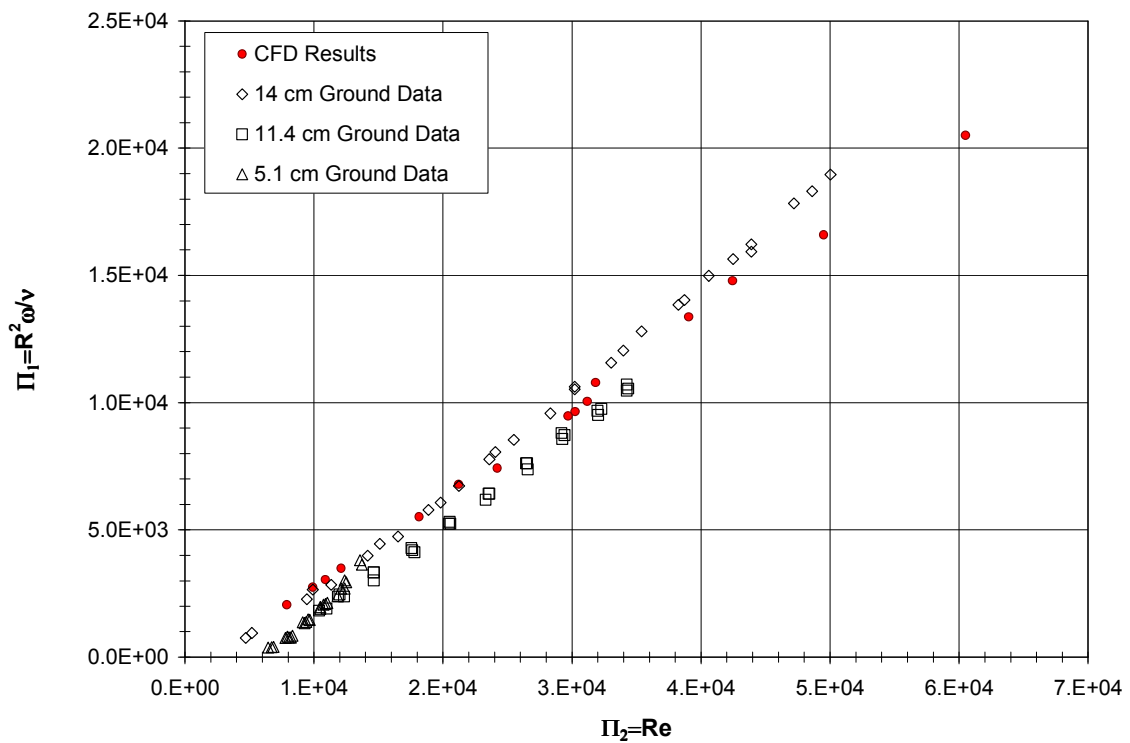
Fig. 4.20 Buckingham Pi Relationship

The data and results both show a linear relationship between the Reynolds number at the nozzle and the rotational flow Pi group, Π_1. As seen in Fig. 4.19, the 14 cm diameter ground data compares most closely with the CFD results, while the 11.4 cm and 5.1 cm diameter ground data shares slightly less of a resemblance to these results. Despite

varying separator diameter, flow rate, nozzle outlet area, and rotational speed, each operational state examined, either on the ground or using CFD, follows the linear relationship between these two Pi groups relatively well.

The linear regression of these results and data, shown as Eq. (4.6), has a Pearson product moment correlation coefficient, r, of 0.99 or an r-squared of 0.98.

$$\frac{R^2\omega}{\nu} = 0.394(\text{Re}_N) - 2020.0 \tag{4.6}$$

Rearranging, a rotational speed prediction is given for associated separator parameters, shown as Eq. (4.7).

$$\omega = \frac{0.394 L_N V - 2020.0\nu}{R^2} \tag{4.7}$$

Predicted rotational speeds are compared to the ground test data in Fig. 4.21.
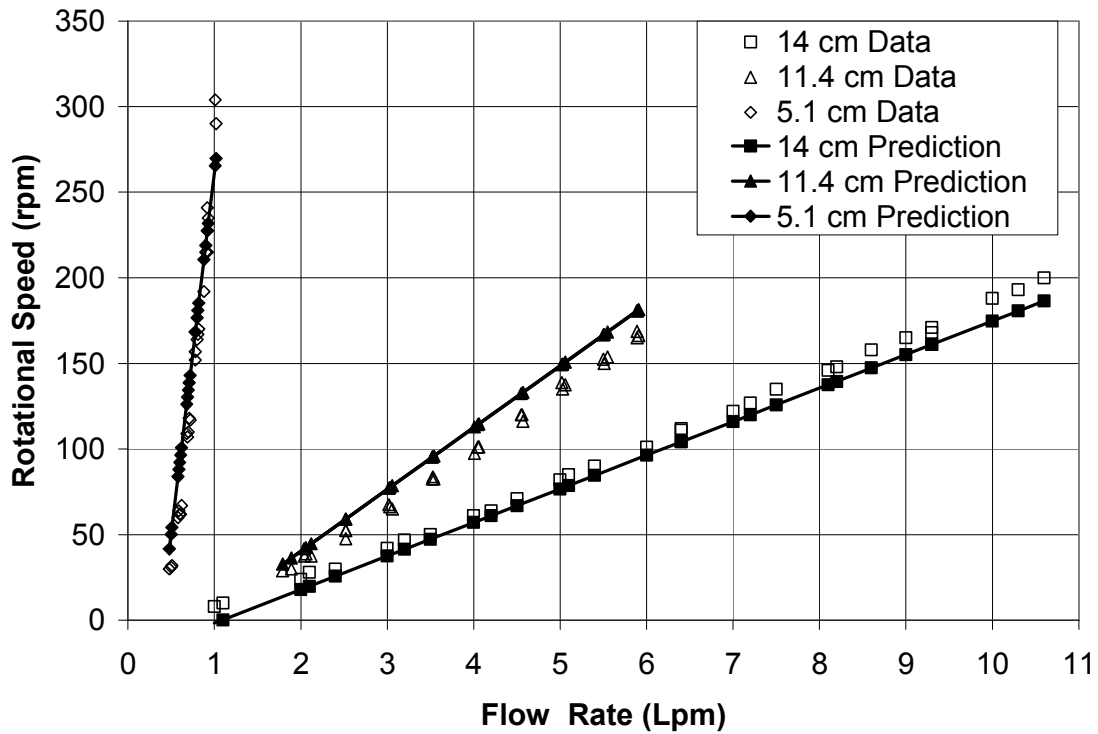
Fig. 4.21 Predicted Rotational Speeds Compared with Ground Data

The rotational speeds predicted by Eq. (4.7), shown by the lines in Fig. 4.21, compare well with their ground data counterparts, shown as the hollow markers. This equation models the separator data well. Combined with the validity of the rigid body rotation approximation provided by the CFD velocity profile results, this equation can be used to approximate tangential velocities for given separator parameters. These velocities, in turn, can be used to determine bubble transit times as shown in the following section.

Bubble Transit Time Results

Using the prediction equation from the previous section, bubble transit times for varying separator parameters can be calculated using the process described in the theory section. The code developed to perform these calculations is found in Appendix A.2. For this discussion, the 5.1, 11.4, and 14 cm diameter, wide nozzle separator model bubble transit times are calculated for varying inlet flow rate and shown in Fig. 4.22.
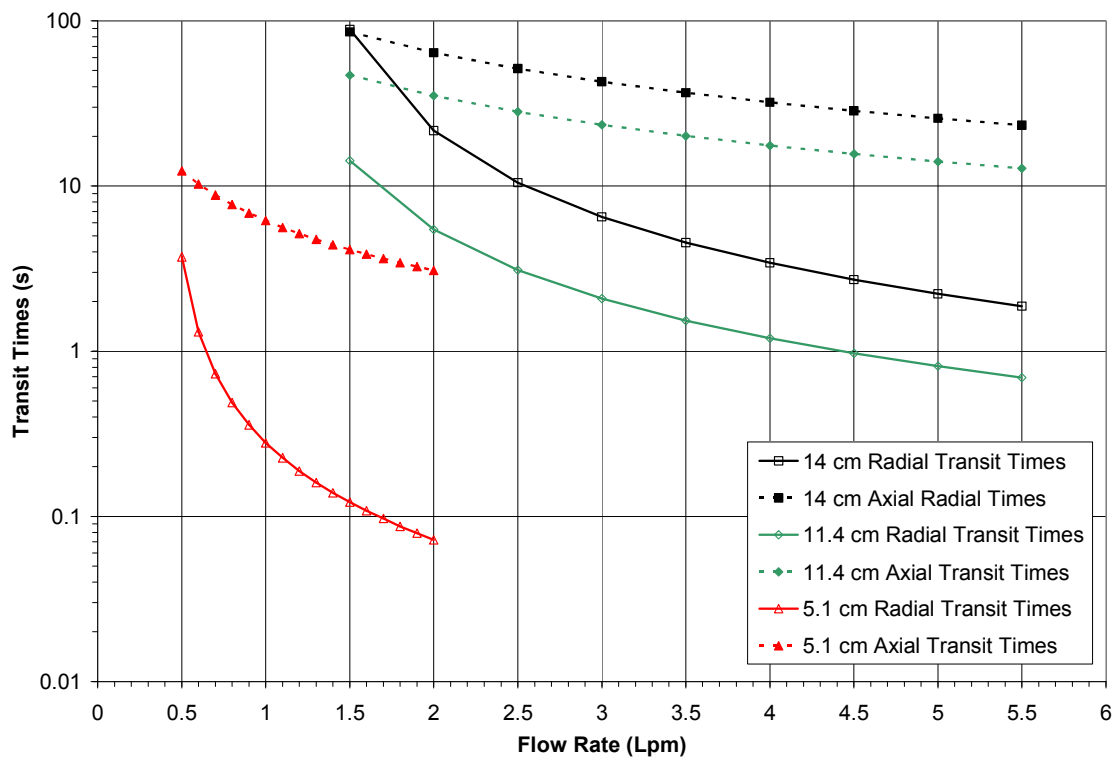
Fig. 4.22 Calculated Bubble Transit Times

The results displayed in Fig. 4.22 are for all liquid cases. As such, radial transit is from the nozzle outlet to the centerline of the separation volume. Axial transit also begins at the nozzle outlet and ends at the separator baffle location. Bubble size for these calculations was set to 1 mm, a typical size encountered in separator operation. With the exception of the lowest flow rate for the 14 cm diameter separator, axial transit time exceeds radial times. This indicates that separation will occur as the bubble reaches the centerline with little axial movement. Furthermore, as inlet flow rate increases, the difference between radial and axial transit times increases, indicating separation failure will occur at a minimum flow rate.

Introducing a gas core into the calculation will reduce both the axial flow area and radial transit distance. The effect of the gas core is examined in Fig. 4.23 for the 11.4 cm diameter separator.
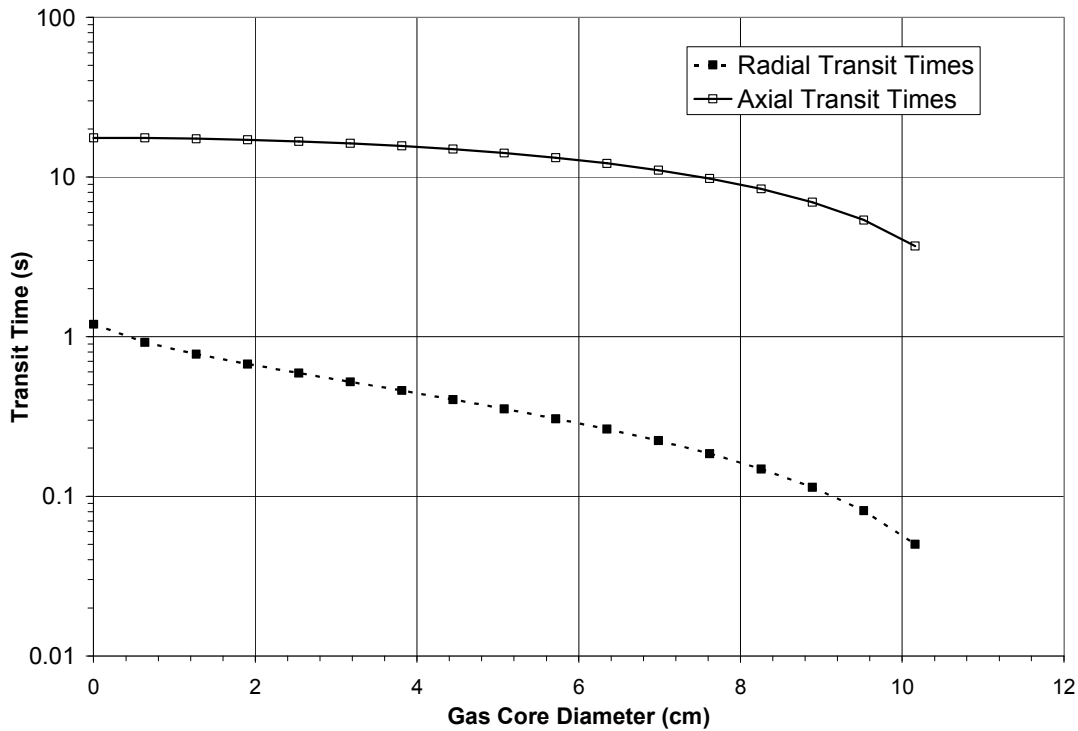
Fig. 4.23 Gas Core Diameter Effects on Transit Times

The separator model used for Fig. 4.23 is a wide nozzle case with 4 liters per minute of inlet flow. As gas core diameter increases, axial transit time begins to approach the magnitude of the radial transit times. However, even at the largest gas volume, the radial transit time remains considerably less than the axial time. Furthermore, as gas core diameter increases, radial transit time also decreases, although not as rapidly relative to the axial time decrease. To examine this effect further, the calculations completed for Fig. 4.22 are revisited but include the maximum gas core diameter for each separator model. The results are shown in Fig. 4.24.
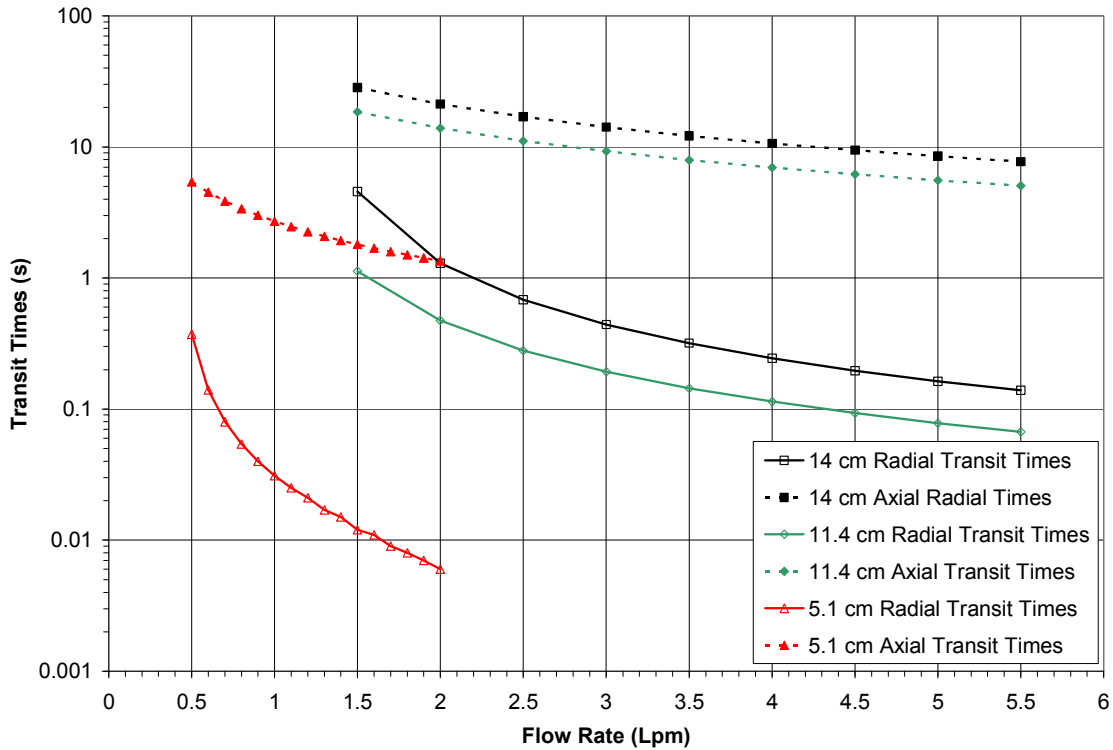
Fig. 4.24 Calculated Bubble Transit Times with Maximum Gas Core Diameter

As seen in Fig. 4.23, the axial and radial transit times have decreased considerably compared with the all liquid cases. Fig. 4.24 indicates that as the gas core diameter increases to the maximum volume, radial transit times remain below the axial transit times for the flow rates of interest. Furthermore, the ratio of axial transit time to radial transit time has increased. This effect is most noticeable for the 14 cm diameter separator at a flow rate of 1.5 liters per minute. For the all liquid case, the radial and axial transit times are nearly equivalent. For the maximum gas core case, the axial transit time is four times greater than the radial transit time. This behavior indicates that increasing gas core diameter improves the operational characteristics of the separator.

Minimum inlet flow rate, then, is found by comparing the radial and axial times of the all liquid case for a specific separator model. Maximum flow rate would depend on the pressure resources of the system.

5. CONCLUSION

In the microgravity environment experienced by space vehicles, liquid and gas do not naturally separate as on Earth. This behavior presents a problem for two-phase space systems such as environment conditioning, waste water processing, and power systems. Responding to this need, researchers have conceived various methods of producing phase separation in low gravity environments. These separator types have included wicking, elbow, hydrophobic/hydrophilic, vortex, rotary fan separators, and combinations thereof. Each class of separator achieved acceptable performance for particular applications and most performed in some capacity for the space program.

However, increased integration of multiphase systems requires a separator design adaptable to a variety of system operating conditions. To this end, researchers at TAMU have developed a separator capable of handling both a wide range of inlet conditions as well as changes in these conditions with a single, passive design. Currently, rotary separators are recognized as the most versatile microgravity separation technology. However, compared with passive designs, rotary separators suffer from higher power consumption, more complicated mechanical design, and higher maintenance requirements than passive separators. Furthermore, research completed over the past decade has shown the TAMU MVS more resistant to inlet flow variations and versatile in application.

The TAMU MVS provides reliable phase separation in microgravity environments utilizing the intrinsic momentum of the two-phase flow. Furthermore, the unique design of this separator allows the device to handle changes in inlet flow quality and rate. Coupled with a simple, passive design, integration of the MVS is possible for a variety of space systems without significant adjustment. For instance, over the past decade, the TAMU MVS found application with the IMMWPS, Boeing propellant transfer system, PEM fuel cell technology, and several other systems. In all cases, this device allowed two-phase flow loops to function in a microgravity environment. TAMU is currently extending the application of the MVS to dehumidification and heat exchange.

In order to improve the ease of system integration and allow for further optimization of the MVS design, the effects of nozzle area ratio, separator geometry, and inlet flow rate on momentum transfer and the tangential velocity distribution within the denser fluid must be understood. CFD, in the form of Adapco's Star-CD, is used in this work, along with single phase ground testing, to accomplish this goal. Furthermore, as aids to be used in conjunction with the ground data and CFD results, relationships for radial pressure, bubble transit time, and momentum transfer were developed.

Ground testing data showed a linear relationship between rotational speed and inlet flow rate. The slope of this relationship is directly related to the surface area of the separator wall and, therefore, the diameter of the separator design. Small changes in inlet flow rate have greater effect on the rotational speed of smaller separators, whereas larger

separators require a more significant change in inlet flow rate to achieve the same rotational speed gain. This is expected as smaller separators have less surface area available for momentum losses and the inlet momentum rate required to drive them is considerably less than that of the larger separators. Furthermore, this sensitivity of smaller separators with regards to momentum balance was found to demand more precise rotational speed and flow rate monitoring instruments. Even small errors in measurement could result in large discrepancies between flow rate and rotational speed.

The CFD results compared well with the ground data, with the exception of the 14 cm diameter case, and indicated that the majority of the rotational flow travels at nearly the same rotational speed. The exception to this single body rotation behavior occurred near the nozzle outlet where high tangential velocities persist. This region, however, exists near the outer radius of the separator, along the axial location of the nozzle outlet, and within azimuthal locations up to 90 degrees from the nozzle outlet. Overall, this region is relatively small in comparison with the separation volume. The assumption of rigid body rotation, then, is conservative as no account is made for this high velocity region and allows simplification of tangential velocity models developed for the MVS.

Examination of the tangential velocity results also indicated the importance of nozzle outlet area. A reduction of this area by 67.5% resulted in doubling the tangential velocities achieved by the separator models. Competing with this improvement is the pressure drop through the nozzle. As a result, achieving rotational speed gain by

reducing nozzle dimensions is limited by the pressure resources of the system. Furthermore, the largest model studied, a 14 cm diameter separator, showed a different tangential velocity profile for the narrow nozzle case. This profile change may indicate that nozzles of too narrow a dimension result in a change in momentum transfer behavior. In this case, the momentum spread more axially than radially, resulting in the same average rotational speed as the wider nozzle case but with lower tangential velocities in the region of the separation volume away from the wall. This effect is undesirable as lower tangential velocities reduce the magnitude of the centripetal acceleration field responsible for phase separation. For this study, the nozzles of each model were scaled according to separator radius. The results displayed by the narrow nozzle 14 cm diameter case indicate another scaling method should be investigated.

Dimensional analysis was conducted using the separator parameters of radius, inlet momentum rate, fluid properties, and rotational speed. Using the Buckingham Pi Theorem, a two group relationship between these parameters was found. Applying this relationship to the ground data and CFD results showed a strong correlation between the two Pi groups. Linear regression provided an equation linking rotational speed to the separator parameters. This equation was tested against the ground data and shown to predict average rotational speed well for all separator models used in the ground test.

The radial and axial transit times of gas bubbles within the separation volume were calculated using the method described in the theory section and the average rotational

speed prediction equation determined from the two Pi groups. Maximum radial transit time was found to occur when the separation volume is full of liquid. As the gas volume within the separation volume increases, both axial and radial transit times decrease. Radial transit time, however, decreases much more rapidly than axial transit time, indicating axial and radial transit times are closest in value for the all liquid case and increasing gas core diameter improves the operational characteristics of the separator. From a design standpoint, the all liquid case provides a conservative minimum flow rate for successful phase separation. Maximum flow rate depends on the pressure resources of the system.

The work presented here demonstrated that rigid body rotation is an acceptable assumption for the liquid within the separation volume, average rotational speed holds a linear relationship with inlet flow rate, nozzle outlet area directly affects tangential velocities within the rotating fluid, and average rotational speed can be predicted from known separator parameters. Together, these findings allow for a conservative prediction of separator performance. Further data collection, most importantly microgravity two-phase flow rotational speed data, will improve the accuracy of this model over the entire two-phase inventory range and allow for more aggressive separator designs. Notwithstanding the limitation to a conservative estimate, the model presented here provides a solid base for separator design and will aid in the optimization of future MVS applications.

To further develop the single phase model, continued ground testing should be pursued to provide more data to analyze the dimensionless relationship. Less intrusive rotational speed and more precise flow rate measurement methods will be necessary for the smaller separator sizes. Aside from flow rate, separator sizing, and nozzle geometry, the effects of varying fluid density and viscosity should also be examined to determine the ability of this model to predict MVS operation using a variety of fluids. Finally, microgravity testing of the rotational speed and flow rate relationship would be required to complete the single phase model.

Furthermore, extension of this model into a two-phase model should be attempted. Two-phase CFD will require more calculation time but would provide insight into the effect of the presence of a gas core on the tangential velocity profile. As the gas core is only produced during microgravity for the rotational speeds of interest, a non-intrusive rotational speed measurement technique would be required to validate the CFD results with data obtained during microgravity operation. Comparison of the two-phase model with the single phase model presented here would validate the use of this model as an initial design point for MVS systems.

REFERENCES

1) W. Dean, "Zero Gravity Phase Separation Technologies – Past, Present, and Future," *SAE Technical Paper Series*, **921160**, 1-7 (1992).

2) M. Izenson, "Water Balance in PEM Fuel Cells", *American Society of Mechanical Engineers, Advanced Energy Systems Division*, **42**, 147-154 (2002).

3) B. Ionnotta, "A Nuclear Jump-Start for Space Power", *Aerospace America*, **40**, 30-35, 39 (2002).

4) H. Ahn, K. Tanaka, H. Tsuge, K. Terasaka, K. Tsukada, "Centrifugal Gas-Liquid Separation under Low Gravity Conditions", *Separation Purification Technology*, **19**, 121-129 (2000).

5) D. Schrage, "Operational Characteristics of a Two-Phase Free-Vortex Separator for Micro-Gravity", *American Society of Mechanical Engineers, Heat Transfer Division*, **307**, 97-104 (1995).

6) F. Erdal, S. Shirazi, O. Shoham, G. Kouba, "CFD Simulation of Single-Phase and Two-Phase Flow in Gas-Liquid Cylindrical Cyclone Separators", *Society of Professional Engineers*, **2**, 436-446 (1997).

7) J. Tyack, R. Fenner, "Computational Fluid Dynamics Modelling of Velocity Profiles within a Hydrodynamic Separator", *Water Science and Technology*, **39**, 169-176 (1999).

8) W. Peng, A. Hoffmann, P. Boot, A. Udding, H. Dries, A. Ekker, J. Kater, "Flow Pattern in Reverse-Flow Centrifugal Separators", *Powder Technology* **127**, 212-222 (2002).

9) A. De Vries, *Path and Wake of a Rising Bubble*, Twente University Press, Enschede, Netherlands, (2001).

10) R. Fox, A. McDonald, *Introduction to Fluid Mechanics, Fifth Edition*, John Wiley & Sons, New York, (1998).

11) R. Clift, J. Grace, M. Weber. *Bubbles, Drops, and Particles,* Academic Press, New York, (1978).

12) *Star-CD Version 3.15 Methodology,* CD-Adapco, London, England (2004).

13) D. Mavriplis, "Mesh Generation and Adaptivity for Complex Geometries and Flows", *Handbook of Computational Fluid* Mechanics, 417-459 (1996).

14) *Star-CD Version 3.15 User Guide*, CD-Adapco, London, England (2004).

15) Z. Warsi, "Conservation Form of the Navier-Stokes Equations in General Nonsteady Coordinates", *American Institute of Aeronautics and Astronautics*, **19**, 240-242 (1981).

16) F. White, *Viscous Fluid Flow*, McGraw-Hill, New York, (1991).

APPENDIX A

A.1. Tangential Velocity Averaging Code

```
#define PI 3.14159265358979323846264

#include <iostream.h>
#include <iomanip.h>
#include <fstream.h>
#include <math.h>
#include <conio.h>
#include <string.h>
#include <dirent.h>


void opening(void);
char* uinput(char*, char*);

int main(void)
{
    char filename[12];
    DIR *cdir;
    struct dirent *cent;
    char *cfile;
    ifstream tfp;            // Input file stream (THE file pointer)
    ofstream ofp;             // Output file stream
    double vt[4000];
    double r[4000];
    double radii[100];
    double vavg[100];
    double n, t, z, vr, vz, axial;
    int counter, i;
    int length;

    opening();

    cout << "Current .grf files in this directory: " << endl << endl;
    cdir=opendir("."); //"." refers to the current dir
    while ((cent=readdir(cdir))){
        cfile=cent->d_name;
        length=strlen(cfile);
        if(cfile[length-3]=='g'&&cfile[length-2]=='r'&&cfile[length-1]=='f')
            cout << cent->d_name << endl;
    }
    closedir(cdir);

    cout << endl << "Enter input file name: ";
```

```
    cin >> filename;
    tfp.open(filename, ios::in);
    if(!tfp.is_open())
    {
        cout << endl << "FILE NOT FOUND" << endl << endl;
        return 1;
    }
    tfp >> n;
    tfp >> r[0];
    tfp >> t;
    tfp >> z;
    tfp >> vr;
    tfp >> vt[0];
    tfp >> vz;
    counter=0;

    while(!tfp.eof())
    {
       axial=z;
       while(z==axial)
       {
           ++counter;
           tfp >> n;
           tfp >> r[0];
           tfp >> t;
           tfp >> vr;
           tfp >> vt[0];
           tfp >> vz;
       }
       i=0;
    }

    tfp.close();

    return 0; // Success.
}

void opening(void)
{
    char in;

    clrscr();
    cout << "This program averages .grf data exported from StarCD for the Phase Separator" <<
endl << " model.  The proper format is:" << endl << endl;
    cout << "[CELL ID] [r] [t] [z] [Radial Velocity] [Tangential Velocity] [Axial Velocity]" << endl <<
endl;
    cout << "Tangential velocity data is averaged for each axial plane and radial ring." << endl <<
endl;
    cout << "Press any key to access the program." << endl;
    getch();
    clrscr();
}
```

A.2. Bubble Transit Time Calculation Code

```
// BTTS.EXE (Bubble Transit Time Simulation)
//
// This program calculates the transit time of and route taken by a bubble traversing the
// phase separator operating volume (cylinder volume).  In the tangential direction, the bubbles
// are assumed to move at the same speed as the liquid flow.  In the radial direction, bubble
// acceleration is assumed to result from the balance between bouyancy force and drag force.
// It is important to note that since this is a microgravity separator, the bouyancy force
// results from the centripetal acceleration imparted to the fluid as it moves around the cylinder.
//
// Return values:
//
// 0 - Success
// 1 - File I/O Error
// 2 - Re[b], Vr Solver did not converge to specified tolerance after MAXIT iterations.
// 3 - Negative square root error in vterm (Terminal Velocity) calculation.
//
// Michael Ellis
//
// 4/27/04 Initial code
// 5/4/05 Added rotational speed interpolation from ground data
// 6/9/06 Added rotational speed prediction from thesis

#define VERSION "2.2"
#define COMPILED "6/9/06"
#define PI 3.14159265358979323846264 // Ratio of circumference to diameter
#define START 19              // starting line for calculation display
#define MAXIT 1E8              // Maximum iterations to perform in Re[b], Vr solver
#define SMALL 1E-12              // Initial iteration time step until bubble nears terminal velocity

#include <iostream.h>  // C++ standard IO header
#include <iomanip.h>   // C++ IO manipulation header
#include <fstream.h>   // C++ file IO header
#include <math.h>      // C math header for sqrt() and atof()
#include <conio.h>     // for clrscr() and getch()
#include <string.h>    // for strlen()

void opening(void);
/* Welcome screen */
double uinput(char *name, double suggest);
/* General user input function */

int main(void)
{
    double vt, vr;    // Tangential and radial velocity variables.
    double dt;          // Time step variable.
    double Crb, rb, minr, r, thet;   // Bubble radius, radial location, and angular location.
    double cd;          // drag coefficient variable.
    double pl,pg;       // liquid and gas density variables.
```

```cpp
        double dv;              // dynamic viscosity variable.
        double D;               // Separator diameter.
        double nozh, nozw, noza; // Nozzle height, width, and area variables.
        double nozl;             // Nozzle characteristic length.
        double nozv;              // Nozzle outlet velocity.
        double lh, lt, lax;     // liquid film height, thickness, axial, and tangential flow area
        double lr, vavg;        // liquid film median radial position, average velocity in liquid film
        double Dcore[2];        // Gas core diameter range.
        double dd;
        double Ccore;
        double w;               // rotational speed.
        double rev;             // revolutions.
        double flow[2];          // Flow rate range.
        double Cflow;
        double df;
        double dax;
        double vterm;            // terminal velocity.
        double time;            // overall transit time.
        double Re;              // Reynold's number for Cd calculation.
        double We;               // Weber number for bubble stability check.
        double Mo;              // Morton number for bubble shape check.
        double acc;             // Acceleration from force balance.
        double converge;        // Covergence criteria
        int writefreq;          // File write frequency
        int err;                // Error checker variable
        int i, j, m;            // Used for position display during calculation.
        double st;              // Surface tension
        double Dint;
        fstream mfp;            // I/O memory file for program
        ofstream tfp;           // general output file handle
        ofstream sfp;

// Read memory file for easier re-use of program.  Unless no file, then set initial variables.

        mfp.open("BTTS.MEM", ios::in);
        if(!mfp.is_open())
        {
                // First run or mem file deleted.  Set initial values.
                D=4.5;
                Dcore[0]=1.5;
                Dcore[1]=3.1;
                dd=0.1;
                flow[0]=2.0;
                flow[1]=4.0;
                df=0.5;
                pl=997.009;
                pg=1.1614;
                dv=855E-6;
                dt=0.0001;
                rb=100.0; // diameter in microns, converted to meters later
                st=71.7E-3;
        }else
        {
```

```cpp
    // Read from memory file to restore variables from last run.
    mfp >> D;
    mfp >> nozh;
    mfp >> nozw;
    mfp >> Dcore[0];
    mfp >> Dcore[1];
    mfp >> dd;
    mfp >> flow[0];
    mfp >> flow[1];
    mfp >> df;
    mfp >> pl;
    mfp >> pg;
    mfp >> dv;
    mfp >> st;
    mfp >> rb;
    mfp >> dt;
    mfp.close();
  }
// Display opening screen and give user option to change initial parameters.
  opening();
  cout << "To reset to initial program values, delete file BTTS.MEM and re-run program." <<
endl << endl;
  D=uinput("Separator diameter (in)", D);
  nozh=uinput("Nozzle outlet height (in)", nozh);
  nozw=uinput("Nozzle outlet width (in)", nozw);
  Dcore[0]=uinput("Minimum gas core diameter (in.)", Dcore[0]);
  Dcore[1]=uinput("Maximum gas core diameter (in.)", Dcore[1]);
  dd=uinput("Gas core diameter increment (in.)", dd);
  flow[0]=uinput("Minimum liquid volumetric flowrate (Lpm)", flow[0]);
  flow[1]=uinput("Maximum liquid volumetric flowrate (Lpm)", flow[1]);
  df=uinput("Liquid volumetric flowrate increment (Lpm)", df);
  pl=uinput("Liquid density (kg/m3)", pl);
  pg=uinput("Gas density (kg/m3)",pg);
  dv=uinput("Liquid dynamic viscosity (kg/ms)",dv);
  st=uinput("Liquid surface tension (N/m)",st);
  rb=uinput("Bubble diameter (microns): ",rb);
  dt=uinput("Time step (s)",dt);
  writefreq=uinput("File write frequency (Hz):",0.01/dt);
  converge=uinput("Convergence tolerance (m)",0.001);
  cout << endl << "Calculating:" << endl;
/*
  Problem here, goes away when text is written to the screen for some reason.  May be because
  of pause.  File is just read, closed, then rewritten.  Might need a pause.
*/
// Write parameters to file.
  mfp.open("BTTS.MEM", ios::trunc | ios::out);
  if(!mfp.is_open())
  {
      cout << endl << endl << "FATAL ERROR: Failed to open BTTS.MEM" << endl << endl;
    return 1;  // File I/O Failure.
  }
  err=mfp.rdstate();
  switch(err)
```

```
        {
            case ios::eofbit: cout << endl << "ERROR: BTTS.MEM is an empty file." << endl; break;
            case ios::badbit: cout << endl << "ERROR: BTTS.MEM is an invalid file." << endl; break;
            case ios::failbit: cout << endl << "ERROR: BTTS.MEM bit check failed." << endl; break;
            case ios::goodbit:
            mfp << D << endl;
            mfp << nozh << endl;
            mfp << nozw << endl;
            mfp << Dcore[0] << endl;
            mfp << Dcore[1] << endl;
            mfp << dd << endl;
            mfp << flow[0] << endl;
            mfp << flow[1] << endl;
            mfp << df << endl;
            mfp << pl << endl;
            mfp << pg << endl;
            mfp << dv << endl;
            mfp << st << endl;
            mfp << rb << endl;
            mfp << dt << endl;
        break;
        }
        mfp.close();
        tfp.open("SETUP.DAT",ios::out);
        if(!tfp.is_open())
        {
            cout << endl << endl << "FATAL ERROR: Failed to open SETUP.DAT" << endl << endl;
            return 1;  // File I/O Error
        }
        tfp << D << " cm separator diameter w/ " << Dcore[0] << " to " << Dcore[1] <<" cm gas core."
<< endl;
        tfp << flow[0] << " to " << flow[1] << " Lpm volumetric flowrate." << endl;
        tfp << "Liquid density: " << pl << " kg/m3" << endl;
        tfp << "Liquid dynamic viscosity: " << dv << "kg/m s" << endl;
        tfp << "Gas density: " << pg << " kg/m3" << endl;
        tfp << "Bubble diameter: " << rb << " microns" << endl;
        tfp << "Time step: " << dt << " s" << endl;
        tfp.close();
// Calculate remaining intitial parameters.
        tfp.open("PATH.DAT", ios::out);
        if(!tfp.is_open())
        {
            cout << endl << endl << "FATAL ERROR: Failed to open PATH.DAT" << endl << endl;
            return 1;  // File I/O Error
        }
        i=1000; // set display counter.
        j=i+1; // set display flag counter so the first value is displayed.
// Print header to file.
        tfp << setw(15) << "time (s)";
        tfp << setw(15) << "radial (cm)";
        tfp << setw(15) << "angular (deg)";
        tfp << setw(15) << "Re[b]";
        tfp << setw(15) << "We[b]";
```

```cpp
   tfp << endl;

   sfp.open("TIMES.DAT", ios::out);
   sfp << setw(20) << "Gas Core (in.)" << setw(20) << "Flowrate (Lpm)" << setw(20) << "rpm" <<
setw(20) << "tradial (s)" << setw(20) << "taxial (s)" << endl;

// Convert variables to SI
   Dint=D*10.0;
   D*=2.54/100.0;
   nozw*=2.54/100.0;
   nozh*=2.54/100.0;
   noza=nozw*nozh;
   nozl=pow(noza,0.5);
   Dcore[0]*=2.54/100.0;
   Dcore[1]*=2.54/100.0;
   dd*=2.54/100.0;
   rb/=1.0E6;
   flow[0]*=0.001/60.0;
   flow[1]*=0.001/60.0;
   df*=0.001/60.0;

// Begin calculation
   for(Ccore=Dcore[0]; Ccore<=Dcore[1]; Ccore+=dd)
   {
        for(Cflow=flow[0]; Cflow<=flow[1]; Cflow+=df)
        {
        time=0.0;   // Set initial time to zero
                 tfp << endl;
           m=writefreq;
        r=D/2.0; // separator radius in meters.
        minr=Ccore/2.0+converge; // same with gas core.  Add tolerance.
        Crb=rb/2.0; // same with bubble diameter.
        vr=0.0; // set initial radial velocity to zero.
        thet=0.0; // set initial angular position to zero.
                 lax=PI*(D*D/4.0-Ccore*Ccore/4.0);
                 lr=(D-lt)/2.0;
        vavg=Cflow/lax; // Average axial velocity
        nozv=Cflow/noza;
        w=(0.3975*nozl*nozv-2126.3*(dv/pl))/pow(r,2); // rotational speed prediction from
dimensional analysis

        while(r>minr)
        {
           time+=dt;
           ++j;
           ++m;
           vt=2.0*PI*r*w; // Calculate tangential velocity assuming rigid body rotation
           thet+=(vt*dt/r)/PI*180.0;
           while(thet>360.0)
           {
              thet-=360.0;
           }
           Re=pl*vr*Crb*2.0/dv;
```

```
        if(Re==0.0)
        {
            cd=1.0;    // Actually cd is "infinite", but vr is zero, so term in acceleration equation
goes to zero.
        }else if(Re<20.0)
        {
            cd=24.0/Re*(1.0+0.1315*pow(Re,(0.82-0.05*log10(Re))));
        }else
        {
            cd=24.0/Re*(1.0+0.1935*pow(Re,0.6305));
        }
        if(Re==0.0)    // low flow, calculate terminal velocity using Stoke's approximation
        {
            vterm=pow(Crb,2)/12.0/dv*(pl/pg-1.0)*pow(vt,2)/r;
        }else        // Calculate from force balance
        {
            vterm=8.0/3.0*pow(vt,2)/cd*Crb/r*(1-pg/pl);
            if(vterm<0.0)
            {
                cout << endl << endl << endl << "FATAL ERROR: Terminal Velocity calculation
attempted square root of negative." << endl << endl;
                return 3;
            }
            vterm=sqrt(vterm);
        }
        vr=vterm;
        We=pl*vr*vr*r*Crb/vt/vt/st;    // Weber number calculation for bubble stability
        Mo=pow(vt,2)/r*pow(dv,4)/pl/pow(st,3);
        r-=vr*dt;
        if(m>writefreq)
        {
            m=0;
            tfp << setw(15) << setprecision(8) << time;
            tfp << setw(15) << setprecision(8) << r*100.0;
            tfp << setw(15) << setprecision(8) << thet;
            tfp << setw(15) << setprecision(8) << Re;
            tfp << setw(15) << setprecision(8) << We;
            tfp << endl;
        }
        if(j>i)
        {
            j=0;
            gotoxy(1, START);
            cout << setw(21) << "Flow: " << setprecision(2) << Cflow*60.0/0.001 << " LPM     ";
            gotoxy(38, START);
            cout << setw(21) << "Core: " << setprecision(2) << Ccore/2.54*100.00 << " in    ";
            gotoxy(1, START+1);
            cout << setw(21) << "r: " << setprecision(6) << r << " m  ";
            gotoxy(38, START+1);
            cout << setw(21) << "theta: " << setprecision(2) << thet << " degrees       ";
            gotoxy(1, START+2);
            cout << setw(21) << "Radial velocity: " << setprecision(4) << vr << " m/s    ";
            gotoxy(38, START+2);
```

```
            cout << setw(21) << "Tangential velocity: " << setprecision(4) << vt << " m/s    ";
            gotoxy(1, START+3);
            cout << setw(21) << "Re[b]: " << setprecision(4) << Re << "     ";
            gotoxy(38, START+3);
            cout << setw(21) << "Drag coefficient: " << setprecision(4) << cd << "      ";
            gotoxy(1, START+4);
            cout << setw(21) << "We[b]: " << setprecision(4) << We << "     ";
            gotoxy(38, START+4);
            cout << setw(21) << "Mo[b]: " << setprecision(4) << Mo << "      ";
            gotoxy(1, START+5);
            cout << setw(21) << "rpm: " << setprecision(4) << w << "      ";
            gotoxy(38, START+5);
            cout << setw(21) << "v[axial]: " << setprecision(5) << vavg << "      ";
         }
      }
      sfp << setiosflags(ios::fixed) << setw(20) << setprecision(4) << Ccore*100.0/2.54;
      sfp << setw(20) << setprecision(4) << Cflow/0.001*60.0;
      sfp << setw(20) << setprecision(4) << w*60.0;
      sfp << setw(20) << setprecision(4) << time;
      sfp << setw(20) << setprecision(4) << D/vavg << endl;

      gotoxy(1, START+7);
      cout << "Time from radius " << D/2.54*100.0 << " in. to " << r/2.54*100.0 << " in.: " <<
time << " s      " << endl;
      if(df==0.0)Cflow=Cflow+10;
    }
    if(dd==0.0)Ccore=Ccore+10;
  }
  tfp.close();
  sfp.close();
  cout << endl << "Case information found in SETUP.DAT" << endl << "Position information
found in PATH.DAT" << endl;
  cout << "Transit Time information found in TIMES.DAT" << endl;

  cout << "Press any key to exit the program." << endl;
  getch();

  return 0; // Success.
}

void opening(void)
{
  clrscr();
  cout << "Bubble Transit Time Simulation." << endl;
  cout << "Version: " << VERSION << " compiled " << COMPILED << endl;
  cout << "Michael Ellis" << endl << endl;
  cout << "This program calculates the bubble transit time and path experienced by a bubble";
  cout << "traversing the phase separator volume during operation.  The following" << endl;
  cout << "assumptions are made:" << endl << endl;
  cout << "- Bubbles move in the tangential direction with the same velocity as the fluid." <<
endl;
  cout << "- The radial bubble velocity results from the balance between the bouyancy and" <<
endl;
```

```
    cout << "  drag forces." << endl;
    cout << "- Fluid is assumed to move as a single body with constant rotational speed." <<
endl;
    cout << "- Bubbles move in the axial direction with the same velocity as the fluid." << endl;
    cout << "- Reynold's number is low and bubble is small enough to be treated as spherical." <<
endl << endl;
    cout << "Press any key to access the program." << endl;
    getch();
    clrscr();
}

double uinput(char *name, double suggest)
{
    double input;
    char *together;

    cout << name << " " << "[" << suggest << "]: ";
    cin.getline(together, 20, '\n');
    if(strlen(together)==0)return suggest;  // Possible end to function.
    input=atof(together);
    return input;   // Inevitable end to function.
}
```

A.3. CFD Data Extraction Code

```cpp
#define TOP 420
#define BOTTOM 2020
#define PI 3.141592653589793

#include <iostream.h>
#include <iomanip.h>
#include <conio.h>
#include <fstream.h>
#include <dirent.h>
#include <math.h>

class cfddata
{
  private:

      struct node  // data structure
      {
        double r, t, z;
        double vr, vt, vz;
        node *prev;
        node *next;
      };

      node *cfdtop; // pointer to the top of the list
      node *cfdbottom; // pointer to the bottom of the list
      node *cfdnow; // pointer to the current node
      node *places[10000]; // place holders for list (every 100)
      char *workingfile;
      ifstream ifs; // input file stream
      int length;
      double axials[50];
      int axialtot;
      double ztol, rtol;
      double flowrate, diameter, nozzlew, nozzleh;

      void newdata(void);
// Default method to add a new entry to the list.  Adds to the bottom of the list.
      int up(void);
// Move up an entry
      int down(void);
// Move down an entry
      node* select(int);

  public:
   cfddata(void);
        node* operator[] (int);
   int assign(char*);
        int load(void);
```

```
            void save(void);
            void swap(int,int);
// Build linked list from file input
            void getposition(double*, double*, double*);
// Retrieve position data for current entry
            void getvelocity(double*, double*, double*);
// Retrieve velocity data for current entry
            void display(void);
            int getlength(void);
// Display Cell Data
    long int total(void);
// Returns total number of entries.
    ~cfddata(void);
};

void opening(void);                    // Opening screen
void dirlist(void);                    // List current directory

cfddata::cfddata()
{
        cfdtop=NULL;
        cfdbottom=NULL;
        cfdnow=NULL;
        length=0;
        axialtot=0;
}

cfddata::node* cfddata::operator[] (int where)
{
    int i, skip;

        skip=where/100;
    cfdnow=places[skip];
    for (i=skip*100; i<where; ++i)
    {
            if(cfdnow->next!=NULL)cfdnow=cfdnow->next;
    }

    return cfdnow;
}

int cfddata::assign(char* filename)
{
        workingfile=filename;
        ifs.open(filename, ios::in);
        if(!ifs.is_open())
        {
                return 0;          // File not found
        }
        cout << endl << "Please specifiy the separator parameters associated with this";
        cout << endl << "data set." << endl;
        cout << endl << "Separator diameter (inches): ";
        cin >> diameter;
```

```
        cout << "Inlet flow rate (LPM): ";
        cin >> flowrate;
        cout << "Nozzle Height (inches): ";
        cin >> nozzleh;
        cout << "Nozzle Width (inches): ";
        cin >> nozzlew;
        cout << endl << "You may select a tolerance for incoming data to reduce the";
        cout << endl << "resulting output size.  Actual resulting tolerance will depend";
        cout << endl << "mesh parameters.  A zero tolerance is acceptable." << endl;
        cout << endl << "Enter axial tolerance in inches: ";
        cin >> ztol;
        cout << "Enter radial tolerance in inches: ";
        cin >> rtol;
        return 1;  // success
}

void cfddata::newdata()
{
        if(cfdtop==NULL)
        {
        cfdnow=new node;
        cfdnow->prev=NULL;
        cfdnow->next=NULL;
        cfdtop=cfdnow;
        cfdbottom=cfdnow;
        places[0]=cfdnow;
        }else
        {
        cfdnow=new node;
        cfdnow->prev=cfdbottom;
        cfdnow->next=NULL;
        cfdbottom->next=cfdnow;
        cfdbottom=cfdnow;
        }
}

int cfddata::up()
{
        if(cfdnow->prev!=NULL)
        {
                cfdnow=cfdnow->prev;
        }else
                return 0;
        return 1;
}

int cfddata::down()
{
        if(cfdnow->next!=NULL)
        {
                cfdnow=cfdnow->next;
        }else
                return 0;
```

```
            return 1;
}

cfddata::node* cfddata::select(int where)
{
    node *movetemp;
    int k;
    int skip;

    skip=where/100;
            movetemp=places[skip];
    for(k=skip*100; k<where; ++k)
    {
            if(movetemp->next!=NULL)movetemp=movetemp->next;
    }
    return movetemp;
}


int cfddata::load()
{
            double n, rad, the, axi;   // n - Cell ID, rad - radius, the - theta, axi - axis
            double vrad, vthe, vaxi;  // vrad - radial vel, vthe - tangential vel, vaxi - axial vel
            double checkvthe;  // Check variable to make sure data is in cylindrical coords
            double convrad, convthe;          // conversion variables
            int there, i;
            char gathered = 0;

            cout << endl << "Reading data file";

            while(!ifs.eof())
            {
                    if(++length % 10000 == 0)cout << ".";
                    ifs >> n;
                    ifs >> rad;
                    ifs >> the;
                    ifs >> axi;
                    ifs >> vrad;
                    ifs >> vthe;
                    ifs >> vaxi;

        there=0;
        for(i=0; i<axialtot; ++i)
        {
            if(axials[axialtot]==axi)there=1;
        }
        if(!there)
        {
            axials[axialtot]=axi;
            ++axialtot;
        }
                    if(!gathered)
                    if(fabs(rad)<0.05&&the>2.1)
```

```
                    {
                              gathered=1;
                              checkvthe=vthe;
                    }

                    newdata();
                    cfdnow->r=fabs(rad);
                    cfdnow->t=the;
                    cfdnow->z=axi;
                    cfdnow->vr=fabs(vrad);
                    cfdnow->vt=fabs(vthe);
                    cfdnow->vz=fabs(vaxi);
                    if(length % 100 == 0)
                    {
                              places[length/100]=cfdnow;
                    }
          }
          cfdnow=cfdtop;
          if(cfdnow==NULL)
     {
        cout << "Error reading file!" << endl << endl;
          return 0;
     }else
     {
          cout << "Complete.  " << length << " data points read." << endl << endl;
     }

          if(checkvthe>0.25)
          {
                    cout << "WARNING: Data appears to be in cartesian coordinates." << endl <<
"Convert to cylindrical coordinates [y/N]? ";
                    cin >> gathered;
                    if(gathered=='y'||gathered=='Y')
                    {
                              cout << endl << "Converting...";
          while(cfdnow!=NULL)
                         {
                                   convrad=sqrt(cfdnow->r*cfdnow->r+cfdnow->t*cfdnow->t);
                                   convthe=atan(cfdnow->t/cfdnow->r);
                                   cfdnow->r=convrad;
                                   cfdnow->t-convthe;
                                   cfdnow=cfdnow->next;
                         }
                         cout << "Done" << endl << endl;
                    }

          }
          cfdnow=cfdtop;

          return 1;
}

void cfddata::save()
{
```

```
        ofstream sfs;
        int i;

        sfs.open(workingfile, ios::out);
        cfdnow=cfdtop;
        cout << "Saving processed .grf file." << endl << endl;
        for(i=1; cfdnow->next!=NULL; ++i)
        {
        sfs << setiosflags(ios::fixed) << setprecision(4) << setw(20) << i << setw(20) << cfdnow-
>r << setw(20) << cfdnow->t << setw(20) << cfdnow-> z << setw(20) << cfdnow->vr << setw(20)
<< cfdnow-> vt << setw(20) << cfdnow->vz << endl;
            cfdnow=cfdnow->next;
        }
        sfs.close();
}

void cfddata::swap(int one, int two)
{
   node *onetemp, *twotemp;
   double temp;

   onetemp=select(one);
        twotemp=select(two);
   temp=onetemp->r;
   onetemp->r=twotemp->r;
   twotemp->r=temp;
   temp=onetemp->t;
   onetemp->t=twotemp->t;
   twotemp->t=temp;
   temp=onetemp->z;
   onetemp->z=twotemp->z;
   twotemp->z=temp;
   temp=onetemp->vr;
   onetemp->vr=twotemp->vr;
   twotemp->vr=temp;
   temp=onetemp->vt;
   onetemp->vt=twotemp->vt;
   twotemp->vt=temp;
   temp=onetemp->vz;
   onetemp->vz=twotemp->vz;
   twotemp->vz=temp;
}

int cfddata::grabdata()
{
        ofstream ofs;      // output file stream
        char ofile[12];
        double selectedz;
        int i, num=0;

        cout << "Positive axial locations: "<< endl << endl;
        for(i=0; i<axialtot; ++i)
        {
```

```
                      cout << setiosflags(ios::fixed) << setw(10) << axials[i];
                      if(i%5==0)
                      {
                              cout << endl;
                      }
              }
      cout << "Cell-centered tangential velocity data will be extracted along the diameter running"
<< endl;
      cout << "from the nozzle outlet to the opposite side of the separator."<< endl << endl;
      cout << "Select axial location: ";
      cin >> selectedz;
      cout << "Enter filename for extracted data: ";
              cin >> ofile;
              ofs.open(ofile, ios::out);
              ofs << setiosflags(ios::fixed) << setprecision(4) << setw(20) << "Diameter: " << setw(20)
<< diameter << setw(20) << "inches" << endl;
              ofs << setw(20) << "Flow Rate: " << setw(20) << flowrate << setw(20) << "LPM" << endl;
              ofs << setw(20) << "Nozzle H: " << setw(20) << nozzleh << setw(20) << "inches" <<
endl;
              ofs << setw(20) << "Nozzle W: " << setw(20) << nozzlew << setw(20) << "inches" <<
endl << endl;
              ofs << setw(20) << "r" << setw(20) << "theta" << setw(20) << "vt" << endl;

              cfdnow=cfdtop;

              while(cfdnow!=NULL)
              {
                      if(cfdnow->z==selectedz)
                      {
                              cfdnow=cfdnow->next;
                              ofs << setiosflags(ios::fixed) << setprecision(4) << setw(20) << cfdnow-r
<< setw(20) <<  << setw(20) << zsum/(double)num << setw(20) << vravg << setw(20) << vtavg
<< setw(20) << vzavg << setw(20) << cavg << setw(20) << rpmavg << endl;
                      }
              }
              ofs.close();
}

void cfddata::display()
{
              cout << setiosflags(ios::fixed) << setprecision(4) << "Cell Position:  [" << cfdnow->r << "
in. , " << cfdnow->t << " deg. , " << cfdnow->z << " in.]" << endl;
              cout << setiosflags(ios::fixed) << setprecision(4) << "Velocity: [" << cfdnow->vr << " m/s ,
" << cfdnow->vt << " m/s , " << cfdnow->vz << " m/s]" << endl;
}

int cfddata::getlength()
{
      return length;
}

long int cfddata::total()
{
```

```
  node *cfdtemp;
  long int c=0;              // The definitive dummy counter

  cfdtemp=cfdtop;
  for(;cfdtemp!=NULL; cfdtemp=cfdtemp->next)
      c++;

  return c;
}

cfddata::~cfddata()
{
  node *cfdtemp;
  if( cfdtop == NULL )
      return;

  while( cfdtop != NULL )
  {
      cfdtemp = cfdtop->next;
    delete cfdtop;
    cfdtop = cfdtemp;
  }
}

char *uinput(char *lead)
{
        char* input;

        cout << lead;
        cin >> input;

        return input;
}

void opening()
{
        clrscr();
   cout << "This program accesses .grf data exported from StarCD for the Phase Separator" <<
endl << "model.  The proper format is:" << endl << endl;
   cout << "[CELL ID] [r] [t] [z] [Radial Velocity] [Tangential Velocity] [Axial Velocity]" << endl <<
endl;
   cout << "Cell-centered velocity data is extracted for specified positions." << endl << endl;
   cout << "Press any key to access the program." << endl;
   getch();
   clrscr();
}

void dirlist()
{
   DIR *cdir;
   int length;
   struct dirent *cent;
   char *cfile;
```

```cpp
        cout << "Current .grf files in this directory: " << endl << endl;
    cdir=opendir("."); //"." refers to the current dir
    while ((cent=readdir(cdir))){   // This will generate a warning because of the = in the qualifier
statement, it is ok.
        cfile=cent->d_name;
        length=strlen(cfile);
        if(cfile[length-4]=='.'&&cfile[length-3]=='g'&&cfile[length-2]=='r'&&cfile[length-1]=='f')
            cout << cent->d_name << endl;
    }
    cout << endl;
    closedir(cdir);
}

int main()
{
        cfddata store;    // Linked list variable
        char input[12];

        opening();
        dirlist();
        cout << "Enter data filename from choices listed above: ";
    cin >> input;
        if(!store.assign(input))
    {
        cout << endl << "FILE NOT FOUND.  Program terminated." << endl << endl;
                return 1;
    }
    if(!store.load())
    {
       cout << "FILE CONTAINS NO DATA.  Program terminated." << endl << endl;
        return 2;
    }
    cout << "Data sort beginning.  This process takes several minutes depending on processor"
<< endl << "speed and file size." << endl << endl;
    store.save();
    while(store.grabdata()){};

        return 0;
}
```

VITA

Michael Clay Ellis received his Bachelor of Science degree in nuclear engineering in May, 1999 from Texas A&M University. He entered the nuclear engineering graduate program at Texas A&M University in August, 2002. His research interests include space power, microgravity fluid dynamics, computational modeling, and astronomy.

Mr. Ellis may be reached through Dr. Frederick Best, Texas A&M University, Department of Nuclear Engineering, MS 3133, College Station, TX 77840. Dr. Best's email address is fbest@tamu.edu.